

University of Trento

Manuel Fassin (Ph.D. Student)

**BEHAVIOUR AND MODELLING OF THE  
INELASTIC RESPONSE OF CONCRETE  
AND STEEL-CONCRETE  
INFRASTRUCTURES SUBJECTED TO  
LOW-CYCLE FATIGUE**

Prof. Oreste S. Bursi (Tutor)

April, 2016

UNIVERSITY OF TRENTO

Doctorate in Engineering of Civil and Mechanical  
Structural Systems

Cycle: XXVIII

Head of the Doctoral School: Prof. Paolo Scardi

Final Examination: 21 / 04 / 2016

Board of examiners:

Prof. Bozidar Stojadinovic (ETH, Zürich)

Prof. Alexander B. Movchan (University of Liverpool)

Prof. Daniele Zonta (University of Trento)

## **ABSTRACT**

Nowadays, infrastructures are of strategical importance for allowing communication between countries. Owing to its usefulness, the design and the maintenance of bridges, streets and tunnels, which represent the network, become a fundamental issue.

In order to investigate the behaviour of infrastructures under different loads, such as gravity, seismic phenomena, thermal differences, and so on, appears essential a comprehensive experimental campaign on scaled and full-scale specimens. In particular, in order to guarantee the safety of citizens, the seismic response of infrastructures under an earthquake requires a careful evaluation of the level of damage of structural elements.

In this thesis, typical case studies are considered, such as a concrete tunnel lining and a composite steel-concrete bridge.

In the first part of the thesis, a typical concrete tunnel lining is analysed. In order to investigate the inelastic behaviour of a concrete circular tunnel, several tests were performed. In greater detail, the best Fiber Bragg Grating (FBG) package configuration was obtained by means of monotonic and cyclic tests on substructures. Based on these results, the resulting suitable configuration in a full-scale tunnel test was used to measure deformations with high accuracy. Cyclic test on the full-scale tunnel provided data on the damage of reinforcing concrete and the developing of plastic hinges. With the aim of providing information on the structural safety of a tunnel after an earthquake, a damage index was calculated. In this respect, a nonlinear fiber F.E. model in the OpenSEES environmental was developed. This model calculated the stress in terms of bending moment in concrete sections with the use of experimental curvatures measured by FBGs system. Finally, the damage evolution in the concrete tun-

nel was reported and commented.

In the second part of this thesis, a composite steel-concrete short-medium span bridge is treated. The innovation was the application of the PEER Performance-Based Earthquake Engineering (PBEE) to this type of bridge. Moreover, the use of the Hot-rolled (HRS) steel to manufacture I-girder beams has become an innovation in civil infrastructures in Europe, as much as the use of transversal concrete cross-beams (CCBs) to connect spans. With reference to the hazard selected, a suitable case study was chosen. With the aim of understanding the most critical and stressed parts of the case study, preliminary elastic shell and stick models were developed. After the identification of interesting parts, half-scale subassembly specimens were designed and built. Several quasi-static tests, both monotonic and cyclic, were carried out with the objective of exploring global and local mechanisms in the section owing to low-cycle fatigue phenomena. To detect damage in the connection detail, a refined F.E. model in ABAQUS was developed. Fragility curve parameters of the damage's interest quantities were obtained by fitting experimental and numerical data by means of the Maximum Likelihood Estimation method. The results and the numerical model could be ready for the application of the Performance-Based Earthquake Engineering tool, in which decision variables, such as repair costs, downtime, human life loss and lane closures, were taken into consideration in order to increase the confidence in the design for both engineer and owner's viewpoint.

## ACKNOWLEDGEMENTS

I would like to express my gratitude to my tutor Professor Oreste Salvatore Bursi for his availability, experience and technical competence which have driven me during the Ph.D. carrier. It has been as harsh as formative experience for my training.

I would like to express also my gratitude to Professor Fabrizio Paolacci and all partners of the SEQBRI project for the opportunity to work together in an European project of major importance.

I would like to express my appreciation to Dr. Gabriele Zanon, Dr. Alessio Bonelli, and Dr. Nicola Tondini. I learned something from each of you, I am very grateful for this. Moreover, special thanks go to the Technicians Ivan Brandolise and Tiziano Dalla Torre which have helped me during the experimental campaign, and to the Draft-man Enrico Ceolan, for his support with drawings.

I would like to thank Eng. Enrico Cazzador and Eng. Andrea Morbioli, which have shared the office and the work with me during these years.

I would like to thank all my friends known in Trento and beyond, with whom I have shared joys and sorrows. In particular, I want to remember the good time spent together with Aaron, Alessandro, Andrea, Beatrice, Chiara, Cristiano, Dario, Diego, Dominic, Eleonora, Elia, Enrico, Federico, Fernando, Giuseppe, Irena, Luca, Mattia, Nicola, Paolo, Paolo Alberto, Stefania, Steven, Veronica, Walter and many others.

I would like to express many thanks my mother Daniela, my father Claudio, and my sister Martina for all their generous love during these years. Without your patience and support this milestone would not be possible.

Finally, I would like to express my heartfelt thank to my girlfriend Costanza, which support me any time with patience and love.



## PUBLICATIONS

As a result of the work conducted in this thesis and during the Ph.D. career, the following publications have been produced:

### Journal publications

- Tondini, N., Bursi, O.S., Bonelli, A. and **FASSIN, M.**, 2015. "Capabilities of a FBG sensor system to monitor the inelastic response of concrete sections in new tunnel linings subjected to earthquake loading", *Computer-Aided Civil and Infrastructure Engineering*, Guest Editors: Bursi, O.S., Feng, M.Q. and Wu, Z. 2014, Vol. 30, No. 8.
- Bursi, O.S., Tondini, N., **FASSIN, M.** and Bonelli A., 2015. "Structural Monitoring for the Cyclic Behaviour of Concrete Tunnel Lining Sections Using FBG Sensors", *Structural Control and Health Monitoring*, DOI: 10.1002/stc.1807.
- Bursi, O.S., Cazzador, E., **FASSIN, M.**, Paolacci, F. and Silvia, A. 2016. "A novel component-based model of steel I-girder-to-concrete cross beam connections for the seismic response of composite short-medium span bridges", *Earthquake Engineering and Structural Dynamics*, (to be submitted).

### Conferences

- Tondini, N., Bursi, O.S., **FASSIN, M.** and Zanon, G., 2013. "Seismic behaviour of joints made of high strength steel tubular columns", in *HSS-SERF: High strength steel in seismic resistant structures*, Timisoara: Universitatea "Politehnica" din Timisoara, In corso di stampa. Atti di: HSS-SERF 2013, Napoli, Italia, 28-29 Giugno.

- Bursi, O.S., Zonta, D. and **FASSIN, M.**, 2015. "Towards Intelligent Civil Infrastructure", in *17th International Conference on Transparent Optical Networks (ICTON)*, pp. 1-4, Budapest, Hungary, July 5-9, DOI:10.1109 /ICTON.2015.7193408.
- Cazzador, E., **FASSIN, M.**, Bursi, O.S., Paolacci, F. and Hechler, O., 2015. "Performance Based Earthquake Engineering applied to Composite Bridges with short and medium spans and Concrete Cross Beams", in *Proceedings of the 8th International Symposium on Steel Bridges: Innovation & New Challenges 2015 (SBIC-2015)*, Istanbul, Turkey, September 16-17
- **FASSIN, M.**, Cazzador, E., Bursi, O.S. and Paolacci, F., 2015. "An innovative mechanical model for steel-concrete connections of bridges subjected to earthquake loadings", in *XXV CONGRESSO C.T.A.*, Salerno, Italia, 1-3 Ottobre.

## CONTENTS

<b>1</b>	<b>Introduction</b>	<b>2</b>
1.1	Objective of the thesis . . . . .	3
1.2	Organization of the work . . . . .	5
<b>2</b>	<b>The MONICO and the SEQBRI projects</b>	<b>8</b>
2.1	The MONICO project . . . . .	8
2.2	The SEQBRI project . . . . .	10
<b>3</b>	<b>Design and verification of the tunnel lining case study</b>	<b>12</b>
3.1	Seismic design of a metro tunnel lining . . . . .	12
3.1.1	Tunnel features and soil characteristics . . . . .	12
3.1.2	Determination of stresses . . . . .	14
3.2	Test specimens . . . . .	17
3.2.1	Substructure specimens . . . . .	18
3.2.2	Full-scale specimen . . . . .	19
3.3	Test programme and load protocols . . . . .	22
3.3.1	Test typology applied to substructures and the full-scale specimen . . . . .	23

<b>4</b>	<b>Optical fibers and their packaging</b>	<b>26</b>
4.1	Introduction . . . . .	26
4.1.1	Theory of the FBG . . . . .	27
4.1.2	Temperature compensation . . . . .	29
4.2	FBG packaging . . . . .	30
4.2.1	Fiber packages in substructure tests . . . . .	35
4.2.2	Fiber packages in the full-scale test . . . . .	39
<b>5</b>	<b>Experimental campaign test results and damage evaluation</b>	<b>42</b>
5.1	Test results on substructures . . . . .	42
5.2	Full-scale tunnel ring test results . . . . .	48
5.3	Damage index and damage evaluation . . . . .	51
<b>6</b>	<b>Design and verification of the Bridge Case Study</b>	<b>56</b>
6.1	Definition and description of the case study CS #2.1.1 . . . . .	56
6.2	3D FE model and preliminary analysis of the bridge . . . . .	57
6.3	Design and verification of the CCB detail to static and seismic loading . . . . .	62
6.3.1	Standards on the design of the CCB joint solution . . . . .	62
6.3.2	Description of innovative SCCS-CCB solutions . . . . .	63
6.3.2.1	Cross-beam configuration: DIN FB 104 Var. C . . . . .	65
6.3.2.2	Cross-beam configuration: DOMI1 . . . . .	65
6.3.2.3	Cross-beam configuration: DOMI2 . . . . .	67
6.3.3	Procedure to design and verify the CCB detail . . . . .	67
6.3.4	ULS static verification of the DIN FB 104 Var. C cross-beam configuration . . . . .	73

6.3.4.1	Check of the component stresses by $F_{C,Ed}$ and $F_{t,Ed}$ . . . . .	74
6.3.4.2	Stress design of the connector system . . . . .	81
6.3.4.3	Tension resistance of connectors . . . . .	83
6.3.4.4	Check of the connector system . . . . .	86
6.3.4.5	Longitudinal shear and transversal reinforcement	88
6.3.4.6	Check of stitching reinforcement . . . . .	88
6.3.5	ULS static verification of DOMI1 and DOMI2 cross-beam configurations . . . . .	90
6.3.5.1	Check of the component stresses by $F_{C,Ed}$ and $F_{t,Ed}$ . . . . .	90
6.3.5.2	Stress design of the connector system and bars	94
6.3.5.3	Design and verification of the shear resistance of bars . . . . .	96
6.3.5.4	Longitudinal shear and transversal reinforcement	98
6.3.6	ULS seismic verification of innovative cross-beam configurations . . . . .	99
6.3.6.1	Check of tensile strength of longitudinal reinforcement in the concrete slab . . . . .	99
6.3.6.2	Check of shear resistance of concrete slab . . .	100
6.4	Selection of the representative subassembly specimen based on preliminary numerical analysis . . . . .	100
<b>7</b>	<b>Experimental campaign of subassembly specimens</b>	<b>104</b>
7.1	The experimental setup, the testing programme and the testing protocol . . . . .	104

7.1.1	Scaling procedure . . . . .	104
7.1.2	Design of subassembly specimens . . . . .	105
7.1.3	The test setup . . . . .	109
7.1.4	The testing programme . . . . .	110
7.1.5	The testing protocol . . . . .	110
7.2	Monotonic tests and outcomes . . . . .	111
7.2.1	SQ1M test . . . . .	113
7.2.2	SQ2M test . . . . .	118
7.2.3	SQ3M test . . . . .	118
7.2.4	Outcomes of monotonic tests . . . . .	119
7.2.5	Evaluation of the yielding point for cyclic tests . . . . .	120
7.3	Cyclic tests and outcomes . . . . .	121
7.3.1	SQ1C test . . . . .	122
7.3.2	SQ2C test . . . . .	125
7.3.3	SQ3C test . . . . .	126
7.3.3.1	The damage index $D_i$ and the damage domain . . . . .	126
7.3.3.2	Damage limit states . . . . .	130
7.3.3.3	SQ3C test results . . . . .	131
7.3.4	Outcomes of cyclic tests . . . . .	134
7.4	Vertical test and outcomes . . . . .	136
<b>8</b>	<b>Numerical modelling and analysis of the subassembly specimen</b>	<b>138</b>
8.1	3D F.E. modelling of the I-girder-CCB subassembly specimen . . . . .	138
8.1.1	Material models . . . . .	139
8.1.1.1	Steel materials . . . . .	139
8.1.1.2	Concrete material . . . . .	141

8.1.2	Description of the model . . . . .	146
8.2	Validation and calibration of the numerical modelling . . . . .	152
8.3	Comments . . . . .	157
<b>9</b>	<b>Damage assessment evaluation with a Performance-Based framework</b>	<b>160</b>
9.1	The Performance-based Earthquake Engineering methodology . . . . .	160
9.2	Assessment of components for damage fragility functions . . . . .	162
9.2.1	Engineering Demand Parameters . . . . .	163
9.2.2	Damage Measures . . . . .	163
9.2.2.1	Definition of damage states . . . . .	164
9.3	Damage Estimation and Evaluation of Fragility Curves . . . . .	167
9.3.1	Damage estimation from experimental tests and numerical simulations . . . . .	170
9.3.2	Fragility functions . . . . .	170
<b>10</b>	<b>Summary, Conclusions and Future Perspectives</b>	<b>178</b>
10.1	Summary . . . . .	178
10.2	Conclusions . . . . .	180
10.3	Future perspectives . . . . .	183



## LIST OF FIGURES

3.1	(a) Thrust action, and (b) bending moment estimated by means of Penzien and Wu (1998) relationships . . . . .	17
3.2	Transversal section of the specimen: (a) M-N diagram relevant to static and seismic LSLS actions, and (b) moment-curvature diagram relevant to maximum and minimum thrust action estimated by Penzien and Wu (1998) relationships. . . . .	18
3.3	(a) Cross-section specimen and relevant experimental strain distribution owing to the design earthquake, (b) actual four-points loading setup, and (c) four-points loading scheme (dimensions are in mm) . . . . .	20
3.4	(a) Plan and lateral views (dimensions are in cm), and (b) actual full-scale specimen setup. . . . .	21
3.5	Load testing protocol according to ECCS (1986) . . . . .	24
4.1	Cross-section of a FBG optical sensor . . . . .	27
4.2	Mode of operation of a FBG optical sensor . . . . .	28
4.3	Spectral distribution of strain FBG sensors in the 75-nm wavelength window. The sensor wavelengths were $\lambda_1 = 1.529$ nm, $\lambda_2 = 1.553$ nm, and $\lambda_3 = 1.577$ nm . . . . .	31

4.4	Deformed configuration of a reinforced concrete element subjected to bending . . . . .	32
4.5	Inclinometers, horizontal displacement strain and vertical displacement transducers configuration for substructure tests (dimension are in mm) . . . . .	33
4.6	(a) Fiber optic sensor stirrup, and (b) position of the FBGs in the groove. . . . .	35
4.7	Plan view, section view and picture before casting of the SSC2 fiber configuration . . . . .	36
4.8	(a) Plan view, section view and picture after casting of the SSC3 fiber configuration, and (b) plan view, section view and picture before casting of the SSC4 fiber configuration . . . . .	38
4.9	TLC1 test: details of fiber sensors used at different sections of the tunnel lining (dimensions are in mm) . . . . .	40
4.10	Distribution of fiber sensors along the inner and outer tunnel lining	41
5.1	(a) Experimental moment-rotation curve, and (b) moment-curvature response of SSM1 specimen, piecewise approximation and seismic demand . . . . .	43
5.2	Strain gauges, inclinometers, and displacement transducers setup for substructures (dimensions are in mm) . . . . .	43
5.3	SSC2 test: (a) moment-rotation curve detected with inclinometers and (b) moment-curvature relationship obtained from strain gauge displacement transducers assuming plane sections . . . .	45

5.4	SSC2 test: (a) strain values provided by bonded and unbonded fiber optic sensors located on the bottom side of the beam section, and (b) strains at the longitudinal rebar level for the $2\delta_y$ cycle with bonded fibers (dimensions are in mm) . . . . .	46
5.5	Unbonded internal vs.unbonded external fiber data from the bottom side of the SSC4 test . . . . .	47
5.6	Test on tunnel lining (TLC1): (a) strains owing to the pre-stressing of the ring section, Sec. #2 in., and (b) comparison between internal bonded FBG fiber data and standard displacements sensors during the cyclic test, Sec. #2 out. . . . .	50
5.7	TLC1 test, during the ECCS phase: (a) external unbonded FBG fiber data in Sec. #1, and (b) internal unbonded FBG fiber data in Sec. #6 in. . . . .	50
5.8	Damage limit domain of concrete section with parameter $\beta^*$ estimation . . . . .	52
5.9	(a) <i>Concrete 01</i> - Kent-Scott-Park concrete model, and (b) <i>Steel 02</i> - Giuffre-Menegotto-Pinto steel model after McKenna et al. (2000) . . . . .	53
5.10	TLC1 test: section damage evolution, during the ECCS phase . . . . .	54
6.1	(a) Longitudinal and (b) transversal views of the case study CS #2.1.1 . . . . .	58
6.2	3D modelling of the bridge case study CS #2.1.1 . . . . .	59
6.3	Typical configurations of CCB based on DIN FB 104 (2009): (a) Variant A, (b) Variant B, and (c) Variant C . . . . .	64

6.4	Concrete cross-beam configurations: (a) lateral and (b) top views of DIN FB 104 Var. C solution, (c) lateral and (d) top views of the DOMI1 solution, (e) lateral and (f) top views of the DOMI2 solution	66
6.5	Flow chart for the SCCS-CCB interface verification . . . . .	68
6.6	Stress distribution on (a) a generic SCCS beam, and on (b) a SCCS-CCB interface . . . . .	71
6.7	Equivalent T-stub in compression . . . . .	74
6.8	Strut-and-tie mechanism in (a) xz plane, and (b) xy plane . . . . .	79
6.9	Distribution of forces on the connector system in DIN FB104 Var.C solution . . . . .	82
6.10	Failure mechanisms to pull-out of the concrete cone for (a) a single stud, and (b) a group of studs . . . . .	85
6.11	Failure surface for longitudinal shear and transversal reinforcements of the connector system in DIN FB104 Var.C . . . . .	87
6.12	Instantaneous centre for connector system of DOMI1 and DOMI2 solutions . . . . .	93
6.13	Submodel types: (a) submodel A, (b) submodel B, and (c) submodel C . . . . .	101
6.14	(a) Out-of-plane bending moment $M_3$ , and (b) shear force $F_2$ comparison between Submodel A and full bridge model . . . . .	102
6.15	(a) Out-of-plane bending moment $M_3$ , and (b) shear force $F_2$ comparison between Submodel B and full bridge model . . . . .	103
6.16	(a) Out-of-plane bending moment $M_3$ , and (b) shear force $F_2$ comparison between Submodel C and full bridge model . . . . .	103

7.1	Steel girder-CCB connection details for (a) DIN FB 104 Var.C type, (b) DOMI1 type, and (c) DOMI2 type . . . . .	106
7.2	Testing equipment, specimen and sensor layout for (a) monotonic and cyclic tests with lateral loads, and (b) monotonic test with vertical load . . . . .	107
7.3	Strain gauges configuration for (a) front, and (b) top views for SQ1M/SQ1C tests; (c) front, and (d) top views for SQ2M/SQ2C tests; (e) front, and (f) top views for SQ3M/SQ3C/SQ3V tests, respectively . . . . .	108
7.4	Force-displacement relationship of monotonic tests . . . . .	112
7.5	Deformation measured by Gefran 1, 3, 5, 7 on the top concrete slab for (a) and (b) SQ1M test, (c) and (d) for SQ2M test, and (e) and (f) for SQ3M test, respectively . . . . .	114
7.6	Deformation measured by strain gauges on top and bottom flanges of steel girders for (a) SQ1M test, (c) SQ2M test, and (e) SQ3M test, respectively; deformation measured by strain gauges on longitudinal reinforcements of the concrete slab for (b) SQ1M test, (d) SQ2M test, and (f) SQ3M test, respectively . . . . .	115
7.7	Deformation measured by strain gauges on: (a) top, and (b) bottom rows of studs for SQ1M test; (c) top, and (d) bottom rows of studs for SQ2M test; (e) top row of studs and (f) bottom prestresses bars for SQ3M test . . . . .	116
7.8	Deformation measured by strain gauges on stirrups for (a) SQ1M test, (b) SQ2M test, and (c) SQ3M test . . . . .	117
7.9	Bi- and trilinear fits of a force-displacement relationship envelope	121

7.10 Force-displacement relationship for (a) SQ1C, and (b) SQ2C cyclic tests . . . . .	123
7.11 Damaged specimen after (a) SQ1C, and (b) SQ2C cyclic tests .	123
7.12 Deformation measured by Gefran 1, 3, 5, 7 on the top concrete slab: (a) and (b) for SQ1C test; (c) and (d) for SQ2C test, respectively . . . . .	126
7.13 Deformation measured by strain gauges on top and bottom flanges of steel girders for (a) SQ1M test, and (c) SQ2M test, respectively; deformation measured by strain gauges on longitudinal reinforcements of the concrete slab for (b) SQ1M test, and (d) SQ2M test, respectively . . . . .	127
7.14 Deformation measured by strain gauges on: (a) top, and (b) bottom rows of studs for SQ1C test; (c) top, and (d) bottom rows of studs for SQ2C test . . . . .	128
7.15 Deformation measured by strain gauges on stirrups for (a) SQ1C, and (b) SQ2C tests . . . . .	129
7.16 (a) Damage domain and limit states for tested specimens, and (b) force-displacement relationship for the SQ3C test . . . . .	132
7.17 Damaged specimen for the SQ3C test: (a) concrete crushing at the top of the slab, (b) top view of the slab and the CCB, (c) concrete cracking read by Gefran 7, and (d) concrete cracking at the edge of the slab . . . . .	133

7.18	Deformation measured in the SQ3C test by (a) Gefran 1 and 3, (b) Gefran 5 and 7 on the top concrete slab; deformation measured by strain gauges on (c) top and bottom steel flanges, (d) longitudinal rebars in the concrete slab, (e) upper row of Nelson studs, and (f) prestressed bars . . . . .	135
7.19	Force-displacement relationship of vertical monotonic test . . . . .	137
8.1	Response of concrete to uniaxial loading in (a) tension, and (b) compression . . . . .	142
8.2	Yield surfaces in (a) deviatoric plane, and (b) in plane stress . . . . .	144
8.3	(a) Mesh characterisation of the specimen, and (b) reinforcing steel elements embedded to the concrete specimen . . . . .	148
8.4	(a) S . . . . .	149
8.5	Trilinear force-displacement relationships of test setup (from(a) to (d)), and (e) springs setup configuration . . . . .	150
8.6	Model assembly of the specimen with boundary conditions, applied loads and the imposed displacement . . . . .	151
8.7	(a) Force-displacement comparison for the SQ3M specimen, and (b) actual damaged condition after the monotonic test . . . . .	152
8.8	Comparison between experimental data read from strain gauges and numerical simulation for the (a) SG9, (b) SG10, (c) SG15, and (d) SG16, respectively . . . . .	153
8.9	Damage of the concrete specimen in (a) compression, and (b) tension configurations, respectively . . . . .	155
8.10	Maximum stresses on (a) steel web protrusion, and (b) on steel reinforcement cage . . . . .	156

8.11 Location of the submodel analysed in the experimental campaign and with the FE model, and the position of the most stressed subassembly . . . . .	157
9.1 PBEE framework (after Moehle and Deierlein (2004); Porter (2003))	161
9.2 Visual damage observations corresponding to (a) DS1, and (b) DS2, respectively . . . . .	165
9.3 Visual damage observations corresponding to (a) DS3, and (b) DS4, respectively . . . . .	167
9.4 Identification of damage states for (a) SQ1M, (b) SQ1C, (c) SQ2M, (d) SQ2C, (e) SQ1M, and (f) SQ1C experimental tests, respectively	171
9.5 Fragility functions and probability of being at each damage state for the SCCS-CCB connection detail for the $EDP1 = d$ . . . . .	173
9.6 Fragility functions and probability of being at each damage state for the SCCS-CCB connection detail for the $EDP2 = \phi$ . . . . .	174
9.7 Fragility functions and probability of being at each damage state for the SCCS-CCB connection detail for the $EDP3 = HE$ . . . . .	175

## LIST OF TABLES

3.1	Geometrical and mechanical characteristics for the benchmark tunnel . . . . .	13
3.2	Maximum and minimum characteristic value of internal actions based on Penzien and Wu's theory . . . . .	16
3.3	Test programme and fibre combinations adopted in different tests	23
4.1	Constants and reference values for the fiber optic sensor in the Stirrup 1 . . . . .	37
4.2	Constants and reference values for the fiber optic sensor in the Stirrup 2 . . . . .	37
4.3	TLC1 test: strain and temperature fiber sensors . . . . .	39
5.1	Average values of prestraining . . . . .	49
5.2	Maximum deformations at each instrumented section . . . . .	49
6.1	Mechanical properties for the bridge model . . . . .	60
6.2	ULS actions and stresses on the composite section at the intermediate support . . . . .	60
6.3	Participant masses and periods for 13th and 14 modes of the bridge . . . . .	61

6.4	ULS seismic actions and stresses on the composite section at the intermediate support . . . . .	61
6.5	Geometrical properties of the SCCS-CCB interface . . . . .	72
6.6	Stresses and forces from SCCS to CCB interface . . . . .	73
6.7	T-stub checks on the DIN FB 104 Var. C solution . . . . .	77
6.8	Diffusive reinforcement in z-direction for DIN FB104 Var. C solution	80
6.9	Diffusive reinforcement in y-direction for DIN FB104 Var. C solution	80
6.10	Neutral axis of head steel plate for DIN FB104 Var. C solution . .	83
6.11	Maximum tension forces on a single stud connector for DIN FB104 Var. C solution . . . . .	83
6.12	Maximum tension forces on a group of stud connectors for DIN FB104 Var. C solution . . . . .	84
6.13	Longitudinal shear in the connector system for DIN FB104 Var.C solution . . . . .	89
6.14	Check of longitudinal shear in the connector system for DIN FB104 Var.C solution . . . . .	89
6.15	Stitching reinforcement for DIN FB104 Var.C solution . . . . .	90
6.16	T-stub checks on DOMI1 and DOMI2 solutions . . . . .	91
6.17	Diffusive reinforcement in z- and y-direction for DOMI1 and DOMI2 solutions . . . . .	92
6.18	Shear forces on the connector system for DOMI1 and DOMI2 solutions . . . . .	95
6.19	Shear resistance of the transversal bar . . . . .	96
6.20	Check of the connector system and bars for DOMI1 and DOMI2 solutions . . . . .	97

6.21 Reinforcement $A_{sf}$ and shear stress $v_{Ed}$ calculation for DOMI1 and DOMI2 solutions . . . . .	98
6.22 Check of longitudinal shear $v_{Ed,z}$ and $v_{Ed,x}$ in the connector system for DOMI1 and DOMI2 solutions . . . . .	99
7.1 Scale factors (Kumar et al., 1997) . . . . .	105
7.2 Testing program . . . . .	111
7.3 Relevant displacement and force values for monotonic tests . . .	112
7.4 Monotonic tests results . . . . .	120
7.5 Yielding points coordinates calculated in accordance with Bursi et al. (2002) . . . . .	122
7.6 Relevant displacement and force values for cyclic tests . . . . .	123
7.7 Damage limit states in accordance with Mackie et al. (2008) <sup>1</sup> and CEN (2006) <sup>2</sup> . . . . .	131
7.8 Cyclic tests results . . . . .	136
7.9 Vertical test results . . . . .	137
8.1 Tensile test results of S460M I-girder . . . . .	140
8.2 Tensile test results of B450C reinforcements . . . . .	140
8.3 Tensile test results of S235J2G3+C450 Nelson stud and M10.9 prestressing bar . . . . .	141
9.1 Component repair methods and items . . . . .	168
9.2 Statistical parameters estimated for $EDP1$ for the damage states	172
9.3 Statistical parameters estimated for $EDP2$ for the damage states	172
9.4 Statistical parameters estimated for $EDP3$ for the damage states	176



## **CHAPTER 1**

### **INTRODUCTION**

The damage evolution in infrastructures subjected to low-cycle fatigue phenomena is a relevant issue that afflicts both new and existing infrastructures in seismic countries. The correct evaluation of this quantity assumes a large importance due to economic and social consequences that the closure or/and the reconstruction of damaged infrastructures implicate. Moreover, the lack of knowledges of the seismic behaviour of critical detail connections requests a particular attention in both design and realization of components. Hence, experimental tests and numerical simulations can bridge this gap. However, mechanical and geometrical characteristics, as well as the response behaviour of the infrastructure, should be considered as stochastic values and treated by means of probabilistic approaches. In this light, it appears clear that also the damage should be calculated as a random variable.

The aim of this work is to understand the non-linear behaviour of components and subsystems of infrastructures, and to quantify the damage and related costs.

In this respect, two case studies are proposed and analysed. In greater

detail, the damage evolution of a concrete tunnel was monitored with a Fiber Bragg Grating (FBG) system by means of a damage index. Instead, in the second case study the damage measure, part of Performance-Based Earthquake Engineering (PBEE) approach, was calculated for a steel-concrete short-medium span bridge by means of fragility functions for all damage states and for each relevant engineering demand parameter.

## **1.1 Objective of the thesis**

This thesis is divided in two parts:

1. in the first part, the seismic behaviour of a concrete tunnel is analysed. In particular, a benchmark tunnel was adopted as case study, and stresses imposed from the ground to the concrete tunnel lining were computed. In order to quantify deformations in critical concrete sections, an experimental campaign on substructures and on a full-scale specimen has been conceived. The aim of these tests was to investigate the capability of the Fiber Bragg Grating (FBG) system to capture the inelastic behaviour of concrete sections subjected to low-cycle fatigue. In this view, monotonic and cyclic tests on substructure specimens that reproduce the plastic hinge phenomenon were used to identify the most suitable FBG configuration, and to prove its feasibility to measure high deformation level. Moreover, a cyclic test on a full-scale tunnel lining specimen showed the actual capability of the FBG system to monitor section deformations with reliability. In addition, in order to quantify the damage assessment of tunnel sections, a FE model developed in OpenSEES allowed to calculate bending moments acting on each section by means of curvature values

provided by the FBG strain evolution measurement. Finally, a damage index that measures the health's condition of the tunnel was carried out.

2. in the second part, the study of a benchmark steel-concrete bridge subjected to seismic loading is reported. In particular, the attention was focused on the connection between steel-concrete composite sections (SCCSs) and the concrete cross-beam (CCB). Three typologies of this detail were designed in accordance with European Standards. The seismic out-of-plane behaviour of joints needed to be investigated. Thus, an experimental campaign on subassemblies was carried out. The scaling process, the effective dimensions of subassemblies and the test setup were obtained by means of a preliminary FE model. Monotonic and cyclic displacement histories were applied to specimens. In order to record deformations, specimens were equipped with several devices, such as linear displacement potentiometers and strain gauges. Moreover, the damage condition of the specimen was observed during the test. The information provided by tests allowed to quantify the damage state of connection details. A 3D FE model of the connection was validated and calibrated on experimental data. This model was adopted to measure local phenomena such as stresses and deformations on the concrete slab and on the CCB. Finally, the PBEE approach was introduced to treat the damage measures. In order to estimate the parameters of the supposed probability distribution function, the Method of the Maximum Likelihood Estimation (MLE) was used. A fragility curve represents the probability of exceedence a certain damage limit state given an engineering demand parameter (EDP). Hence, fragility curves of more significant EDPs were generated.

## 1.2 Organization of the work

This thesis is organised in chapters as reported hereinafter:

- **Chapter 1.** This chapter includes the introduction and the organization of the thesis.
- **Chapter 2.** This chapter introduces the two European Projects with their peculiarities and objectives.
- **Chapter 3.** This chapter reports the characteristics of the benchmark tunnel lining, the static and seismic design and the experimental test programme.
- **Chapter 4.** This chapter introduces the Fiber Bragg Grating (FBG) system as devices to measure seismic deformations and provides several installation configuration of the FBGs on subassembly specimens and on a full-scale tunnel.
- **Chapter 5.** This chapter presents the experimental campaign on sub-assemblies and on full scale specimen subjected to monotonic and cyclic imposed displacement history. A numerical model, calibrated against experimental deformation read by FBGs system, allows to estimate the damage of the tunnel by means of a damage index.
- **Chapter 6.** This chapter introduces the benchmark steel-concrete composite bridge. The design and the verification of three different joint details between the steel-concrete section and the concrete-cross beam are described in detail.

- **Chapter 7.** This chapter investigates the out-of-plane behaviour of designed connection details subjected to monotonic and cyclic displacement testing protocols. Moreover, the residual vertical capacity of the damaged specimen is carried out.
- **Chapter 8.** This chapter shows the capability of a FE model of specimens to capture global and local behaviour, such as damage and other relevant stress and deformation.
- **Chapter 9.** This chapter introduces the PBEE methodology to assess the damage. In particular, fragility curves parameters of the most representative EDP are estimated by means of the Maximum Likelihood Estimation method. The related repair actions and associated unit costs are provided.
- **Chapter 10.** This chapter presents the conclusions along with the future perspectives.



## **CHAPTER 2**

### **THE MONICO AND THE SEQBRI PROJECTS**

#### **2.1 The MONICO project**

MONICO is a project funded by the European Union within the 7th research programme framework. The main objective of MONICO project is to ensure the safety of seismic-vulnerable tunnel cross-sections or sections where very high standards of safety are required, by developing a decision support system (DSS) that relies on information provided by fiber optic sensors; the information then allowing real-time assessment of the structural reliability of the tunnel lining (Loupos et al., 2011). The DSS is developed by incorporating two structural modules: the Expert System (ES) and the Data Base (DB). The former acts as a controlling interface between the user and the system, and coordinates the other modules. The user can estimate the actual structural condition at the monitored parts of the tunnel cross-sections as well as the overall structural condition of the cross-section. Moreover, by means of the DS module, the user can examine the trends of strain and structural condition of the monitored sections and of the entire tunnel lining, under the effects of past earthquakes. The DSS provides real-time warning of abnormal situations and allows the end-user

to examine different scenarios for hypothetical situations. In detail, to ensure the safety of vulnerable tunnel cross-sections, fiber optic sensors providing a real-time remote deformation sensing capability are integrated with software that collects and processes data and assesses the structural reliability of the lining. The fiber optic sensors record deformations in 8 locations of the tunnel cross-section. These deformations are then converted to strains, curvatures, deflections, stresses, bending moments, and axial forces, which are monitored so that they do not exceed limit values. Thus, local ductility of the monitored sections under operating loads is assessed deterministically and stochastically by varying the material properties represented by mean and standard deviation. Based on local damage indices after a seismic event, the global structural condition of the tunnel is stochastically estimated through the Monte Carlo simulation (MCS) method (Hammersley and Handscomb, 1975), where the Latin hypercube sampling (LHS) method is selected in order to reduce the computing effort (Iman and Conover, 1980). In detail, a nonlinear FE model of the tunnel is developed a priori with material and geometrical properties, that is the stress-strain and moment-curvature relationships that represent the stochastic variables. Then, a spectrum-compatible reference seismic input representative of the site is applied to the tunnel FE model and a series of dynamic nonlinear analyses are performed by varying material and geometrical properties. In this way, the extrapolation of the damage indices to other critical cross-sections is possible as well as the estimate of the structural reliability of each section of the tunnel by means of a First-Order Reliability Method (FORM) (Ditlevsen and Madsen, 1996).

The monitoring of concrete structures by means of FBG fibers is widely employed (Rodrigues et al., 2010; Habel and Krebber, 2011; Wu and Adewuyi,

2011), measuring cracking, displacement, vibration control, and other parameters. A common range for such reinforced concrete structures found in literature is  $\pm 1000$  to  $\pm 5000 \mu\epsilon$  (Majumder et al., 2008; Kerrouche et al., 2009). The novelty hereinafter is the assessment of FBG sensor capabilities in monitoring the inelastic response of a tunnel lining, when subjected to seismic loads, in full-scale tests. Moderate to strong seismic events can entail high inelastic curvature demand on concrete members, the bending associated with yield of the reinforcement steel. In this study, the target strain range was set to  $\pm 10000 \mu\epsilon$  (1%), to be measured by FBG sensors for ductile concrete sections.

## **2.2 The SEQBRI project**

The main objective of the European SEQBRI project is to explore the applicability of the next generation (full-probabilistic) PBEE approach in order to design short-medium span SCC I-girder bridges (Cazzador et al., 2015). Owing to its improved mechanical characteristics, such as tensile resistance, toughness, ductility, weldability and wear resistance, the high performance fine grain steel for hot-rolled members was investigated. In particular, the attention is focussed on the use of HRSS beams in SSC bridges with transversal CCBs, through the investigation of the seismic response of different joint connections between CCB and HRSS beams both for longitudinal and transversal seismic loading. Several SCC bridges were conceived in the project with three different total lengths: 96.20 m, 40.00 m and 193.60 m. For all of them the connection between spans was assured by a transversal CCB. Both the conceptual design and response of each bridge was carried out within the PBEE framework, where four variables are involved. In particular, it is considered:

- *Intensity Measure (IM)*, which represents a measure of the ground motion intensity. Several IM variables are available, such as Peak Ground Acceleration (PGA), Spectral Acceleration at fundamental period (Sa(T)), etc.;
- *Engineering Demand Parameter (EDP)*, which describes the structural response in term of global and local parameters such as deformation, forces, etc.;
- *Damage Measure (DM)*, which identifies the most relevant structural damage conditions;
- *Decision Variable (DV)*, which transforms the damage conditions into useful quantities for the risk management process decision.

The application of the PBEE methodology entails, under the requirements expressed in Yang et al. (2009), the evaluation of the mean annual rate  $\lambda$  of  $DV$  exceeding the threshold of  $dv$  as follows:

$$\lambda(DV > dv) = \iiint G(DV|DM) dG(DM|EDP) dG(EDP|IM) d\lambda(IM) \quad (2.1)$$

where  $G(\bullet)$  represents the complimentary cumulative distribution function of the considered variables.

It is evident that Equation 2.1 encompasses four components of performance assessment and it requires a fully probabilistic approach. Specifically, the quantification of  $\lambda(IM)$  requires a site hazard analysis, usually performed by a Probabilistic Seismic Hazard Analysis (PSHA),  $G(EDP|IM)$  needs a response analysis, usually performed by using numerical techniques (e.g. IDA),  $G(DM|EDP)$  requires a damage analysis often based on experimentation, whilst  $G(DV|DM)$  requires loss analysis (Günay and Mosalam, 2013).

## **CHAPTER 3**

### **DESIGN AND VERIFICATION OF THE TUNNEL LINING CASE STUDY**

#### **3.1 Seismic design of a metro tunnel lining**

##### **3.1.1 Tunnel features and soil characteristics**

The first case study analysed is an actual tunnel lining located in Rome. The geometrical and mechanical characteristics of the tunnel, as well as the soil are summarised in Table 3.1. With reference to NTC2008 (Ministero delle Infrastrutture, 2008), seismic actions at the Life Safe Limit State (LSLS) and at the Collapse Prevention Limit State (CPLS) were considered. For LSLS, a design reference peak ground acceleration (PGA) of 0.16 g, i.e. that associated with the type A ground (rock), was adopted. Moreover, due to strategic relevance of the infrastructure, an importance factor IV entailing a reference life of 200 years and a return period of 1898 years was assumed. This induced a PGA in a type D ground (deposits of loose-to-medium cohesion-less soil,  $S = 1.752$ ) of 0.28 g; thus, the peak ground particle velocity  $V_S = 0.319$  m/s was obtained. After that, Equation 3.1 was used to calculate the effective shear wave propagation velocity, equal to 125.1 m/s; with  $G_S$  was indicated the shear

**Table 3.1:** Geometrical and mechanical characteristics for the benchmark tunnel

Description	Symbol	Value	Unit
Outside diameter	$D$	4.80	m
Lining thickness	$t$	0.20	m
Deep tunnel axis	$H_S$	20	m
Height of water	$H_W$	5	m
Elastic modulus of concrete tunnel lining	$E_l$	31.4	GPa
Poisson's modulus of concrete tunnel lining	$\nu_l$	0.20	-
Elastic modulus of soil	$E_s$	84	MPa
Poisson's modulus of soil	$\nu_s$	0.49	-
Density of soil	$\rho_s$	1800	kg/m <sup>3</sup>

modulus of the soil. Finally, the maximum soil shear strain, equal to 0.26%, was determined by means of Equation 3.2.

$$C_s = \sqrt{\frac{G_s}{\rho_s}} \quad (3.1)$$

$$\gamma_{max} = \frac{V_s}{C_s} \quad (3.2)$$

For CPLS, a reference period of 200 years was adopted. Hence, the return period and the PGA increased to 2475 years and 0.30 g, respectively. The PGA values corresponding to LSLS and CPLS are typical of moderate/high seismic areas in Europe (ESD, <http://www.isesd.hi.is/ESDLocal/frameset.htm>).

### 3.1.2 Determination of stresses

In accordance with Penzien and Wu (1998), the response of the unboth-ered ground subjected to an earthquake can be in the transversal direction of the tunnel. This involves an ovalization of the section of the circular tunnel. This phenomenon was estimated by means of Penzien and Wu (1998) theory. On the bases of both deep tunnel and homogeneous soil assumptions, this approach provides lining stresses owing to:

1. the self-weight of the soil;
2. the overload;
3. the seismic deformation.

The main hypotheses of this method are the following two. Firstly, the assumption that no soil deformation occurs as a consequence of the tunnel boring method, and secondly, the condition of full slip between soil and tunnel. Thus, the variation in the diameter  $D$  of the circular tunnel is proportional to the variation of the hole in *free-field* condition. Penzien and Wu (1998) theory allows to calculate the dilational- and shear-type variation of the diameter due to Equation 3.3, Equation 3.4, and Equation 3.5 for the self-weight of the soil, the overload and the seismic action, respectively.

$$\begin{aligned}\Delta_{dl,sw} &= \frac{\bar{\sigma}_1 R(1 + K_{0,sw})(1 + \nu_s)}{E_s(1 + \alpha_d)} + \frac{2uR^2(1 - \nu_l^2)\alpha_d}{E_l A_l(1 + \alpha_d)} \\ \Delta_{sl,sw} &= \frac{\bar{\sigma}_1 R(1 - K_{0,sw})(1 + \nu_s)(3 - 4\nu_s)}{E_s(1 + \alpha_s^{sn})} \cos 2\theta\end{aligned}\tag{3.3}$$

$$\Delta_{dl,ol} = \frac{2p_{ol}R(1 + K_{0,ol})(1 - \nu_s^2)}{E_s(1 + \alpha_d)} \quad (3.4)$$

$$\Delta_{sl,ol} = \frac{4p_{ol}R(1 - K_{0,ol})(1 - \nu_s^2)}{E_s(1 + \alpha_s^{sn})} \cos 2\theta$$

$$\Delta_{sl,sm} = \frac{4R\gamma_c(1 - \nu_s^2)}{(1 + \alpha_s^{sn})} \cos 2\left(\theta + \frac{\pi}{4}\right) \quad (3.5)$$

where  $R$  denotes the radius,  $\bar{\sigma}_1$  the effective stress;  $K_{0,sw}$  and  $K_{0,ol}$  the lateral earth pressure coefficient for the self-weight and for the overload; respectively;  $u$  the water pressure;  $\gamma_c$  the shear deformation;  $A_l$  the unit length cross-section; and  $p_{ol}$  the overload (in this case assumed to be equal to 2 kN/m<sup>2</sup>). Moreover, in order to take into account soil-lining interaction stiffness, two adimensional coefficients  $\alpha_d$  and  $\alpha_s^{sn}$  were defined as follows:

$$\alpha_d = \frac{E_l A_l (1 + \nu_s)}{R E_s (1 - \nu_f^2)} \quad (3.6)$$

$$\alpha_s^{sn} = \frac{3E_l I_l (1 + \nu_s)(5 - 6\nu_s)}{R^3 E_s (1 - \nu_f^2)}$$

The inward diameter change owing to radial ( $\Delta_{d1}$ ) and to shear-type stresses ( $\Delta_{s1}$ ) was evaluated as a function of the above reported coefficients and soil characteristic parameters for each loading condition. Once  $\Delta_{d1}$  and  $\Delta_{s1}$  were determined, thrust, bending moment, and shear effects were evaluated with Equation 3.7, Equation 3.8, and Equation 3.9, respectively.

$$P_l(\theta) = - \left[ \frac{E_l A_l \Delta_{d1}}{2R(1 - \nu_f^2)} + \frac{3E_l I_l \Delta_{s1}}{2R^3(1 - \nu_f^2)} \right] \cos(2\theta) \quad (3.7)$$

$$M_l(\theta) = - \frac{3E_l I_l \Delta_{s1}}{2R^2(1 - \nu_f^2)} \cos(2\theta) \quad (3.8)$$

**Table 3.2:** Maximum and minimum characteristic value of internal actions based on Penzien and Wu's theory

Action	Load Case	Unit	Soil weight	Overload	Seismic action	Overall
Maximum	Bending moment	kNm/m	35.08	0.03	49.28	84.38
	Thrust force	kN/m	-676.67	-4.65	41.07	-640.25
	Shear action	kN/m	28.79	0.02	40.44	69.25
Minimum	Bending moment	kNm/m	-35.08	-0.03	-49.28	-84.38
	Thrust force	kN/m	-735.13	-4.70	-41.07	-780.89
	Shear action	kN/m	-28.79	-0.02	-40.44	-69.25

$$V_I(\theta) = -\frac{3E_I I \Delta s_1}{R^3(1 - \nu_I^2)} \cos(2\theta) \quad (3.9)$$

Between the seismic propagation direction and the seismic action exists a phase angle of  $45^\circ$ . Due to the circular shape and to the fact of being under static loading conditions, overall stresses are equivalent to an almost uniform compression load with limited bending and shear stresses. The overall stress state derives from the combination of the aforementioned three basic loads. The contribution caused by tension and shear stresses is calculated, and as a consequence, internal forces are evaluated. In particular, the maximum and minimum force values are shown in Table 3.2. Moreover, in agreement with Szechy (1970), Figure 3.1 shows the typical configuration of distribution of internal forces.

Figure 3.1(b) shows the bending moment distribution obtained using the Penzien and Wu (1998) relationships. Its sinusoidal shape exhibits a low gradient around the maximum and minimum moment: in fact, the maximum moment amplitude ( $\Delta M/M_{max}$ ) varies less than 15% over 1 m along the circular tunnel

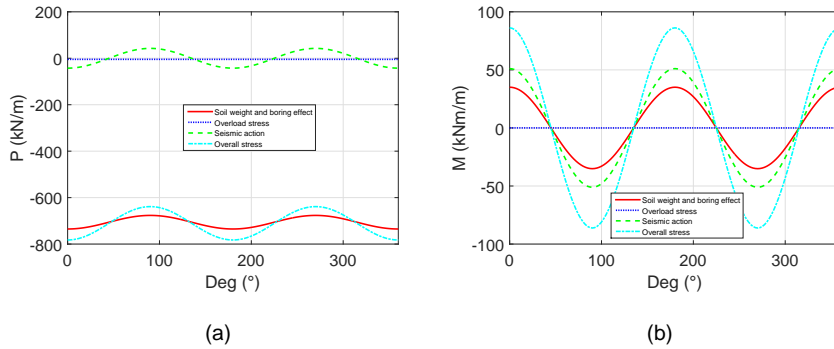


**Figure 3.1:** (a) Thrust action, and (b) bending moment estimated by means of Penzien and Wu (1998) relationships

lining. In order to reproduce this behaviour, a pure bending test on the appropriate substructure appeared to be the most suitable solution.

### 3.2 Test specimens

In order to investigate the behaviour of the concrete section under cyclic loads, an experimental campaign on relevant subassemblies and full-scale specimens became necessary. First of all, a design verification for both static and seismic LSLS combinations was provided by means of a M-N diagram, as shown in Figure 3.2(a). With reference to the benchmark tunnel, a 200 mm x 1000 mm concrete cross-section with (7+7)  $\Phi$  16 mm reinforcement bars was adopted. The concrete and the reinforcing steel were characterised by C25/30 and B450C material properties, respectively. Moreover, Figure 3.2(b) illustrates the moment-curvature diagram of the section associated with the maximum and minimum thrust. As expected, compression stresses increase

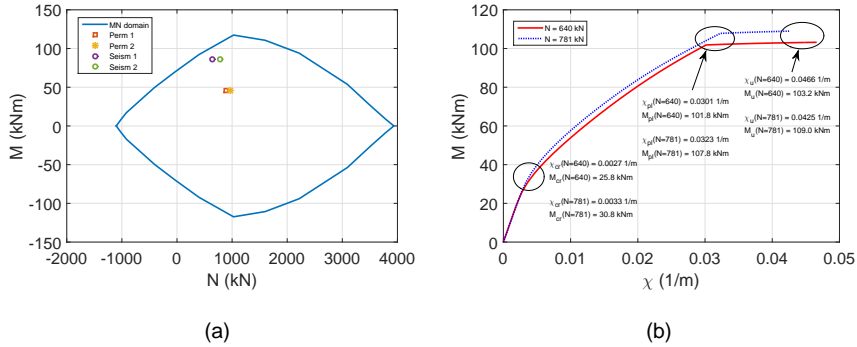


**Figure 3.2:** Transversal section of the specimen: (a) M-N diagram relevant to static and seismic LSLS actions, and (b) moment-curvature diagram relevant to maximum and minimum thrust action estimated by Penzien and Wu (1998) relationships.

section strength but decrease ductility.

### 3.2.1 Substructure specimens

The aim of substructure tests was twofold: i) to characterise the moment capacity and the plastic rotation of concrete sections, and ii) to select adequate packaging for FBG sensors for the full-scale test. Due to the fact that maximum bending moment remains constant over 1 m length on tunnel lining, a four-point bending test on subassemblies was planned. In fact, this configuration is able to provide a uniform bending moment on section. In order to understand the effective distance between the two points of the load's application, some considerations are carried out.

The favourable seismic behaviour of an infrastructure is characterised by the capacity of its section to dissipate inelastic energy. Locations where this dis-

sipation occurs are called plastic hinges. With reference to Williams and Sexsmith (1995) and Bursi and Ferrario (2003), the damage index  $D_i$  is strictly connected to the plastic hinge length  $l_{pl}$ . The length value can be calculated by means of the Nilson and Winter (1986) and OPCM 3274 (2003) relationships, i.e. Equation 3.10 and Equation 3.11, respectively.

$$l_{pl} = 0.5d + 0.05z = 165 \text{ mm} \quad (3.10)$$

where  $d$  is the effective depth of the cross-section and  $z$  is the distance from the critical section of the plastic hinge to the point of contraflexure.

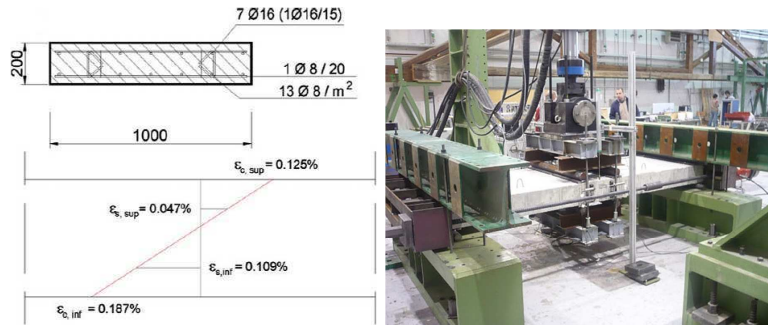
$$l_{pl} = 0.1L_v + 0.17h + 0.24 \frac{d_{bl}f_y}{\sqrt{f_c}} = 480 \text{ mm} \quad (3.11)$$

where  $L_v$  is the shear span,  $h$  defines the height of the section,  $d_{bl}$  is the average diameter of longitudinal rebars,  $f_y$  defines the yield strength of the reinforcement steel, and  $f_c$  is the concrete compression strength.

With reference to the above-mentioned considerations, the selected span for the uniform bending moment adopted was equal to 400 mm, namely a value between the limits calculated with Equation 3.10 and Equation 3.11. This type of test provided both flexural ductility and the strength characteristics without considering any shear effect. The cross-section specimen and the load scheme are shown in Figure 3.3. Each specimen had cross-section 1000 mm x 200 mm and length 3000 mm.

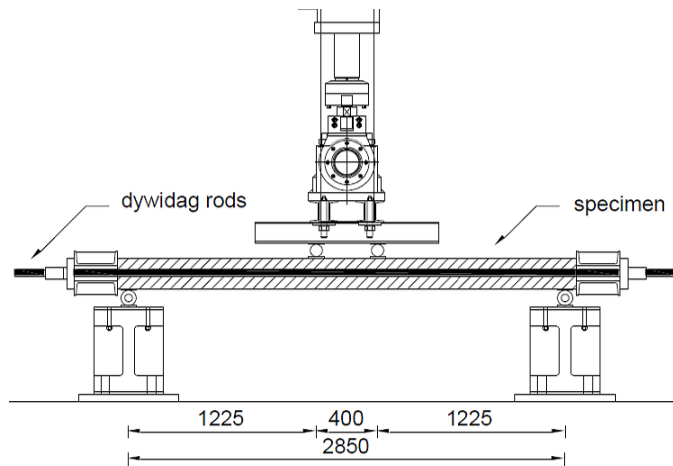
### 3.2.2 Full-scale specimen

With regard to the benchmark case study, a full-scale specimen of the tunnel lining was extracted. The geometry of the circular tunnel was characterised by the outside diameter of 4.8 m, thickness 0.2 m, and width 1.0 m.



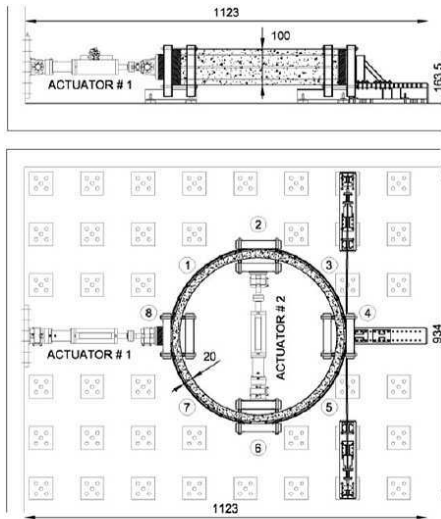
(a)

(b)

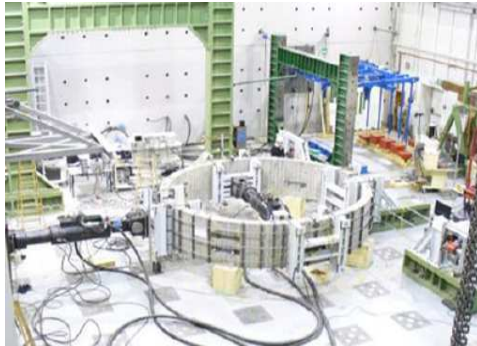


(c)

**Figure 3.3:** (a) Cross-section specimen and relevant experimental strain distribution owing to the design earthquake, (b) actual four-points loading setup, and (c) four-points loading scheme (dimensions are in mm)



(a)



(b)

**Figure 3.4:** (a) Plan and lateral views (dimensions are in cm), and (b) actual full-scale specimen setup.

In order to reproduce the stress configuration due to seismic actions, that were obtained from Penzien and Wu (1998); Hashash et al. (2001, 2005), and thus the ovalization of the tunnel section, two electro-hydraulic actuators were located orthogonally to one another. Figure 3.4 shows the configuration of the setup for the full-scale specimen. In fact, in this case, the worst case for the structural safety of a lining occurs when seismic waves propagate at an angle of  $45^\circ$ . This happens due to the fact that seismic action maxima, in this case, sum up with the static load maxima. Hence the maximum moment was reached at  $0^\circ$ ,  $90^\circ$ ,  $180^\circ$ , and  $270^\circ$ . The axial force was applied by steel ties carried by a system of cylindrical bearings. Detailed study on a F.E. model shows that this configuration is the most efficient solution as to friction losses.

In order to emulate loads derived from the ground and additional loads, three 24 mm high-tensile steel cables pre-stressed with two hollow jacks of capacity 1000 kN each, provided a force of 600 kN to the full-scale specimen. The same force was used for substructure tests. The cable tension was transferred to the ring by means of vertical steel rollers, as depicted in Figure 3.4.

### **3.3 Test programme and load protocols**

The experimental campaign was split into three parts:

1. tests on materials;
2. tests on substructures;
3. test on a full-scale specimen of a tunnel lining.

Tests on materials were carried out to characterize their mechanical properties. Table 3.3 reports the procedure used for each test of type (2) and (3).

**Table 3.3:** Test programme and fibre combinations adopted in different tests

Specimen	Test	Testing procedure	Test acronym	Note about fibres
Substructure	1	Monotonic	SSM1	No fibres
	2	Cyclic ECCS	SSC1	No fibres
	3	Cyclic ECCS	SSC2	Internal bonded and unbonded FBGs
	4	Cyclic ECCS	SSC3	External unbonded FBGs
	5	Cyclic ECCS	SSC4	Internal and external unbonded FBGs
	6	Cyclic ECCS	SSC5	External unbonded Brillouin fibres
Tunnel lining	7	Cyclic ECCS	TLC1	FBGs with various configurations

### 3.3.1 Test typology applied to substructures and the full-scale specimens

With reference to the test typologies applied to the substructures, both monotonic and cyclic tests were performed. In order to achieve force-displacement response and information concerning ductility, the monotonic test with imposed displacement control history was performed. Cyclic tests were imposed on the basis of the outcomes of this monotonic test. The load protocol for cyclic tests was created with reference to the procedure suggested by the European Convention of Constructional Steelwork (ECCS, 1986). Although this protocol was designed for steel structures, it was adopted in absence of a specific cyclic test procedure for concrete structures. The monotonic test provided the yielding parameter  $\delta y$ , i.e. the elastic-plastic transition of the cross-section behaviour. Hence, the cyclic loading history was defined as a series of cycles in displacement control, which were increased proportionally to the  $\delta y$  value, as shown in Figure 3.5.

In detail, the monotonic test on the substructure provided deflection by  $\delta y = 19$  mm. Moreover, the complete collapse of the beam was achieved at a displa-

cement of 60 mm, entailing significant loss in stiffness and strength. Hence, a maximum displacement of  $4\delta_y = 76$  mm was adopted for the cyclic tests. Finally, loads were applied in two phases in both monotonic and cyclic tests: i) initial axial specimen pre-stressed with Dywidag rods, and ii) vertical displacement by means of a hydraulic actuator.

With reference to the test typologies applied to the full-scale specimen, due to the fact that only one full-scale specimen was available, a cyclic test with ECCS (1986) loading history was performed. The yield displacement of the ring was  $\delta_{y_{ring}} = 60$  mm. This value was estimated from results provided by the monotonic test and numerical simulations of the entire ring.

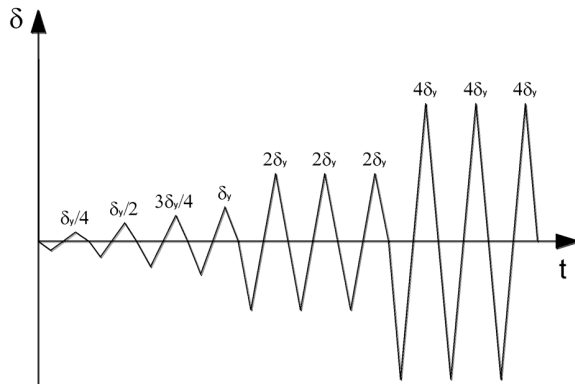


**Figure 3.5:** Load testing protocol according to ECCS (1986)



## CHAPTER 4

### OPTICAL FIBERS AND THEIR PACKAGING

#### 4.1 Introduction

Due to their relatively high strain resolution, multiplexing capability, low costs and virtually insensitivity to fluctuations in source power, narrowband fiber Bragg gratings (FBGs) have attracted considerable attention among optical fiber sensor technologies (Pozzi et al., 2008).

A FBG reflects a wavelength of light that shifts in response to variations in temperature and/or strain. Figure 4.1 shows several components that constituted the fiber section. FBGs are constructed by using holographic interference or a phase mask to expose a short length of photosensitive fiber to a periodic distribution of light intensity. The refractive index of the fiber is permanently altered according to the intensity of light it is exposed to. The resulting periodic variation in the refractive index is called a fiber Bragg grating, as shown in Figure 4.2.

The main advantages to use the FBG technologies are reported below:

- can measure very high strain levels ( $> 10000 \mu\text{m/m}$ ) and are therefore very well suited to high stressed composite constructions;

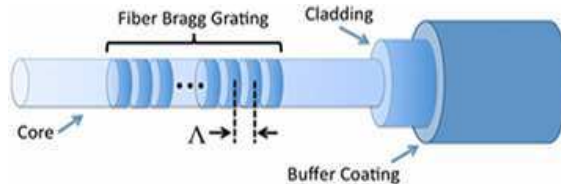


**Figure 4.1:** Cross-section of a FBG optical sensor

- show excellent long-term stability under mechanical fatigue conditions, making them perfectly suited for long-term conditions monitoring;
- are immune to electromagnetic interference (even lightning interference);
- are intrinsically passive (no electrical power required) and therefore can be positioned in high-voltage and potentially explosive atmosphere areas;
- can be read out over large distances, without the need of amplification means under way (> 20 km);
- due to the nature of the glass, FBGs show a good corrosion resistance.

An FBG-based system generally includes a broadband source (light emission device), a set of optical fibers with pre-written Bragg grating sensors and an Interrogation Unit with an optical spectrum analyser (Zonta et al., 2007).

#### **4.1.1 Theory of the FBG**

The FBG sensor is based on a periodic modulation of the index of refraction of the fiber core along the longitudinal direction (Werneck et al., 2013). The law that expresses the physical phenomenon inside the fiber is a simplification of

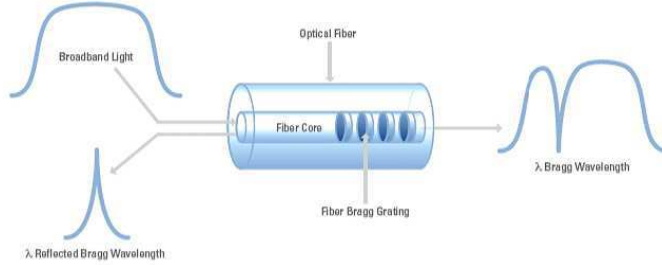


**Figure 4.2:** Mode of operation of a FBG optical sensor

the Bragg's law:

$$\lambda_B = 2n_{eff}\Lambda \quad (4.1)$$

where  $\lambda_B$  is the Bragg wavelength,  $n_{eff}$  is the effective refractive index of the fiber, and  $\Lambda$  is the periodicity of the grating. With reference to (4.1), it is possible to calculate the sensitivity of the Bragg wavelength with respect to strain and temperature. The sensitivity to strain is the partial derivative of Equation 4.1 with respect to displacement:

$$\frac{\Delta\lambda_B}{\Delta L} = 2n_{eff} \frac{\partial\Lambda}{\partial L} + 2\Lambda \frac{\partial n_{eff}}{\partial L} \quad (4.2)$$

Substituting twice Equation 4.1 in Equation 4.2 and rearranging:

$$\frac{\Delta\lambda_B}{\lambda_B} = \frac{1}{\Lambda} \frac{\partial\Lambda}{\partial L} \Delta L + \frac{1}{n_{eff}} \frac{\partial n_{eff}}{\partial L} \Delta L \quad (4.3)$$

The first term of Equation 4.3 is the strain of the grating period due to the expansion of the fiber and it is equal to 1. The second term of the Equation 4.3 is the photo-elastic coefficient  $\rho_e$ , i.e. the variation of the index of refraction with strain. The sensitivity of the Bragg wavelength displacement to strain is

the combination of both phenomena:

$$\frac{\Delta\lambda_B}{\lambda_B} = (1 - \rho_e) \varepsilon_z \quad (4.4)$$

where  $\varepsilon_z$  is the longitudinal strain of the grating. The sensitivity to temperature is the partial derivative of Equation 4.1 with respect of temperature:

$$\frac{\Delta\lambda_B}{\Delta T} = 2n_{eff} \frac{\partial\Lambda}{\partial T} + 2\Lambda \frac{\partial n_{eff}}{\partial T} \quad (4.5)$$

Substituting twice Equation 4.1 in Equation 4.5 and rearranging:

$$\frac{\Delta\lambda_B}{\lambda_B} = \frac{1}{\Lambda} \frac{\partial\Lambda}{\partial T} \Delta T + \frac{1}{n_{eff}} \frac{\partial n_{eff}}{\partial T} \Delta T \quad (4.6)$$

The first term of Equation 4.6 is the thermal expansion of the silica  $\alpha$ . The second term of the Equation 4.6 is the thermo-optic coefficient  $\eta$ , i.e. the temperature dependence of the refractive index. The sensitivity of the Bragg wavelength displacement with temperature is the combination of both phenomena:

$$\frac{\Delta\lambda_B}{\lambda_B} = (\alpha + \eta) \Delta T \quad (4.7)$$

The total sensitivity of the Bragg wavelength with strain and temperature is the sum of Equation 4.4 and Equation 4.7:

$$\frac{\Delta\lambda_B}{\lambda_B} = (1 - \rho_e) \varepsilon_z + (\alpha + \eta) \Delta T \quad (4.8)$$

#### 4.1.2 Temperature compensation

In order to measure only the strain with a FBG, a compensation of the variation of the local temperature is needed. A smart way to take into account this phenomenon is to put into the same fiber-optic device two FBGs: the first one

measuring strain and temperature, whilst the second one only the temperature, for compensation. From Equation 4.8 it could be obtain:

$$\begin{cases} \frac{\Delta\lambda_{B1}}{\lambda_{B1}} = (1 - \rho_e)\Delta\varepsilon + (\alpha + \eta)\Delta T \\ \frac{\Delta\lambda_{B2}}{\lambda_{B2}} = \phantom{(1 - \rho_e)\Delta\varepsilon} + (\alpha + \eta)\Delta T \end{cases} \quad (4.9)$$

After some algebraic manipulations, the resolution of the system provides the (4.10), i.e. the real strain of the FBG1 as measured by  $\Delta\lambda_{B1}$ , compensated against temperature variation measured by  $\Delta\lambda_{B2}$ . The temperature of the sensors is provided by Equation 4.11.

$$\Delta\varepsilon = \frac{1}{K_{\varepsilon 1} K_{T2}} (K_{T2} \Delta\lambda_{B1} - K_{T1} \Delta\lambda_{B2}) \quad (4.10)$$

$$\Delta T = \frac{\Delta\lambda_{B2}}{K_{T2}} \quad (4.11)$$

where GF and TK are parameters of the sensors:

$$K_{\varepsilon 1} = (1 - \rho_e)\lambda_{B1} = GF\lambda_{B1}$$

$$K_{T1} = (\alpha + \eta)\lambda_{B1} = TK\lambda_{B1}$$

$$K_{T2} = (\alpha + \eta)\lambda_{B2} = TK\lambda_{B2}$$

## 4.2 FBG packaging

In order to investigate the capability of the FBG to capture the inelastic behaviour of the tunnel lining subjected to moderate/high seismic loading, and to achieve the best FBG configuration, an experimental campaign on substructures and on a full-scale specimen was carried out. In particular, three types of configurations were explored:

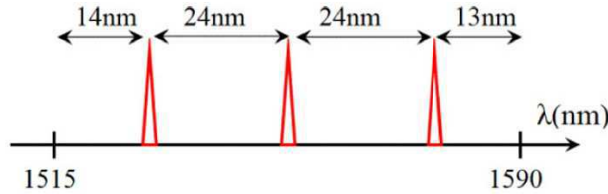


**Figure 4.3:** Spectral distribution of strain FBG sensors in the 75-nm wavelength window. The sensor wavelengths were  $\lambda_1 = 1529$  nm,  $\lambda_2 = 1553$  nm, and  $\lambda_3 = 1577$  nm

1. FBG sensors attached to reinforcement bars, bonded in concrete;
2. FBG sensors attached to reinforcement bars, unbonded in concrete;
3. FBG sensors externally mounted on metal holders welded to reinforcement bars through access holes left during casting.

The glue attached the sensors to the groove on rebar pieces, and contemporarily, protected them from the concrete. As demonstrated in Her and Huang (2011), at higher strain levels acrylate coating presented problems when embedded in or bonded to concrete material. In order to avoid this issue, acrylate coating and a 900  $\mu\text{m}$  tubing were used only for external fibers.

The seismic demand of the tunnel entailed a maximum rebar deformation of  $\varepsilon_{s,inf} = 0.109$ , as shown in Figure 3.3(a). That means, a value of at least  $\pm 1\%$  in terms of strain was adopted as target. In fact, this strain demand can be achieved with a FBG system that monitored the section damage evolution associated to the development of a plastic hinge and a minimum strain ductility of 10.

With reference to the system design, the following criteria had been pursued.

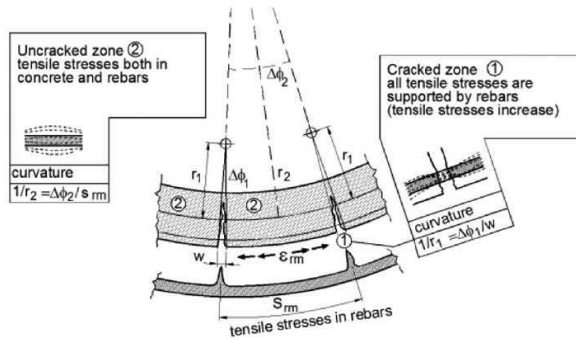


**Figure 4.4:** Deformed configuration of a reinforced concrete element subjected to bending

Since a maximum strain of  $10000 \mu\epsilon$  (1% deformation) was the target demand and that 3 nm of strain corresponded to a 0.25% deformation, a 12 nm of wavelength shift strain was adopted. Rao (1997) suggests to assume the typical FBG strain sensitivity equal to  $1.2 \text{ pm}/\mu\epsilon$ . Due to the fact that seismic loads could deform the fiber both in tension and in compression range, the space between the Bragg wavelengths was doubled. Thus, 24 nm of bandwidth per sensor was allocated. The number of sensors that can be applied on a FBG array depends on its wavelength shift. The interrogation unit had a nominal wave length range of 75 nm, i.e. its spectral limit was between 1515 and 1590 nm. Hence, only three sensors were applied on a single line, as depicted in Figure 4.3. Moreover, the wavelength spacing of the temperature sensors was between  $\pm 1$  and  $\pm 2$  nm, that allowed to measure temperature changes of over  $\pm 100^\circ\text{C}$ . Seismic excitations stresses the concrete section. When the corresponding deformation reached the tensile strain limit of the concrete, cracks developing with a certain spacing interval, typically several centimetres,

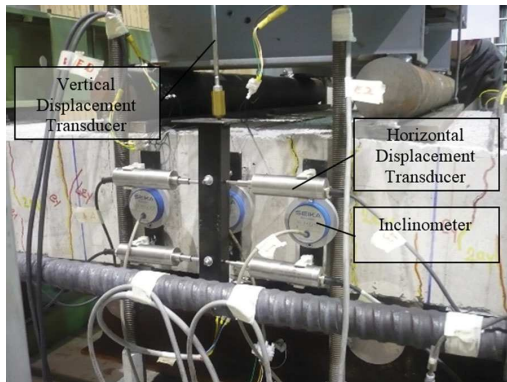
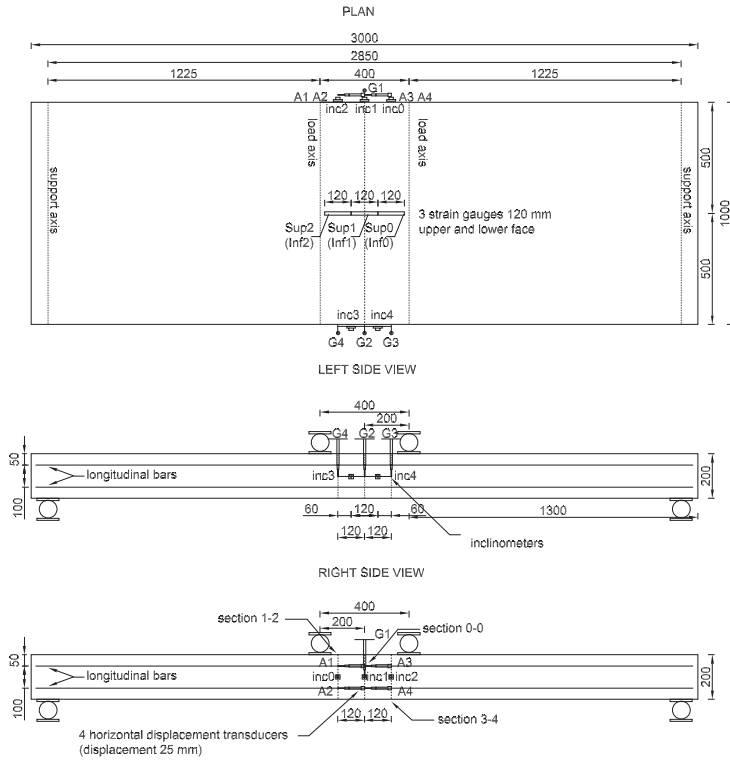


**Figure 4.5:** Inclinometers, horizontal displacement strain and vertical displacement transducers configuration for substructure tests (dimension are in mm)

as shown in Figure 4.4. In this configuration, the reinforcement bars undergo plastic deformation only in correspondence with cracked zones, whilst between two cracks the linear elastic regime can be observed. The base length of the FBG is very short and, consequently, the probability that a sensor spans a crack is very small. Thus, the possibility of measuring local phenomena instead of effective deformation of the section could jeopardize the measure reliability. In order to avoid that issue, the unbonded sensor solution was realised. In detail, the strain measurement was obtained as an average over a long measurement base. Moreover, the long-gauge sensor was not influenced by local material discontinuities and inclusions. For the unbonded sensor solution, fiber pre-strain was needed and the value ranged from 0.76% to 0.88%.

The expected average  $s_{r,avg}$  and maximum  $s_{r,max}$  spacing of cracks in the reinforcing concrete section were calculated in accordance with CEN (2005a), and were assumed to be equal to 110 mm and 180 mm, respectively. The external FBG sensors were mounted by welding two steel plates to the rebar cage at a distance larger than  $s_{r,max}$ . The installation of external FBG fibers was thought to be convenient when building the tunnel. The installation can be easily done after completion of the tunnel and replacement would be straightforward in the case of a fault.

In order to verify the reliability and accuracy of FBG sensors, several traditional devices such as potentiometers (Linear Variable Differential Transformers, LVDTs), strain gauge displacement transducers, inclinometers, and strain gauges were used to monitor the response of specimens during tests, as shown in Figure 4.5.

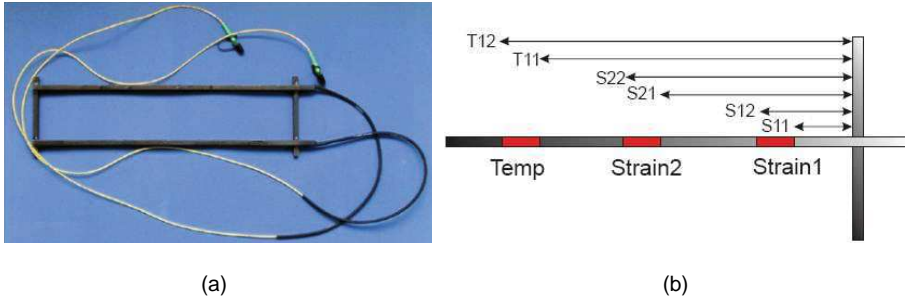


**Figure 4.6:** (a) Fiber optic sensor stirrup, and (b) position of the FBGs in the groove.

#### 4.2.1 Fiber packages in substructure tests

In order to understand the actual behaviour of FBG systems and, thus, to provide their the best configuration for the full-scale test, several FBG configurations on subassemblies specimens were investigated. Table 3.3 shows the test programme and the packaging configuration for each test. In particular, internal fibers were precast in the concrete.

Where the plastic hinge developed, the packaging of FBGs were glued to the longitudinal reinforcing steel. Two smart stirrups with sensors were adopted for the SSC2 test, as illustrated in Figure 4.6(a). In detail, this was an unbonded solution, where fibers were fixed in the 3-mm groove with a shore D 96 epoxy resin on two 10x10 mm steel bars. In order to protect the fibers, the groove was filled with silicone. Each bar contained two strain sensors and one temperature sensor, that allowed the correction of strain readings, as shown in Figure 4.6(b).

The fiber sensors were installed in two manners: i) sensors were completely fixed to the steel, strain values had been read on a short length (5 mm), this

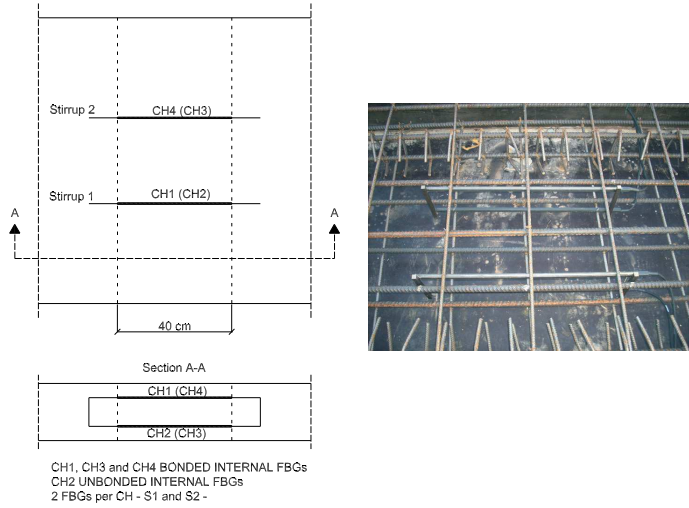


**Figure 4.7:** Plan view, section view and picture before casting of the SSC2 fiber configuration

configuration was assumed for three out of four bars; and ii) in order to provide an average value of strain on the whole bar length and to prevent the tension-stiffening effect, the bond between sensors and steel bars was impeded. Moreover, fibers were pre-stressed. The configuration of this solution is illustrated in Figure 4.7.

This system detected the variation of temperature and strain as follows:

$$T_t = T_0 + \frac{1000 \left( \lambda_{T,t}^{WL} - \lambda_{T_0}^{WL} \right)}{TK} \quad (^\circ\text{C}) \quad (4.12)$$

$$\varepsilon_t = \left[ \frac{\lambda_{\varepsilon,t}^{WL} - \left( \lambda_{T,t}^{WL} - \lambda_{T_0}^{WL} \right) - \lambda_{\varepsilon_0}^{WL}}{\lambda_{\varepsilon_0}^{WL} GF} \right] 10^6 \quad (\mu\varepsilon)$$

where  $TK$  and  $GF$  are characteristic sensor constants, as reported in Section 4.1.2;  $\lambda_{T_0}^{WL}$  and  $\lambda_{\varepsilon_0}^{WL}$  are the reference wavelength values of temperature

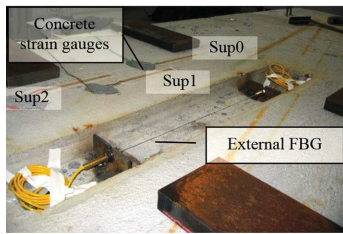
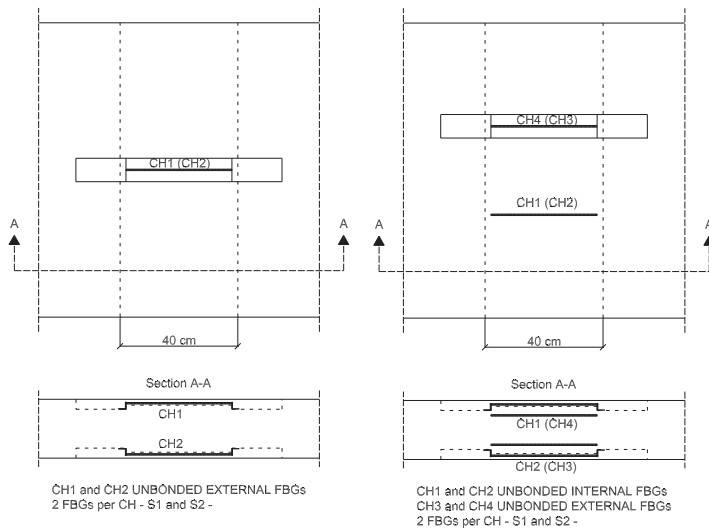
**Table 4.1:** Constants and reference values for the fiber optic sensor in the Stirrup 1

Stirrup 1	Constant	Sensor	Reference wavelength (nm)
	$GF = 0.78$	S1	1540.006
CH1	$TK = 9.8 \text{ pm/K}$	S2	1555.008
	$T_0 = 25.786 \text{ }^\circ\text{C}$	T	1565.034
	$GF = 0.78$	S1	1539.891
CH2	$TK = 9.8 \text{ pm/K}$	S2	1555.024
	$T_0 = 25.786 \text{ }^\circ\text{C}$	T	1565.034

(nm) and strain (nm), respectively;  $\lambda_{T,t}^{WL}$  and  $\lambda_{\varepsilon,t}^{WL}$  are the values at time  $t$  of temperature (nm) and strain (nm), respectively;  $T_0$  is the reference value of temperature ( $^\circ\text{C}$ ). Table 4.1 and Table 4.2 show values assumed for the Stirrup 1 and 2, respectively. In order to overcome issues highlighted in the SSC2 test configuration, a new FBG configuration was explored in the SSC3 speci-

**Table 4.2:** Constants and reference values for the fiber optic sensor in the Stirrup 2

Stirrup 2	Constant	Sensor	Reference wavelength (nm)
	$GF = 0.78$	S1	1565.197
CH1	$TK = 9.8 \text{ pm/K}$	S2	1555.330
	$T_0 = 27.724 \text{ }^\circ\text{C}$	T	1540.384
	$GF = 0.78$	S1	1539.842
CH2	$TK = 9.8 \text{ pm/K}$	S2	1554.950
	$T_0 = 28.845 \text{ }^\circ\text{C}$	T	1565.352



(a)



(b)

**Figure 4.8:** (a) Plan view, section view and picture after casting of the SSC3 fiber configuration, and (b) plan view, section view and picture before casting of the SSC4 fiber configuration

**Table 4.3:** TLC1 test: strain and temperature fiber sensors

N° sensor	Description
2 gauges	1 strain + 1 temp. sensor (inner and outer of Sections 1, 3, 4, 5, 7, and 8)
4 gauges	3 strain + 1 temp. sensor (inner and outer of Sections 2 and 6)
Total 40	24 strain sensors + 16 temp. sensors

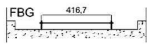
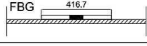
men, as depicted in Figure 4.8(a). In detail, the fiber was externally installed at the level of longitudinal rebars with a prestraining of 0.82 %.

Figure 4.8(b) shows the installed FBG system on the SSC4 test. In this case, the specimen was equipped with two types of FBG: i) external to the concrete, and ii) embedded in the concrete. The last configuration was achieved by protecting the unbonded length with flexible material-foam with water protection or silicone. The fiber prestraining was 0.84%.

#### **4.2.2 Fiber packages in the full-scale test**

The substructure tests provided the optimal fiber packaging, that was employed in the full-scale test. The best configuration was that with both internal and external unbonded FBG solution, and it will be discussed in Chapter 5. Nevertheless, in order to collect the potentiality of all FBG packages, the tunnel specimen was also equipped with bonded fibers. The comprehensive FBG installed in the full-scale specimen is presented in Figure 4.9. The sensors were positioned symmetrically at 8 points both of the inner (in) and of the outer (out) section of the tunnel lining, as shown in Figure 4.10. The total number of FBG sensors was based on the interrogation unit capabilities. In correspondence of the inner side of the tunnel and actuator load footprints, additional

	number of sensors
FBG	24

section	
1	
2	
3	
4	
5	
6	
7	
8	

**Figure 4.9:** TLC1 test: details of fiber sensors used at different sections of the tunnel lining (dimensions are in mm)

FBGs were inserted in two sections. In fact, plastic hinges developed in these areas. Finally, the complete FBG configuration consisted in 40 sensors, as summarised in Table 4.3. When acquiring data from fibers the target resolution was selected as high as  $1 \mu\epsilon$  and a maximum sampling rate of about 50 samples/sec was ideal for reproducing even the most rapid expected oscillations of a civil structure during an earthquake. The specimen was also instrumented with 16 + 4 standard displacement transducers and 6 load cells.

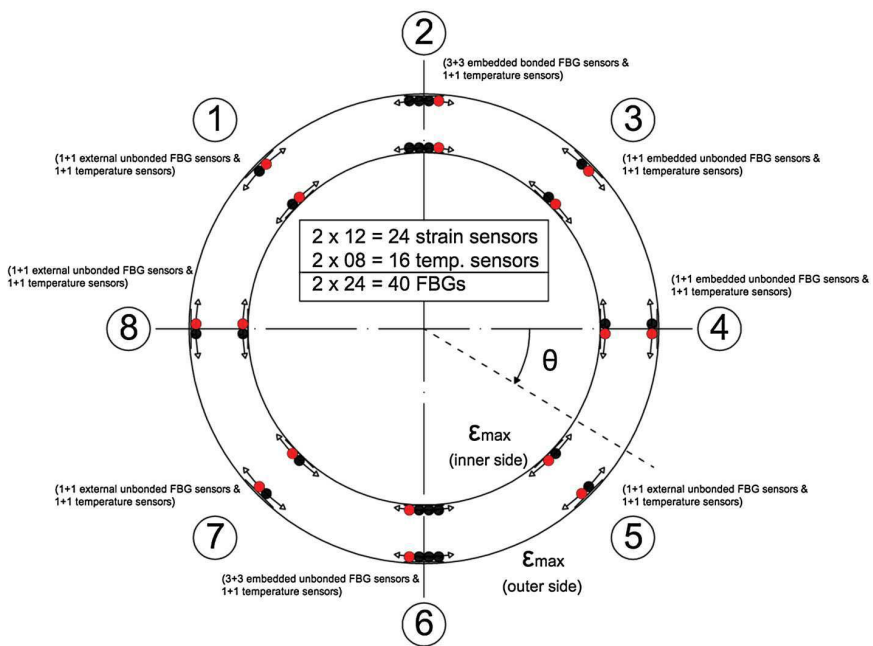


**Figure 4.10:** Distribution of fiber sensors along the inner and outer tunnel lining

## CHAPTER 5

### EXPERIMENTAL CAMPAIGN TEST RESULTS AND DAMAGE EVALUATION

#### 5.1 Test results on substructures

In order to experimentally evaluate the behaviour of the tested section, a monotonic test on the concrete section (namely *SSM1*) was carried out. The rotation at the elastic limit was approximately of 10 mrad, as shown in Figure 5.1(a). Thus, the yielding displacement was determined following the SAC (1997) protocol, and it was assumed to be equal to  $\delta_y = 19$  mm. This value was used as the reference parameter to calibrate the displacement history for cyclic tests in the ECCS (1986) procedure. The corresponding moment-curvature relationship, with a trilinear approximation of the section capacity and the relevant seismic demand were depicted in Figure 5.1(b).

With reference to cyclic tests, all substructure specimens were instrumented with standard sensors, as shown in Figure 5.2. This setup allowed to establish experimentally the plastic rotation and the curvature of the concrete section. In detail, under the assumption of the plane section, the plastic hinge rotation and the curvature can be calculated with Equation 5.1 and Equation 5.2, respec-

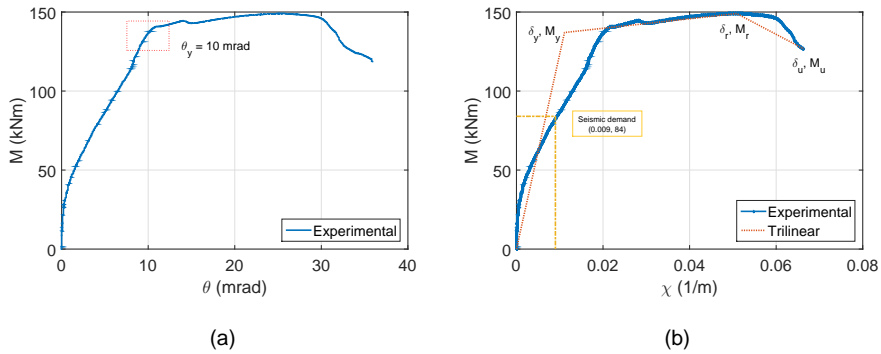


**Figure 5.1:** (a) Experimental moment-rotation curve, and (b) moment-curvature response of SSM1 specimen, piecewise approximation and seismic demand

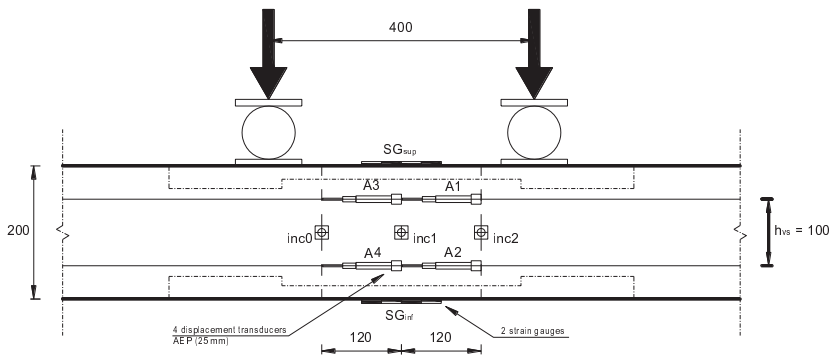


**Figure 5.2:** Strain gauges, inclinometers, and displacement transducers setup for substructures (dimensions are in mm)

tively.

$$\theta_{pl} = inc_2 - inc_0 \quad (5.1)$$

$$\frac{1}{r} = \frac{|\varepsilon_{sup}| + |\varepsilon_{inf}|}{h_{vs}} \quad (5.2)$$

where  $inc_0$  and  $inc_2$  are values provided by inclinometers;  $\varepsilon_{sup} = (A3 + A1)/l_{ref}$  and  $\varepsilon_{inf} = (A4 + A2)/l_{ref}$  are measured deformations over the estimated plastic hinge length at the superior and at the inferior longitudinal rebar level, respectively;  $A1$ ,  $A2$ ,  $A3$  and  $A4$  are displacements read by displacement transducers;  $l_{ref} = 240$  mm is the reference length;  $h_{vs} = 100$  mm is the distance between superior and inferior rebar level.

The first cyclic test, namely *SSC1*, was carried out with the aim to explore the actual ductility of the concrete section. Moreover, the specimen exhibited a plastic behaviour after that the yielding displacement was exceeded. Therefore, the choice in terms of  $\delta_y$  appeared correct.

The capability to detect inelastic deformations with internal bonded and unbonded fibers was explored in the *SSC2* cyclic test. Even though some asymmetric response of the section was observed during the test, the large dissipation of the plastic energy emphasised the positive hysteretic behaviour of the section. In order to highlighted this attitude, experimental moment-rotation and moment-curvature curves are reported in Figure 5.3. As a results, this cross-section was suitable for seismic applications. With reference to the data provided by the FBG system configuration, some consideration can be drawn from Figure 5.4(a). FBG sensors measured a reduction in terms of strain magnitude after the first cycle at  $2\delta_y$ . Both bonded and unbonded sensor solutions showed the same behaviour, probably due to the detachment of the stirrups from the

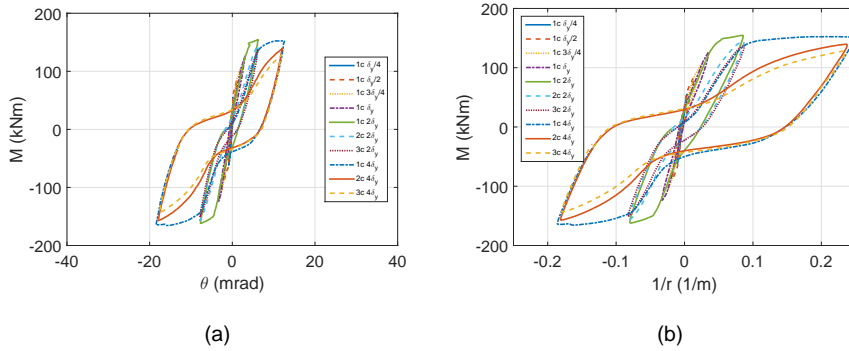
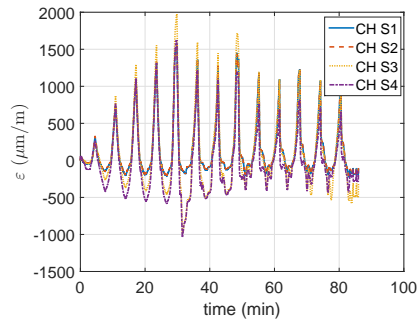
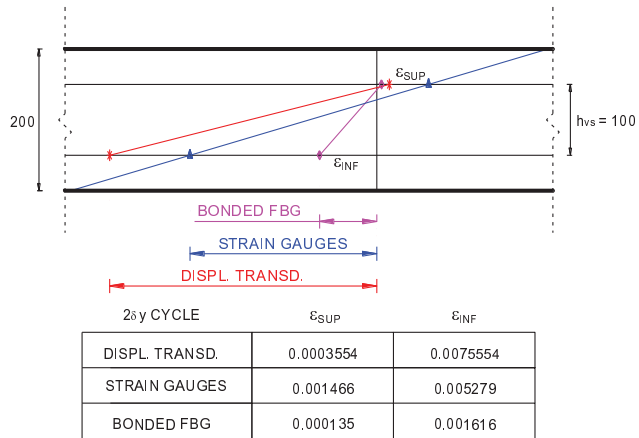


**Figure 5.3:** SSC2 test: (a) moment-rotation curve detected with inclinometers and (b) moment-curvature relationship obtained from strain gauge displacement transducers assuming plane sections

concrete at the moment of cracking. Furthermore, the deformation in compression (-) was always less than that in tension (+), as cracks opened under tension. Figure 5.4(b) shows the strain state of the cross-section provided by the strain gauge displacement transducers, strain gauges, and bonded FBGs, under assumptions of plane sections and perfect bond between concrete and reinforcing steel. Moreover, plastic behaviour read by these instruments are presented. As predicted by both displacement transducers and strain gauges, rebars had to be in the plastic range at an amplitude of  $2\delta_y$ . However, for FBG sensors the section seems to be in the elastic field given a discrepancy between the measurement base lengths. In fact, for displacement transducers and strain gauges an average base length of 120 mm was assumed, whilst only 5 mm base length was used for FBGs. As observed from the experimental tests, the cracking phenomenon more likely occurred over the length of 110 mm. Thus, in this configuration the FBG system detected small local deforma-



(a)



(b)

**Figure 5.4:** SSC2 test: (a) strain values provided by bonded and unbonded fiber optic sensors located on the bottom side of the beam section, and (b) strains at the longitudinal rebar level for the  $2\delta_y$  cycle with bonded fibers (dimensions are in mm)

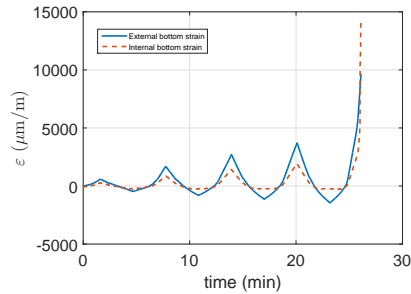


**Figure 5.5:** Unbonded internal vs.unbonded external fiber data from the bottom side of the SSC4 test

tions due to the fact that over the 5-mm-length concrete cracking was unlikely.

In the SSC3 cyclic test, the solution with FBGs externally installed was explored. Due to the fact that good results in terms of strains were reached, this FBG packaging was also adopted for the SSC4 specimen. More in detail, in the SSC4 test FBGs were installed embedded in the concrete and external to the concrete. The performance of the external fiber package compared to the internal one can be noted in Figure 5.5. Both solutions measured beyond 1% strain, thus they were suitable for the target strain.

The experimental campaign on substructures provided following outcomes:

1. the cross-solution used appears suitable for seismic load due to their ductile behaviour characterized by large deformations in the plastic range associated with high energy dissipation;
2. with reference to the SSC2 specimen, FBGs installed on a smart steel stirrup shows the capacity to measure strains beyond a  $2\delta_y$  displacement amplitude, that corresponded to only about 0.2% strain. In fact, the partial

detachment of the fibers from the steel stirrup or the detachment of the steel from concrete were the main causes;

3. this behaviour was avoided by means of a new package solution, that is the external installation of fibers on steel supports, and gluing fibers to ribbed bars of the same steel used to specimens. This solution was adopted for both remaining substructure tests and also for full-scale tunnel specimen;
4. the ability of both external and internal unbonded (with a portion of ribbed bar) package solutions to measure higher strains than the target value of 1% was achieved in the *SSC4* specimen;
5. short-length strain measurements prevented an effective measurement of mechanical cross-section behaviour. In fact, the strain field was underestimated owing to measurements carried out where cracks were not present. In this respect, external and unbonded fibers with 3 sensors in a row provided more accurate average values.

## **5.2 Full-scale tunnel ring test results**

Results obtained in the substructure specimens provided the most suitable FBG packaging for the full-scale test. Figure 4.9 and Figure 4.10 show fibers configuration. More specifically, external fibers were installed with the configuration used for substructure tests. In order not to modify the global behaviour of the reinforced concrete section, embedded fibers were installed on ribbed bars, with a small diameter of 8 mm made of the same steel B450C used in specimens. Moreover, in order to compare and monitoring the capability of FBGs

**Table 5.1:** Average values of prestraining

Section	#1	#2	#3	#4	#5	#6	#7	#8
Ave. out/in at the max. load ( $\mu\text{m}/\text{m}$ )	-122	-119	-96	-42	-139	-52	-120	-115

**Table 5.2:** Maximum deformations at each instrumented section

Section	#1	#2	#3	#4	#5	#6	#7	#8
Inner side of the ring $\varepsilon_{max}$ (%)	0.12	1.20	0.02	0.87	0.05	0.54	0.18	0.63
Outer side of the ring $\varepsilon_{max}$ (%)	0.05	0.46	0.01	0.59	0.02	0.21	0.03	0.50

and their measurement quality, conventional sensors were also used during the test.

In order to simulate the effect of confining soil, the full-scale tunnel specimen was pre-stressed by means of steel tendons. Strain results on the Section #2 were shown in Figure 5.6(a), whilst the average strain at each section can be read in Table 5.1.

The data acquired from the embedded FBG fibers were less disturbed than data read by external FBG fibers located in sections without plastic hinges, i.e. Sections #1, #3, #5, and #7, as observed in Figure 5.6(b) and Figure 5.7. The failure boundary in these figures represents the moment in time at which the first section of the tunnel failed, that is Section #8. Maximum deformation values for each instrumented section can be found in Table 5.2. As expected, fibers measured greater deformation in Sections #2, #4, #6, and #8, where plastic hinges formed. In detail, external FBG fibers approached a maximum value of about 0.6% in Section #8, whereas a maximum value of 1.2% was observed at Section #2. Temperature data, provided by the FBG fibers in the

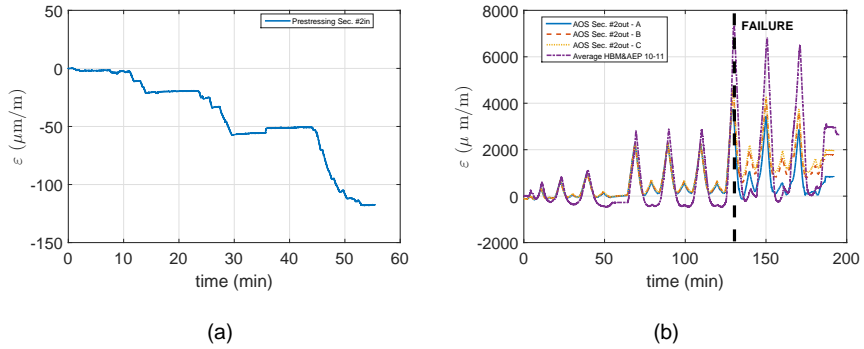


**Figure 5.6:** Test on tunnel lining (TLC1): (a) strains owing to the pre-stressing of the ring section, Sec. #2 in., and (b) comparison between internal bonded FBG fiber data and standard displacements sensors during the cyclic test, Sec. #2 out.

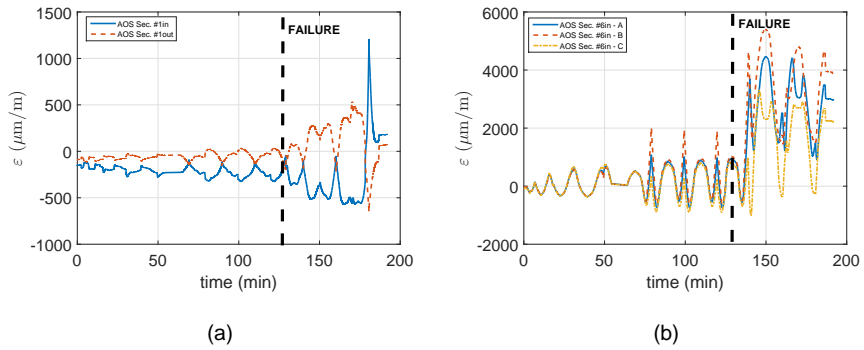


**Figure 5.7:** TLC1 test, during the ECCS phase: (a) external unbonded FBG fiber data in Sec. #1, and (b) internal unbonded FBG fiber data in Sec. #6 in.

Sections #2 in, #2 out, #3 in, #3 out, #4 in, #4 out, #6 in, and #6 out, indicated temperature variations between 19.05 and 21.51°C. The variation of about 2°C in a 4-hour test was consistent with conditions.

### 5.3 Damage index and damage evaluation

All the information in terms of deformation read by FBGs and traditional sensor devices are converted in strains, curvatures, stresses and then in bending moments and axial forces. The local ductility of monitored sections under operating loads can be assessed deterministically and stochastically by varying the material properties represented by the mean and standard deviation. Moreover, in order to detect the local damage at specific monitored locations, an energy-based damage index (Chai et al., 1995) based on the widely known damage model developed by Park and Ang (1985) was applied to the substructures and the full-scale tunnel specimen. In detail, it is expressed as follows:

$$D = \frac{\chi_m}{\chi_{um}} + \beta^* \frac{(E_h - E_{hm})}{M_y \chi_{um}} \quad (5.3)$$

where  $\chi_m$  is the maximum response curvature;  $\chi_{um}$  defines the maximum curvature under a monotonic loading;  $M_y$  is the yield moment of the section;  $\beta^*$  represents a strength deterioration parameter characterizing the damage contribution owing to cumulative plastic strain energy;  $E_h$  and  $E_{hm}$  are the plastic strain energy per unit length dissipated by the section, that is  $\int M d\chi$ , during the earthquake-cyclic loading and during a monotonic loading, respectively. Possibly,  $\chi_{um}$ ,  $E_{hm}$ , and  $M_y$  can be experimentally estimated. Three damage index limits were imposed, according to Bairaktaris et al. (1998):

1.  $D < D_1$ , where  $D_1 = E_{u1}/E_u$ , that corresponds to a condition where no

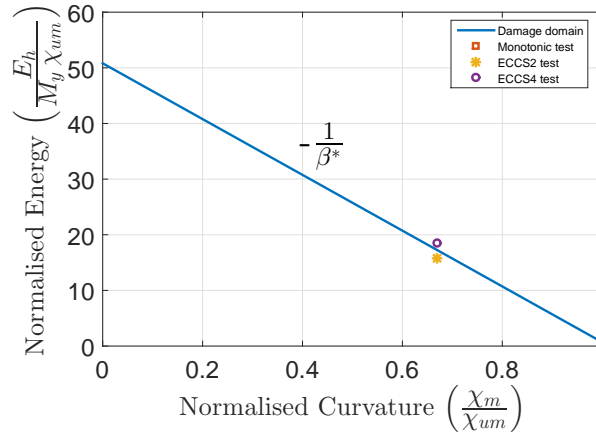


**Figure 5.8:** Damage limit domain of concrete section with parameter  $\beta^*$  estimation

plastic hinges form;

2.  $D_1 \leq D \leq D_2$ , where  $D_2 = E_{u2}/E_u$ , that sets the formation of the first plastic hinge in a concrete section;
3.  $D_2 \leq D \leq 1$  that corresponds to failure of a concrete cross-section.

In detail, energy terms can be calculated as follows:

$$E_{u1} = 0.75M_y\chi_y \tag{5.4}$$

$$E_{u2} = E_{u1} + 0.5(M_y + M_r)(\chi_r - \chi_y)$$

where  $M_y$  and  $\chi_y$  are the bending moment at yielding of rebars and the corresponding curvature, respectively;  $M_r$  and  $\chi_r$  are the maximum resisting bending moment and the corresponding curvature, respectively;  $E_u$  is the available internal energy, equal to the area of the hysteretic envelope. The evaluation of the degradation parameter  $\beta^*$  and the relevant damage index thresholds  $D_1$

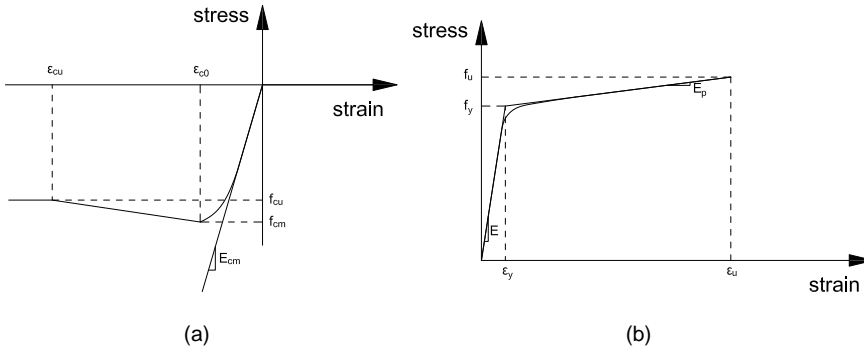


**Figure 5.9:** (a) *Concrete 01* - Kent-Scott-Park concrete model, and (b) *Steel 02* - Giuffre-Menegotto-Pinto steel model after McKenna et al. (2000)

and  $D_2$  were obtained by means of the experimental data resulting from both monotonic and cyclic tests. Specifically, the damage limit domain for the section of Figure 3.3(a) was determined through linear interpolation of experimental failure value, namely where  $D = 1$ , as shown in Figure 5.8. The value of  $\beta^* = 0.02$  was obtained. With reference to threshold values, Equation 5.4 allowed to calculate energy terms  $E_{u1} = 1.14$  kJ/m,  $E_{u2} = 6.83$  kJ/m, and  $E_u = 8.38$  kJ/m, and thus the damage index thresholds  $D_1 = 0.14$  and  $D_2 = 0.85$ . The results provided by FBGs and other devices installed on tunnel specimen allowed to quantify curvature values, under the assumption of plane sections. The bending moment for each section was calculated by means of the F.E. OpenSees software (McKenna et al., 2000). OpenSees, the Open System for Earthquake Engineering Simulation, is an object-oriented, software framework created at the NSF-sponsored Pacific Earthquake Engineering (PEER) Center. It allows users to create finite element applications for simulating the response of structural and geotechnical systems subjected to earthquakes.

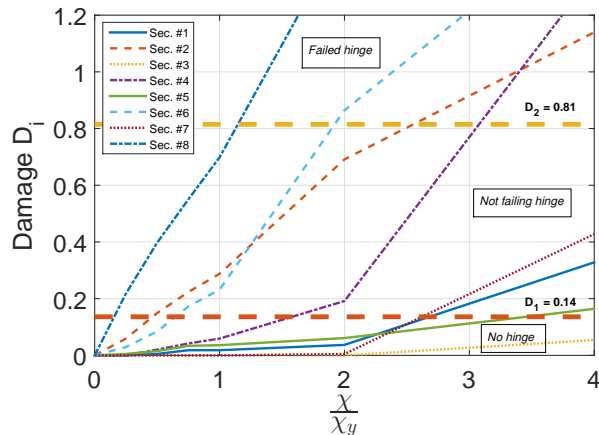


**Figure 5.10:** TLC1 test: section damage evolution, during the ECCS phase

More in detail, a *Zero-length* element with a fiber discretization of the cross-section was adopted in the model. Standard constitutive models for concrete and structural steel were provided by software. With reference to the concrete material, the *Concrete 01* model was adopted both for confined and unconfined concrete section, as depicted in Figure 5.9(a), but with different mechanical parameters. *Steel 02* model was instead used to characterise the mechanical behaviour of the reinforcing steel, as shown in Figure 5.9(b). The mechanical parameters, that obtained from a mechanical characterisation in the laboratory, were considered deterministic due to the fact that only one test was conducted on full-scale specimen. The experimental curvature measured was thus applied to the section. Hence, the model provided corresponding estimated bending moments acting on each section. The damage evolution can be evaluated by means of Equation 5.3. Finally, the damage evolution of each section and the two damage thresholds  $D_1$  and  $D_2$  are shown in Figure 5.10. As confirmed

from experimental results highlighted in both Figure 5.6 and Figure 5.7, the first section that reached the damage failure thresholds  $D_2$  was Section #8. The outcomes emphasise the capability and the reliability of the model to predict the failure of the tunnel lining.

## **CHAPTER 6**

### **DESIGN AND VERIFICATION OF THE BRIDGE CASE STUDY**

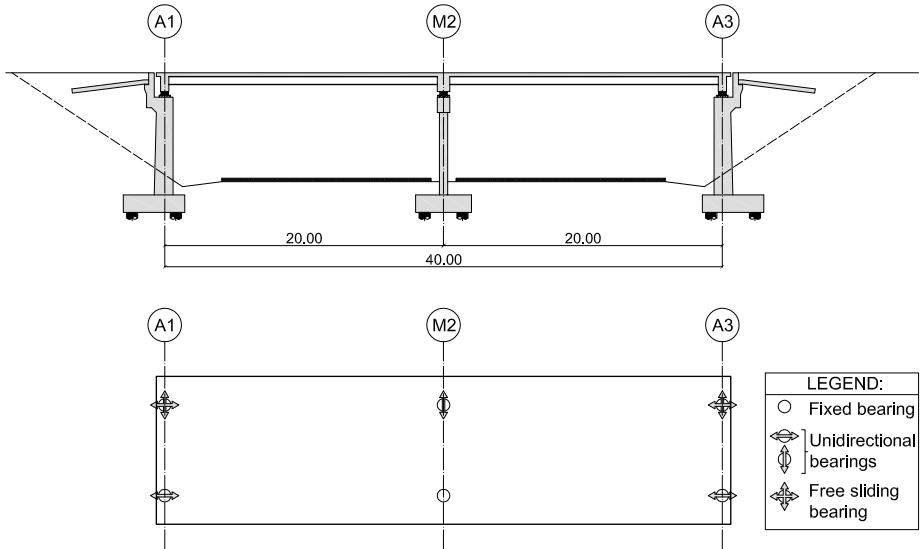
#### **6.1 Definition and description of the case study CS #2.1.1**

The second case study analysed is a typical highway overpass designed according to Eurocodes (CEN, 2005a, 2012b, 2006). The structural solution is a steel-concrete composite I-girders. In detail, the bridge is composed of two simply supported spans. Each spans is 20 m long, for a total length of 40 m. The road cross-section is 10.60 m wide, with a central carriageway 6.50 m wide and two sidewalks 2.05 wide, as shown in Figure 6.1. Four main I-girders HE600B sections, made of hot-rolled S460M steel and separated by 2.65 m distance, support the concrete slab. This component is 0.25 m thick and composed by C35/45 concrete and B450C reinforcing steel; the former and steel I-girders are full rigidly connected by means of Nelson stud connectors welded on the top steel flange. The connection between steel-concrete composite section (SCCS) girders of the two spans is guaranteed by a reinforced concrete cross-beam (CCB). The CCBs are 0.60 m and 0.90 m wide in correspondence of abutments and on the intermediate pier, respectively. The deck is simply supported by six normal bearings and such bearing configuration is shown in

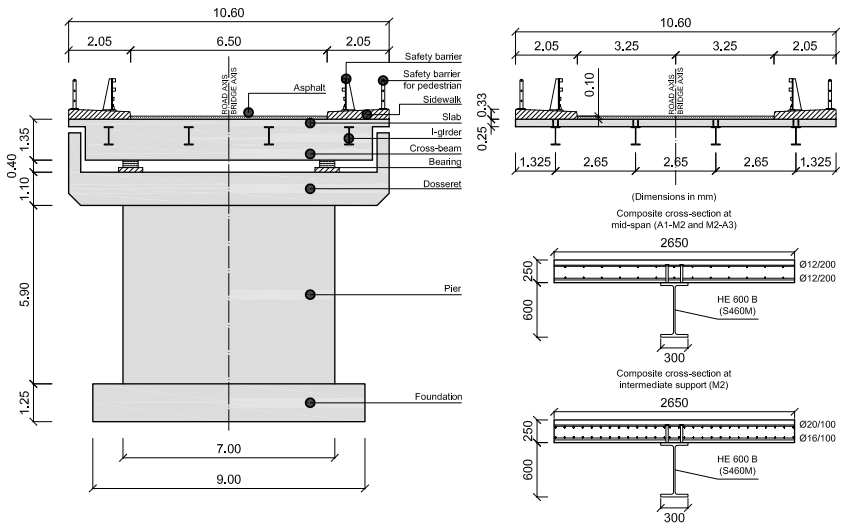
Figure 6.1(a). These device are designed in accordance to CEN (2006). The deck is fixed to the pier and a transversal movement is allowed by a unidirectional bearing, whilst a couple of free and longitudinal sliding bearings on the abutments permits the deck expansion in both directions. With this configuration, the bridge allows for the seismic movement of the deck and minimizes reaction forces both on the deck and abutments. As a result, the pier can undergo plastic deformations whilst the abutments remain in the linear regime. The pier is 7.00 m high, characterise by a 0.60x7.00 m rectangular transversal section. A deep foundation for the intermediate pier is chosen, due to the fact that it has a limited influence on the bridge's response. In order to minimize the construction phases of the steel-concrete composite deck, a procedure based on one-step pouring, typically used for small bridges, is adopted.

## **6.2 3D FE model and preliminary analysis of the bridge**

In order to calculate the stress distribution on the bridge owing to static and seismic loads, a 3D numerical model has been developed by using the commercial software SAP2000 (Computer and Structures, 2002), as shown in Figure 6.2. In the numerical analysis, it was taken into account the actual sequence of the construction phases, and hence which elements were active (steel girders only for the first step, steel girders supporting themselves and fresh concrete in the second step, and composite steel-concrete cross-section in the third step) and the effective elastic modulus of the concrete (short- and long-term loading). The total structural response of the bridge was given by the sum of each step. Table 6.1 summarises mechanical properties that are assigned to elements and calculated according to Eurocodes (CEN, 2005a,b,



(a)  
(Dimensions in m)



(b)

**Figure 6.1:** (a) Longitudinal and (b) transversal views of the case study CS #2.1.1

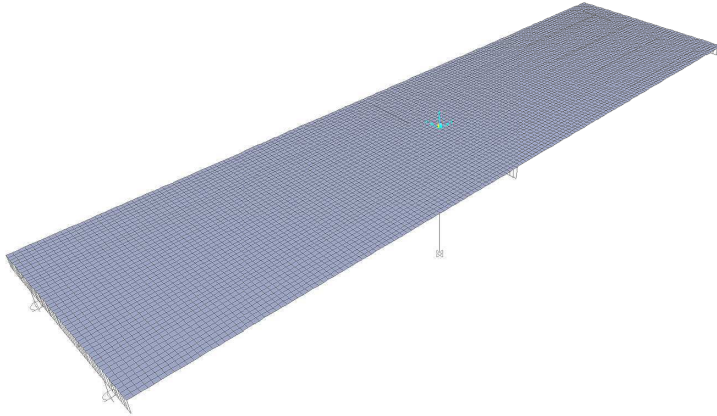


**Figure 6.2:** 3D modelling of the bridge case study CS #2.1.1

2012a).

The numerical model was essentially composed by a combination of three types of elements: *frame*, *shell* and *body*. Steel main girders, CCBs and the intermediate concrete pier were modelled through *frame* elements, whilst the concrete slab was assumed as a *shell* element. In order to perform a rigid connection between the concrete slab and steel girders without any slip, the connection system was modelled with *body* constraints. The two sidewalks and the asphalt layer were inserted by mean of vertical loads. The boundary conditions imposed by the bearing system were simply modelled by adding restraints on the abutments, while local constrains were introduced between the intermediate CCB and pier cap. As mentioned before, in order to extract useful and manageable results, the concrete pier was modelled with frame element. The pier was also assumed to be fully fixed to the foundation. Moreover, the cracked stiffness change of the SCCS have to be taken into account in the numerical model. A length of  $0.15L$ , where  $L$  is the span length, at each side of the

**Table 6.1:** Mechanical properties for the bridge model

Material	Type	$f_y$ (MPa)	$E$ (MPa)	$\nu$ (-)
Structural steel	S460M	460	200000	0.3
Reinforcing stel	B450C	450	200000	0.3
Concrete	C35/45	35	34077	0.2

**Table 6.2:** ULS actions and stresses on the composite section at the intermediate support

Component	Value	Unit
$M_{Ed}$	-2620	kNm
$V_{Ed}$	1040	kN
$\sigma_{a,Ed,top}$	186	MPa
$\sigma_{a,Ed,bot}$	-375	MPa

intermediate support was considered as cracked concrete zone (CEN, 2012b). Thus, the cracked analysis were performed on the bridge. In accordance with CEN (2002), the USL combination were adopted to obtain force and stress values in structural elements. Table 6.2 shows maximum values in terms of force, moment and stress of the most stressed steel-concrete composite beam at the intermediate support.

In order to understand the behaviour of the bridge subjected to a seismic loading, a modal analysis with design elastic spectra was achieved (CEN, 2006). A far field spectrum type 1 and a peak ground acceleration (PGA) equal to 0.25g were adopted. The class B was selected for soil characteristics. In

**Table 6.3:** Participant masses and periods for 13th and 14 modes of the bridge

Mode	$T$	$m_{i,UX}$	$m_{i,UY}$	$m_{i,UZ}$	$\sum_i m_{i,UX}$	$\sum_i m_{i,UY}$	$\sum_i m_{i,UZ}$
	(s)	(-)	(-)	(-)	(-)	(-)	(-)
13	0.067	0.00	0.22	0.00	0.87	0.23	0.67
14	0.062	0.00	0.57	0.00	0.87	0.79	0.67

**Table 6.4:** ULS seismic actions and stresses on the composite section at the intermediate support

Component	Value	Unit
$M_{3,Ed}$	90	kNm
$F_{1,Ed}$	200	kN
$\sigma'_s$	29.1	MPa
$\sigma_s$	31.4	MPa

detail, the seismic analysis was performed only in out-of-plane direction, i.e. along the y-axis. The fundamental period of the bridge was  $T_1 = 0.89$  sec (in longitudinal direction, i.e. x-axis), while in transversal direction (i.e. y-axis) there were two main eigenmodes, which excited 78.4% of the total mass of the bridge. Table 6.3 shows these periods and eigenmodes.

In order to maximise seismic effects to the bridge, the CQC loading combination was adopted. Table 6.4 shows maximum values in terms of force, moment and stress of the most stressed steel-concrete composite beam at the intermediate support due to seismic loading in out-of-plane direction. In detail,

stress values were referred to the top and bottom layer of longitudinal reinforcing steel in the concrete slab.

### **6.3 Design and verification of the CCB detail to static and seismic loading**

The focus of this section is to design and to verify the CCB that connects the composite steel-concrete beam spans. It is an important detail for three reasons: i) to ensure the continuity between spans; ii) to allow the transfer of shear forces and hogging bending moments from the deck to the substructure of the bridge; and iii) to allow a better transversal distribution of actions from the superstructure. Moreover, when a monolithic solution is adopted, the CCB and the cap beam member are the same element. However, the adoption of the CCB-detail solution involves some critical issues such as the identification of the internal local mechanism to transfer the stress between elements and the complexity in terms of executive feasibility.

#### **6.3.1 Standards on the design of the CCB joint solution**

The design of the CCB is described in DIN FB 104 (2009). Three types of solutions to realize the connection between steel-concrete composite section and CCB are reported, as shown in Figure 6.3. The design is thought only to satisfy static load prescriptions, therefore no further information about the seismic behaviour of these joints is provided. DIN FB 104 (2009) considers that longitudinal steel beam ends with a vertical steel head plate, whilst the bottom flange fits inside the CCB. With reference to the continuity joint, internal actions to SCCS-CCB interface are characterised by a hogging bending moment that

puts in tension the steel top flange, and by a shear force. Such moment could be decomposed in a pair of actions: the tension force  $Z$  is transferred from one side to the other by means of the concrete slab, while the compression force  $D$  is transmitted by means of contact between bottom flanges of the Variant A and B joint solutions, as depicted in Figure 6.3(a) and Figure 6.3(b), respectively. Since it is difficult to maintain the alignment of bottom flanges, a steel plate welds these elements together. The Variant C solution instead transfers the compression force through the contact between steel head vertical plate and CCB lateral surface, as shown in Figure 6.3(c).

In the Variant A and C, the shear force is transferred by shear studs welded on the vertical head plate, while in Variant B these studs are welded on a protrusion of the steel web inside the CCB. In all typologies, in order to equilibrate the system of forces between the tension in the concrete slab and the compression in the bottom steel flange, studs have to grasp these additional forces.

### **6.3.2 Description of innovative SCCS-CCB solutions**

The aforementioned CCB's configurations present several theoretical and constructional disadvantages. In Variant A and C, when the neutral axis of the SCCS cuts the girder's web, the studs near the concrete slab are subjected to tension force. Nowadays, there are not specific standards for shear-tension interaction law for the design of these studs. From a construction point of view, the protrusion inside the CCB could obstruct the correct placement of the reinforcing and impend the pouring of the fresh concrete. Moreover, the possibility of detection and repair of the CCB in case of failure appears very complicated. On the basis of the DIN FB 104 (2009), three innovative types of joint solutions are proposed adjusting both some details of the shear stud system, as well as

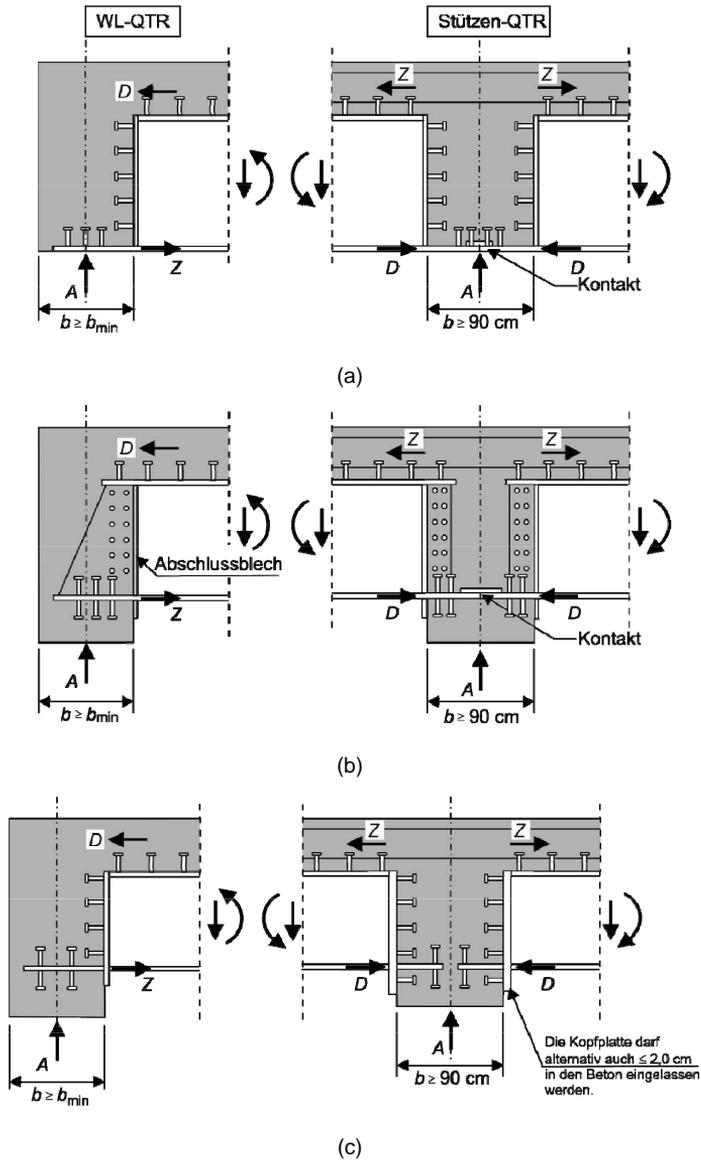


**Figure 6.3:** Typical configurations of CCB based on DIN FB 104 (2009): (a) Variant A, (b) Variant B, and (c) Variant C

the configuration of the protrusion of the steel web and the bottom flange inside the CCB. With reference to the design and verification of strut-and-tie mechanisms inside the CCB, prescriptions in CEN (2005a, 2012a) are followed. For checks on the stud system, CEN (2012b) are adopted, whilst in case of shear-tension interaction of studs the PCI (1991) are used.

#### **6.3.2.1 Cross-beam configuration: DIN FB 104 Var. C**

The steel girder ends with a head plate in the *DIN FB 104 Var.C* proposal, as shown in Figure 6.4(a) and Figure 6.4(b). The bottom flange protrudes inside the cross-beam for less than half the width of the concrete beam's cross section. Compression forces are transferred to the concrete as the flanges of the steel girders are not connected to each other. Tension forces are instead transferred through shear studs vertically disposed on the bottom flange protrusion. The flow of forces between the concrete deck and the steel beam is ensured by studs arranged on the girder's top flange. Shear studs on the head plate transfer forces to the cross-beam.

#### **6.3.2.2 Cross-beam configuration: DOMI1**

The detail type *DOMI1* was designed for cross-beams on bearings and although it is similar to *DIN FB 104 Var. B*, some important differences need to be pointed out, as shown in Figure 6.4(c) and Figure 6.4(d). First, the steel girder head plates are confined at the bottom flange region. Forces are transferred through contact (compression) or through shear studs (tension) to the CCB. Head plate thickness has to be chosen according to design force intensity. Another particular aspect of the configuration is represented by the steel

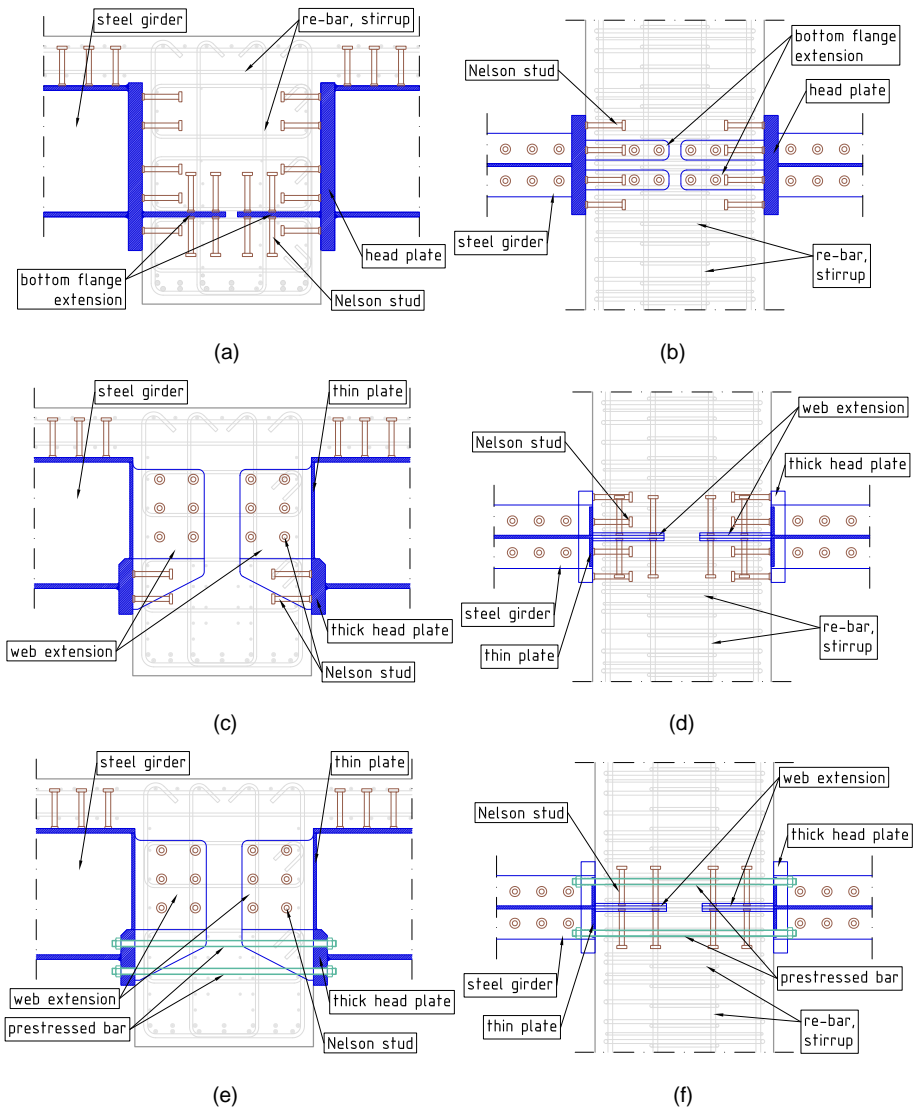


**Figure 6.4:** Concrete cross-beam configurations: (a) lateral and (b) top views of DIN FB 104 Var. C solution, (c) lateral and (d) top views of the DOMI1 solution, (e) lateral and (f) top views of the DOMI2 solution

girder's web extending into the cross-beam. Shear studs are arranged over the entire area and are subjected to pure shear (designed for entire shear force). The protrusion of the web is provided with holes for the placement of the CCB reinforcement. This detail type is designed for bottom steel flanges in light tension or compression. Such stress states are common for short to medium span bridges supported on bearings.

### **6.3.2.3 Cross-beam configuration: DOMI2**

Detail type *DOMI2* differs from the aforementioned *DOMI1* configuration in the bottom steel flange connection, as shown in Figure 6.4(e) and Figure 6.4(f). While compression forces are again transferred through contact via a thick head steel plate, tension is absorbed by four prestressed anchor bars. Shear forces are transferred through studs arranged on both sides of the steel beam web extension, whereas studs on the top flange transfer tensile and compression forces. This detail type is designed for bottom steel flanges where tension forces become significant and the use of shear studs is uneconomical. Bridges with a monolithic connection between cross-beam and pier can be subjected to this stress state.

### **6.3.3 Procedure to design and verify the CCB detail**

With the aim to follow a lineal process that allows to check all the components of the joint, the procedure proposed in Chabrolin et al. (2010) has been adopted. The flow chart given in Figure 6.5 is proposed. The actions to take into account in the design process derive from the linear elastic FE model in Section 6.2. In particular, the following internal actions in correspondence of

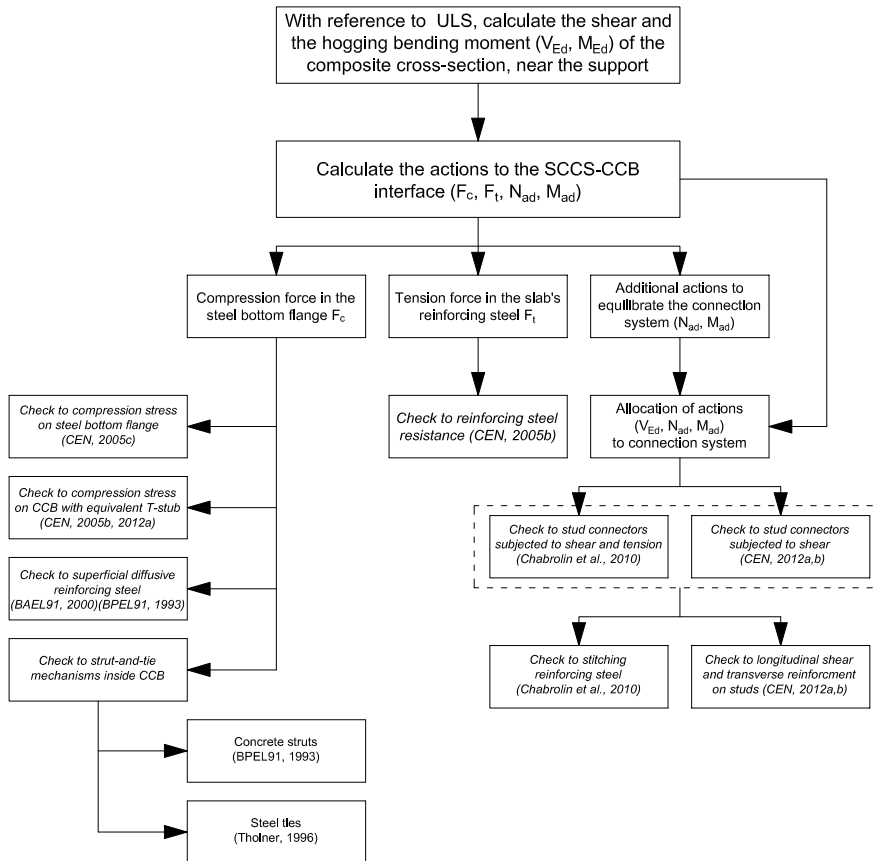


**Figure 6.5:** Flow chart for the SCCS-CCB interface verification

the intermediate support are required as input:

- $V_{Ed}$  shear force;
- $M_{Ed}$  hogging bending moment.

For the calculation, the following hypotheses are assumed:

1. Class of the steel section up to 3;
2. Maximum bending moment at ULS lower than resistance bending moment;
3. Linear stress distribution in correspondence to the SCCS-CCB interface;
4. Only the reinforcing steel inside the effective width of concrete flange for shear lag  $b_{eff}$  is considered in the slab;
5. Tension resistance of the concrete can be neglected.

The plastic neutral axis (PNA) of the SCCS beam is calculated using Equation 6.1:

$$z_{as,p} = \frac{z_a A_a + z_s A_{s,tot}}{A_a + A_{s,tot}} \quad (6.1)$$

where  $z_a$  is the centre of gravity of the steel section area  $A_a$ ,  $A_{s,tot} = A_s + A'_s$  is the tension reinforcing in the concrete slab of  $b_{eff}$  width, and  $z_s$  is the centre of gravity of reinforcing steel section  $A_s$  with reference to the outer surface of the bottom steel flange. The elastic neutral axis (ENA)  $z_{as}$  is calculated considering the hypotheses of partial section behaviour and neglected concrete tension resistance. Figure 6.6(a) shows the internal distribution of stress inside the SCCS, while Figure 6.6(b) illustrates the mechanism of transfer of  $V_{Ed}$

and  $M_{Ed}$  actions from the SCCS to the CCB. Such actions' migration could take place by means of:

- Tension force of reinforcing steel of concrete slab  $F_{t,Ed}$ . This action is placed in the centre of gravity of reinforcing steel  $z_s$ ;
- Contact between compression steel bottom flange and lateral surface of the CCB. It is assumed that the compression force  $F_{c,Ed}$  is placed in the middle of the steel bottom flange  $t_f/2$ ;
- The stud connection system transfers the shear force  $V_{Ed}$  and the additional actions, i.e.  $N_{ad}$  and  $M_{ad}$ , that arise to equilibrate the force system given that  $F_{t,Ed} \neq F_{c,Ed}$ . The additional actions are applied to the centre of gravity of the steel section  $z_a$ .

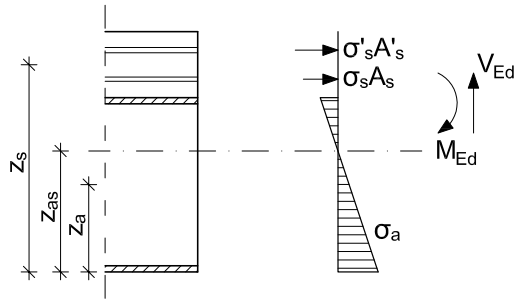
The depth of the neutral axis (NA) is calculated by means of setting the static moment  $S_{nn}$  equal to zero. Hence, if the NA  $z'_{as}$  cuts the web, the following Equation 6.2 holds:

$$S_{nn} = 0 \iff A_{s,tot}(z_s - z'_{as}) - t_w \left( \frac{z'_{as} - t_f}{2} \right)^2 - b_f t_f \left( z'_{as} - \frac{t_f}{2} \right) = 0 \quad (6.2)$$

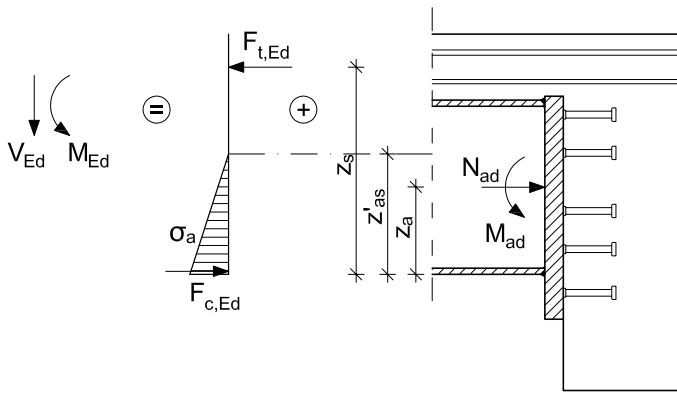
The moment of inertia of the section  $I'_2$  is obtained from:

$$I'_2 = A_{s,tot}(z_s - z'_{as})^2 + \frac{b_f t_f^3}{12} + \frac{t_w (z'_{as} - t_f)^3}{12} + t_w (z'_{as} - t_f) \left( \frac{z'_{as} - t_f}{2} \right)^2 + b_f t_f \left( z'_{as} - \frac{t_f}{2} \right)^2 \quad (6.3)$$

With reference to the SCCS-CCB section, Table 6.5 shows the depth of NA and the second moment of inertia. Forces transfer from SCCS to CCB interface are, respectively:



(a)



(b)

**Figure 6.6:** Stress distribution on (a) a generic SCCS beam, and on (b) a SCCS-CCB interface

**Table 6.5:** Geometrical properties of the SCCS-CCB interface

Component	Value	Unit
$z_s$	726.29	mm
$z_{as,p}$	443.17	mm
$z_{as}$	400.17	mm
$z'_{as}$	397.50	mm
$I'_2$	3.05E+9	mm <sup>4</sup>

- the tension force  $F_{t,Ed}$  in the slab is calculated with:

$$F_{t,Ed} = A_{s,tot} \sigma_s \quad (6.4)$$

where:

$$\sigma_s = -\frac{M_{Ed}}{I'_2} (z_s - z'_{as}) \quad (6.5)$$

- The compression force  $F_{c,Ed}$  in the steel bottom flange is determined with:

$$F_{c,Ed} = b_f t_f \sigma_{a,fb} \quad (6.6)$$

where:

$$\sigma_{a,fb} = \frac{M_{Ed}}{(z'_{as} - t_f/2) I'_2} \quad (6.7)$$

- With reference to the centre of gravity of the steel section, the additional efforts  $N_{ad}$  and  $M_{ad}$  are estimated:

**Table 6.6:** Stresses and forces from SCCS to CCB interface

Component	Value	Unit
$\sigma_s$	282.45	MPa
$\sigma_{a,fb}$	-328.59	MPa
$F_{t,Ed}$	3856.44	kN
$F_{c,Ed}$	-2957.28	kN
$N_{ad}$	-899.17	kN
$M_{ad}$	-133.20	kNm

- from the equilibrium to the translation, the additional axial force  $N_{ad}$  is:

$$N_{ad} = -(F_{t,Ed} - |F_{c,Ed}|) \quad (6.8)$$

- from the equilibrium to the rotation, the additional moment  $M_{ad}$  is:

$$M_{ad} = M_{Ed} + [ |F_{c,Ed}|(z_a - t_f/2) + F_{t,Ed}(z_s - z_a) ] \quad (6.9)$$

- The connection system is able to adsorb the shear force  $V_{Ed}$ . Moreover, due to the compression stress between the vertical steel plate and the CCB lateral surface, part of the this force could be transferred by friction.

Table 6.6 summarises numerical results of aforementioned equations.

### **6.3.4 ULS static verification of the DIN FB 104 Var. C cross-beam configuration**

On the basis of the flow chart displayed in Figure 6.5, all verifications on the SCCS-CCB details are proposed. In particular, the DIN FB 104 Var. C

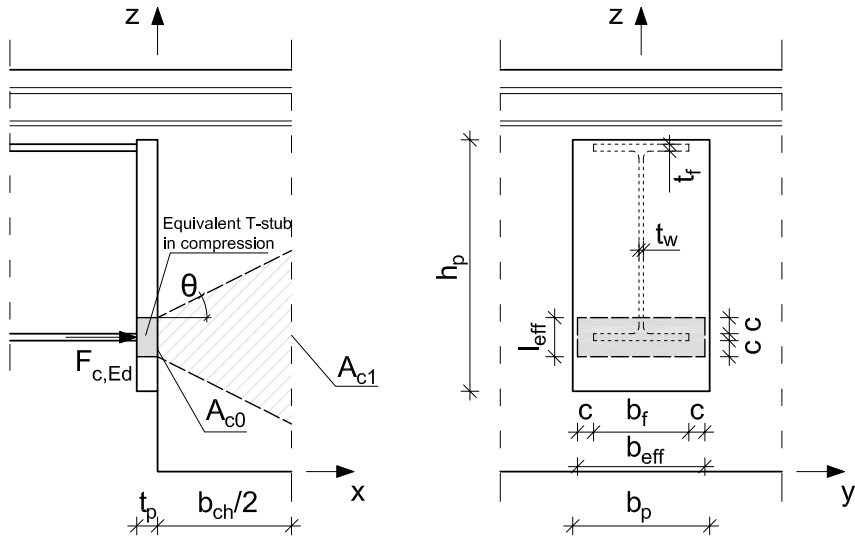


**Figure 6.7:** Equivalent T-stub in compression

cross-beam configuration is analysed.

#### 6.3.4.1 Check of the component stresses by $F_{c,Ed}$ and $F_{t,Ed}$

##### Steel bottom flange

In accordance with CEN (2005b), the compression stress in the middle of the steel bottom flange have to satisfy the following expression:

$$|\sigma_{a,fb}| \leq f_{ad} = 460 \text{ MPa} \quad (6.10)$$

Since  $|\sigma_{a,fb}| = 328.59$ , the verification is satisfied.

##### Equivalent T-stub in compression

The footprint load of the steel plate welded to the bottom flange have to be

sufficient to transfer the compression stress to the CCB lateral surface without penetration, i.e.:

$$|F_{c,Ed}| \leq F_{c,Rd} \quad (6.11)$$

The verification of the equivalent T-stub element in compression is performed in accordance with CEN (2005c). The compression strength resistance is calculated as follows:

$$F_{c,Rd} = f_{jd} b_{eff} l_{eff} \quad (6.12)$$

where:

$$b_{eff} = b_f + 2c;$$

$$l_{eff} = t_f + 2c;$$

$$c \leq t_p \sqrt{\frac{f_{yp}}{3f_{jd} \gamma_{M0}}} \text{ with:}$$

$f_{yp}$  is the design strength of the structural steel;

$f_{jd} = \alpha_{bf} \beta_j f_{cd}$  is the design bearing strength of the joint (CEN, 2005a)  
and with  $\beta = 2/3$ ;

$\alpha_{bf} = \sqrt{A_{c1}/A_{c0}}$  is a coefficient such that satisfies  $1 \leq \alpha_{bf} \leq 3$ ;

$A_{c0} = b_{eff} l_{eff}$  is the loaded area;

$A_{c1}$  is the maximum design distribution area with a similar shape to  $A_{c0}$ .

If the length of  $b_{ch}/2$  is assumed to be the effective length, as depicted in Figure 6.7:

$$A_{c1} = (b_{eff} + b_{ch} \tan \theta)(l_{eff} + b_{ch} \tan \theta) \quad (6.13)$$

where  $\theta$  is the inclination of the concrete strut, and it assumes values in the range of  $26.5 \leq \theta \leq 45$ . The design calculation of the  $A_{c0}$  and  $A_{c1}$  surfaces is iterative. In the first instance,  $\alpha_{bf} = 1.75$  is assumed.

Dimensions of the vertical steel plate have to satisfy:

- Equation 6.11;
- the minimum dimensions to allow the stress diffusion in the concrete cross-beam:

$$h_p \geq t_f + 2c = h_{p,min} \quad (6.14)$$

$$b_p \geq b_f + 2c = b_{p,min} \quad (6.15)$$

Table 6.7 summarises checks on the proposed solution.

#### **Strut-and-tie elements**

The compression force  $F_{c,Ed}$  that it is transferred from the bottom flange to the CCB has to be verified by means of a strut-and-tie mechanism. This mechanism is adopted for the verification of concrete and reinforcing steel strengths. With reference to BPEL91 (1993), the concrete strut is verified, while for the verification and the correct arrangement of diffusive reinforcements, Thonier (1996) and Migliacci and Mola (1984) are considered, respectively.

#### **Concrete strut**

In accordance with BPEL91 (1993), the design strength resistance of the concrete is assumed to be equal to  $f_{cd}$ . The following relationship have to be satisfied:

$$\sigma_c = \frac{|F_{c,Ed}|}{l_{eff}b_{eff}} \leq \sigma_{Rd,max} = 23.33 \text{ MPa} \quad (6.16)$$

In this case  $\sigma_c = 18.37$  MPa, the verification is satisfied.

**Table 6.7:** T-stub checks on the DIN FB 104 Var. C solution

Component	Value	Unit
$f_{yp}$	430	MPa
$t_p$	70	mm
$h_p$	770	mm
$b_p$	550	mm
$c$	146	mm
$b_{eff}$	500	mm
$l_{eff}$	322	mm
$\alpha_{bf}$	2.13	-
$F_{c,Rd}$	5328	kN
$ F_{c,Ed} $	2957.28	kN
$f$	0.56	-

### **Steel tie**

The stress distribution occurs in a 2D manner. Due to this fact, reinforcements in both y- and z-direction have been calculated. More specifically, in z-direction the compression effort rests on an effective length  $l_{eff} = t_f + sc$ . Thonier (1996) assumes that  $b_{ch} \leq 2l_{eff}$ , as shown in Figure 6.8(a). Hence, in order to allow the development of the concrete strut in xz-plane, the following criterion has been satisfied:

$$l_{eff} \leq \frac{b_{ch}}{2} \leq l_{eff} + b_{ch} \tan \theta \leq h' \quad (6.17)$$

where  $h_{chb}$  is the distance between the force  $F_{C,Ed}$  and the outer fiber of the CCB. The tension force in the xz-plane in the steel tie is equal to:

$$T_z = \frac{F_{C,Ed} \tan \theta}{2} \quad (6.18)$$

The reinforcement in z-direction has to be greater than:

$$A_{se,z} \geq A_{se,z,req} = \frac{|F_{C,Ed}| \tan \theta}{2f_{sd}} \quad (6.19)$$

These reinforcements have to be included in the following range:

$$0.2 \frac{b_{ch}}{2} \leq s \leq 0.8 \frac{b_{ch}}{2} \quad (6.20)$$

As in the z-direction, in the y-direction the compression effort rests on an effective length  $b_{eff}$ . As shown in Figure 6.8(b), in order to allow the development of the concrete strut in xy-plane, the following criterion has been satisfied:

$$\frac{b_{ch}}{2} \leq b_{eff} \leq b_{eff} + b_{ch} \tan \theta \leq b' \quad (6.21)$$

The tension force in the xy-plane in the steel tie is equal to:

$$T_y = \frac{F_{C,Ed} \tan \theta}{2} \frac{b_{ch}}{2b_{eff}} \quad (6.22)$$

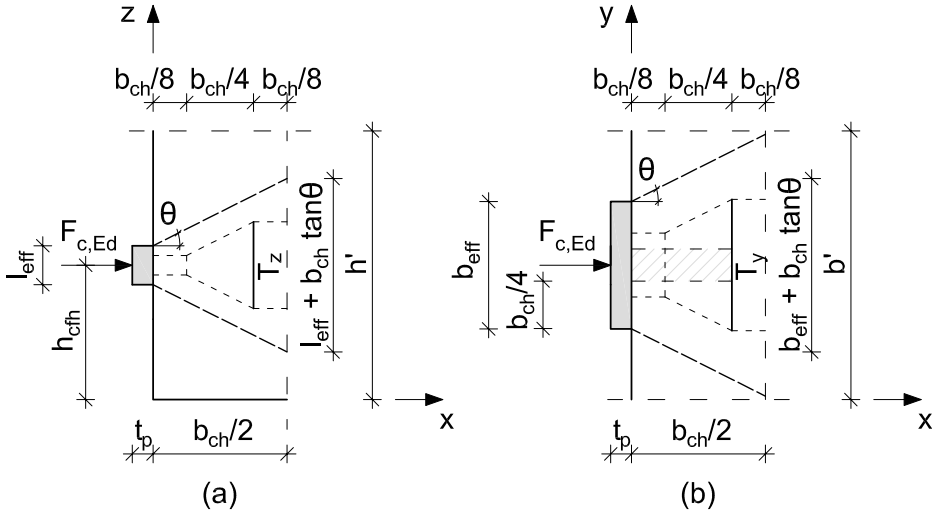


**Figure 6.8:** Strut-and-tie mechanism in (a) xz plane, and (b) xy plane

The reinforcement in y-direction has to be greater than:

$$A_{se,y} \geq A_{se,y,req} = \frac{|F_{c,Ed}| b_{ch} \tan \theta}{4 b_{eff} f_{sd}} \quad (6.23)$$

Table 6.8 and Table 6.9 summarise the quantity of reinforcing steel to be necessary for the CCB in order to propagate the stress from the bottom steel flange.

### Surface reinforcement

In accord with BAEL91 (2000) and BPEL91 (1993), under the steel plate a surface reinforcement has to be placed, such that:

$$A_{s,surf,req} = \frac{0.04 |F_{c,Ed}|}{f_{sd}} \quad (6.24)$$

In this case, the required surface reinforcement has to be equal to 302.30 mm<sup>2</sup>. The effective reinforcement placed in z-direction is equal to 1φ20=314 mm<sup>2</sup>,

**Table 6.8:** Diffusive reinforcement in z-direction for DIN FB104 Var. C solution

Component	Value	Unit
$h_{chf}$	515	mm
$b_{ch}$	900	mm
$\theta$	26.50	deg
$l_{eff}$	322	mm
$b_{ch}/2$	450	mm
$l_{eff} + b_{ch} \tan \theta$	770.72	mm
$h'$	1030	mm
$A_{se,z}$	$7\phi 16+2\phi 20=2035$	$\text{mm}^2$
$A_{se,z,req}$	1884	$\text{mm}^2$

**Table 6.9:** Diffusive reinforcement in y-direction for DIN FB104 Var. C solution

Component	Value	Unit
$h_{chf}$	515	mm
$b_{ch}$	900	mm
$\theta$	26.50	deg
$b_{ch}/2$	450	mm
$b_{eff}$	460	mm
$b_{eff} + b_{ch} \tan \theta$	908.72	mm
$b'$	2650	mm
$A_{se,y}$	$8\phi 16+1\phi 20=1922$	$\text{mm}^2$
$A_{se,y,req}$	1843	$\text{mm}^2$

while in  $y$ -direction it is equal to  $2\phi 16=402 \text{ mm}^2$ . Both verifications are satisfied.

### Reinforcing steel in tension in the slab

With reference to CEN (2005a), in order to verify if the tension on longitudinal reinforcement in the slab, the Equation 6.25 has to be satisfied:

$$\sigma_s \leq f_{sd} = 391.3 \text{ MPa} \quad (6.25)$$

Since  $\sigma_s = 282.45 \text{ MPa}$ , the verification is satisfied.

#### 6.3.4.2 Stress design of the connector system

On the basis of the linear distribution of normal stresses between the vertical steel plate and the CCB, the calculation of actions in the studs is provided. This distribution is determined in accordance with Chabrolin et al. (2010). The main hypothesis is the assumption of the depth of NA equal to  $z_c = 1/3(z_{as} - t_f)$ , as depicted in Figure 6.9.

The following symbols are defined:

$n_{col}$  is the number of columns of the connectors considered;

$n_{rig}$  is the number of rows of the connectors considered;

$n_{con,gr} = n_{col}n_{rig}$  is the number of connectors considered in the group;

$n_{tot}$  is the total number of the connectors.

General actions on the  $i$ -th connector are obtained by means of the sum of design forces:

- axial force caused by the additional force  $F(N_{ad,i})$ :

$$F(N_{ad,i}) = N_{ad}/n_{tot} \quad (6.26)$$

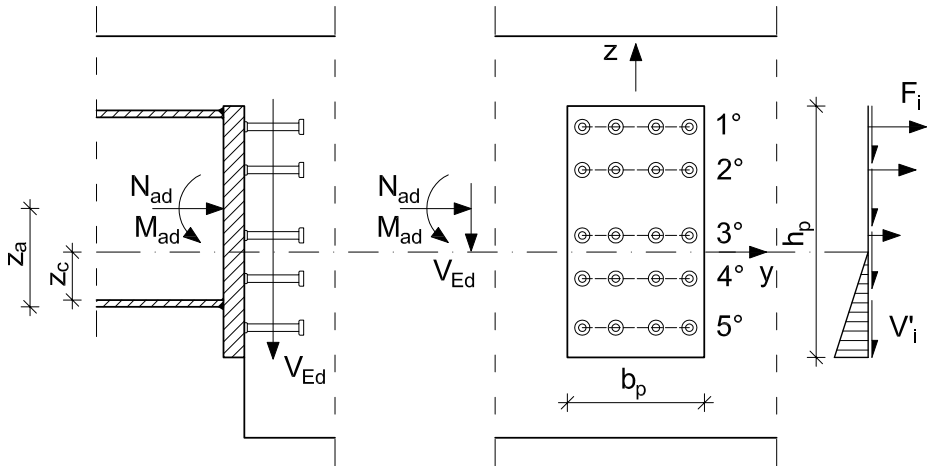


**Figure 6.9:** Distribution of forces on the connector system in DIN FB104 Var.C solution

- axial force due to the additional moment  $F(M_{ad,i})$ :

$$F(M_{ad,i}) = \frac{|M_{ad}|y_i}{\sum_{i=1}^{n_{tot}} y_i^2} \quad (6.27)$$

- shear force  $V'_i$ , that it could be calculated with the assumption of uniform distribution of shear stresses:

$$V'_i = -\frac{|V_{Ed}| - F_{f,Rd}}{n_{tot}} \quad (6.28)$$

where  $F_{f,Rd}$  is the friction force between the vertical plate and the CCB. With reference to CEN (2005c), such force can be computed as follows:

$$F_{f,Rd} = C_{f,d}|F_{c,Ed}| \quad (6.29)$$

with  $C_{f,d} = 0.2$ . In this case, it results that  $F_{f,Rd} = 591.46$  kN and so  $V'_i = -22.43$  kN.

**Table 6.10:** Neutral axis of head steel plate for DIN FB104 Var. C solution

Component	Value	Unit
$b_p$	500.00	mm
$h_p$	785.00	mm
$z_c$	137.72	mm

**Table 6.11:** Maximum tension forces on a single stud connector for DIN FB104 Var. C solution

Component	Value	Unit
$F(N_{ad,i})$	-44.96	kN
$F(M_{ad,i})$	46.47	kN

Table 6.10 shows geometrical characteristics of the vertical plate and the depth of NA. Table 6.11 and Table 6.12 summarise normal actions, that are calculated with aforementioned equations, in case of failure of the single stud connector and a group of stud connectors, respectively. Where requested, the verification for shear-tension interaction of the connector system has been provided.

#### **6.3.4.3 Tension resistance of connectors**

In the case of tension stresses, the verification of stud connectors could be calculated taking into account two different failure mechanisms: i) the collapse for tension in the stud, or b) the pull-out of the concrete cone, as shown in Figure 6.10. With reference to a group of stud connectors, the failure of the

**Table 6.12:** Maximum tension forces on a group of stud connectors for DIN FB104 Var.  
C solution

Component	1° row	1° + 2° rows	Unit
	Value		
$n_{col}$	4	4	-
$n_{row}$	1	2	-
$n_{con,gr}$	4	8	-
$F(N_{ad,gr})$	-179.83	-359.67	kN
$F(M_{ad,gr})$	185.88	310.13	kN
$F(N_{ad,gr}) + F(M_{ad,gr})$	6.04	-49.54	kN

joint could occur due to the collapse of a part of the connector system. PCI (1991) is used to determine the tension resistance of connectors.

#### **Tension resistance of a single head stud**

The tension resistance of a connector for the steel failure is given by:

$$P_{ten,Rd}^{(1)} = \frac{\pi d^2}{4} f_y \quad (6.30)$$

Whereas, the tension resistance of a connector for the pull-out of a concrete cone is given by (see Figure 6.10(a)):

$$P_{ten,Rd}^{(2)} = 0.89(h_{sc} - k)(h_{sc} - k - d_2)\sqrt{f_{ck}} \quad (6.31)$$

where  $k$  and  $d_2$  are the height and the diameter of the head stud, respectively. Hence, the tension resistance values obtained of a single stud are  $P_{ten,Rd}^{(1)} = 171.81$  kN and  $P_{ten,Rd}^{(2)} = 225.69$  kN.

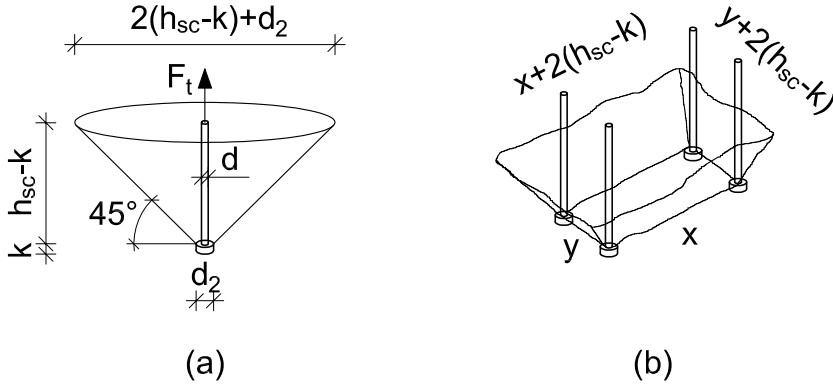


**Figure 6.10:** Failure mechanisms to pull-out of the concrete cone for (a) a single stud, and (b) a group of studs

### Tension resistance of a group of head studs

Figure 6.10(b) shows the failure of a group of studs due to the pull-out of a concrete cone. The tensile strength of such mechanism is calculated as follows.

$$h_{min} = \frac{\min(x; y) + 2(h_{sc} - k)}{2} \quad (6.32)$$

where  $x = [(n_{col} - 1)p_1 + d]$  and  $y = [(n_{row} - 1)p_2 + d]$ . The failure mechanism could developed in two different ways.

If  $\frac{b_{ch}}{2} \geq h_{min}$ :

$$P_{ten,gr,Rd}^{(2)} = 0.223\sqrt{f_{ck}}[x + 2(h_{sc} - k)][y + 2(h_{sc} - k)] \quad (6.33)$$

If  $\frac{b_{ch}}{2} < h_{min}$ :

$$P_{ten,gr,Rd}^{(2)} = 0.223\sqrt{f_{ck}}\{[x + 2(h_{sc} - k)][y + 2(h_{sc} - k)] - A_R\} \quad (6.34)$$

where  $A_R = [x + 2(h_{sc} - k) - b_{ch}][y + 2(h_{sc} - k) - b_{ch}]$ . Hence, the lower value of the tension resistance of studs group is  $P_{ten,gr,Rd}^{(2)} = 410.43$  kN, and it has

been calculated in the first connector row.

#### 6.3.4.4 Check of the connector system

##### Shear-tension interaction

In accordance with CEN (2012b), if the tension force  $F_{ten}$  on studs is lower than 10% of its shear resistance, it is possible to neglect the tension force during the connector system verification. Otherwise, it can be taken into account by following the indications provided in PCI (1991). Due to the actions transferred to the joint and to the connector system properties, the ratio  $F_{ten}/P_{Rd}$  results to be equal to 0.11; hence, the shear-tension interaction has to be taken into account.

##### Check of single steel stud failure

For the verification of the single stud, the shear-tension interaction can be evaluated by means of:

$$s_{ten,Rd}^{(1)} = \frac{1}{\phi_1} \left[ \left( \frac{F(N_{ad,i}) + F(M_{ad,i})}{P_{ten,Rd}^{(1)}} \right)^2 + \left( \frac{V'_i}{P_{Rd}^{(1)}} \right)^2 \right] \leq 1 \quad (6.35)$$

where  $\phi_1 = 0.9$ . Since in the most stressed stud  $s = 0.03 \leq 1$ , the verification is satisfied.

##### Check of concrete failure

For the verification of the pull-out of the concrete cone, the shear-tension interaction can be evaluated by means of:

$$s_{ten,Rd}^{(2)} = \frac{1}{\phi_2} \left[ \left( \frac{F(N_{ad,i}) + F(M_{ad,i})}{P_{ten,Rd}^{(2)}} \right)^2 + \left( \frac{V'_i}{P_{Rd}^{(2)}} \right)^2 \right] \leq 1 \quad (6.36)$$

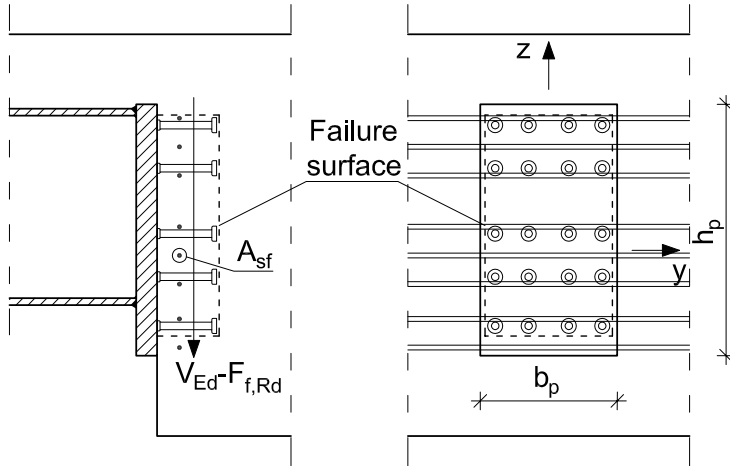


**Figure 6.11:** Failure surface for longitudinal shear and transversal reinforcements of the connector system in DIN FB104 Var.C

where  $\phi_2 = 0.85$ . Since in the most stressed stud  $s = 0.02 \leq 1$ , the verification is satisfied.

### Check of concrete pull-out of a group of connectors

For the verification of the concrete failure due to a group of connectors, the shear-tension interaction can be evaluated by means of:

$$s_{ten,gr,Rd}^{(2)} = \frac{1}{\phi_2} \left[ \left( \frac{F(N_{ad,gr}) + F(M_{ad,gr})}{P_{ten,gr,Rd}^{(2)}} \right)^2 + \left( \frac{V'_i}{P_{Rd}^{(2)}} \right)^2 \right] \leq 1 \quad (6.37)$$

Equation 6.37 has to be applied to all connectors in tension. Since only the first row is in tension with  $s = 0.02 \leq 1$ , the verification is satisfied.

### 6.3.4.5 Longitudinal shear and transversal reinforcement

In order to avoid the failure of the concrete due to sliding or longitudinal cracking, the shear force from the connector system has to be absorbed by a suitable reinforcement. With reference to CEN (2012b), the transversal reinforcement has to satisfy the following criterion:

$$A_{sf}f_{sd}/s_f > v_{Ed}h_f/\cot\theta_f \quad (6.38)$$

Moreover, the shear stress has to be involved:

$$v_{Ed} < v f_{cd} \sin\theta_f \cos\theta_f \quad (6.39)$$

The inclination of the concrete strut is calculated in agreement with CEN (2005a):

$$1 \leq \cot\theta_f \leq 2 \quad \text{for the slab in compression} \quad (6.40a)$$

$$1 \leq \cot\theta_f \leq 1.35 \quad \text{for the slab in tension} \quad (6.40b)$$

The connector system is stressed by a shear force  $V = V_{Ed} - F_{f,Rd}$ , as indicated in Figure 6.11. Table 6.13 summarises the data regarding the reinforcement placed in the CCB and the shear stress, while Table 6.14 gathers the verifications.

### 6.3.4.6 Check of stitching reinforcement

If some studs are subjected to tension force, the CCB could transfer this force without arriving concrete failure. With reference to the most stressed row of connectors, the stitching reinforcement is determined as follows:

$$A_{s,t,req} = \frac{n_{col}[F(N_{ad}) - F(M_{ad})]_{max}}{f_{sd}} \quad (6.41)$$

**Table 6.13:** Longitudinal shear in the connector system for DIN FB104 Var.C solution

Component	Value	Unit
$\phi$	16	mm
$s_f$	112.50	mm
$A_{sf}$	201.06	mm <sup>2</sup>
$\cot \theta_f$	1.25	-
$v_{Ed}$	0.875	MPa

**Table 6.14:** Check of longitudinal shear in the connector system for DIN FB104 Var.C solution

Equation 6.38	699.35	>	139.76
Equation 6.39	0.88	<	5.87

Table 6.15 summarises the required reinforcing steel placed in the CCB.

**Table 6.15:** Stitching reinforcement for DIN FB104 Var.C solution

Component	Value	Unit
$\phi$	16	mm
$n$	6	-
$A_{s,t}$	1206.37	mm <sup>2</sup>
$A_{s,t,req}$	15.45	mm <sup>2</sup>

### 6.3.5 ULS static verification of DOMI1 and DOMI2 cross-beam configurations

It is assumed that for static loads DOMI1 and DOMI2 CCB joint solutions are characterised by the same resistance.

#### 6.3.5.1 Check of the component stresses by $F_{c,Ed}$ and $F_{t,Ed}$

Some verifications are the same of the previous joint solution, such as the checks of the steel bottom flange, of the superficial reinforcement and of the longitudinal reinforcement in the concrete slab. Thus, they can be assumed to be valid for these joint solutions.

#### Equivalent T-stub in compression

As reported in Section 6.3.4.1, the check consists in verifying whether the dimensions of the steel bottom plate are adequate to transfer the compression force from it to the CCB lateral surface. In this case, the verification is satisfied, as emphasised in Table 6.16.

**Table 6.16:** T-stub checks on DOMI1 and DOMI2 solutions

Component	Value	Unit
$f_{yp}$	430	MPa
$t_p$	70	mm
$h_p$	280	mm
$b_p$	460	mm
$c$	80	mm
$b_{eff}$	460	mm
$l_{eff}$	280	mm
$\alpha_{bf}$	2.27	-
$F_{c,Rd}$	4543	kN
$ F_{c,Ed} $	2957.28	kN
$f$	0.65	-

**Table 6.17:** Diffusive reinforcement in z- and y-direction for DOMI1 and DOMI2 solutions

Component	Value	Unit
$A_{se,z}$	$7\phi 16+2\phi 20=2036$	$\text{mm}^2$
$A_{se,z,req}$	1884	$\text{mm}^2$
$A_{se,y}$	$9\phi 16+1\phi 12=1922$	$\text{mm}^2$
$A_{se,y,req}$	1883	$\text{mm}^2$

### Strut-and-tie elements

#### Concrete strut

In accordance with BPEL91 (1993), the design strength resistance of the concrete is assumed to be equal to  $f_{cd}$ . The following relationship has to be satisfied:

$$\sigma_c = \frac{|F_{c,Ed}|}{l_{eff}b_{eff}} \leq \sigma_{Rd,max} = 23.33 \text{ MPa} \quad (6.42)$$

Since  $\sigma_c = 22.96 \text{ MPa}$ , the verification is satisfied.

#### Steel tie

The stress distribution occurs in a 2D manner. Due to this fact, reinforcements in both z- and y-direction have been calculated, as proposed by Thonier (1996). Table 6.17 summarises the quantity of reinforcing steel required for in the CCB to propagate the stress transmitted by the steel bottom flange.

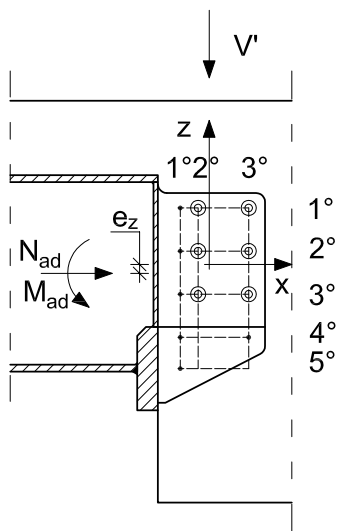


**Figure 6.12:** Instantaneous centre for connector system of DOMI1 and DOMI2 solutions

### 6.3.5.2 Stress design of the connector system and bars

The connection system between the steel beam and the CCB is composed of shear studs welded on the protrusion of the steel web and steel bars, that pass through the web's protrusion.

The hypothesis that web's protrusion and CCB are more stiff than connectors and bars is assumed. Moreover, these elements are considered to be elastic. With reference to the the shear stiffness of the connector system, the distribution of actions is calculated. Torque  $T$  and shear actions  $N_{ad}$  and  $V'$  stress the connector system. Torque is given by the sum of additional moment  $M_{ad}$  and the transport contribution  $N_{ad}e_z$ , as follows:

$$T = M_{ad} + N_{ad}e_z \quad (6.43)$$

On each element of the connector system, i.e. studs and bars (indicated with  $c_-$  and  $b_-$ , respectively), torque causes two orthogonal shear actions  $V_{T,x,i}$  and  $V_{T,z,i}$ . Due to the fact that the shear stiffness is proportional to the transversal section of the element  $A_i$ , in order to evaluate the shear distribution caused by the torque following relationships are proposed:

$$\begin{aligned} V_{T,x,i} &= \frac{Tz_i A_i}{n_V \sum_{i=1}^{n_{tot}} A_i (x_i^2 + z_i^2)} \\ V_{T,z,i} &= \frac{Tx_i A_i}{n_V \sum_{i=1}^{n_{tot}} A_i (x_i^2 + z_i^2)} \end{aligned} \quad (6.44)$$

where  $n_V$  is the number of the shear plane (in this case  $n_V = 2$ ).

On the basis of the shear stiffness,  $N_{ad}$  and  $V'$  actions are distributed as fol-

lows:

$$\begin{aligned}
 V_{x,i} &= \frac{N_{ad}A_i}{n_V \sum_{i=1}^{n_{tot}} A_i} \\
 V_{z,i} &= -\frac{(|V_{Ed}| - F_{f,Rd}) A_i}{n_V \sum_{i=1}^{n_{tot}} A_i}
 \end{aligned}
 \tag{6.45}$$

The total shear force to each element is calculated with the Equation 6.46 and they are summarised in Table 6.18.

$$V_i = \sqrt{(V_{x,i} + V_{T,x,i})^2 + (V_{z,i} + V_{T,z,i})^2} = \sqrt{V_{x,i,t}^2 + V_{z,i,t}^2}
 \tag{6.46}$$

**Table 6.18:** Shear forces on the connector system for DOMI1 and DOMI2 solutions

Element	$V_{z,i,t}$ kN	$V_{x,i,t}$ kN	$V_i$ kN
b11	3.99	-0.13	3.99
c12	-9.34	-0.32	9.35
c13	-63.41	-0.32	63.41
b21	3.99	-16.42	16.89
c22	-9.34	-40.08	41.15
c23	-63.41	-40.08	75.01
b31	3.99	-32.70	32.94
c32	-9.34	-79.84	80.38
c33	-63.41	-79.84	101.95
b41	3.99	-48.98	49.15
b43	-25.97	-48.98	55.44
b51	3.99	-61.88	62.01

**Table 6.19:** Shear resistance of the transversal bar

Component	Value	Unit
$\phi$	16	mm
$f_u$	450	MPa
$k_{Ry}$	0.8	-
$P_{Rd}^{(1)}$	57.91	kN
$P_{Rd}^{(2)}$	64.86	kN
$P_{Rd}$	57.91	kN

### 6.3.5.3 Design and verification of the shear resistance of bars

The design shear resistance of transversal reinforcement is calculated in accordance with Chabrolin et al. (2010).

$$P_{Rd} = \min \left( P_{Rd}^{(1)}, P_{Rd}^{(2)} \right) \quad (6.47)$$

where:

$$P_{Rd}^{(1)} = k_{Ry} f_u \frac{\pi \phi^2}{4} \frac{1}{\gamma_V} \quad \text{steel failure} \quad (6.48a)$$

$$\text{with } k_{Ry} = 0.8 - 0.025(\phi - 16)$$

$$P_{Rd}^{(2)} = 0.29 \alpha \phi^2 \sqrt{f_{ck} E_{cm}} \frac{1}{\gamma_V} \quad \text{concrete failure} \quad (6.48b)$$

Table 6.19 and Table 6.20 show the shear resistance of the transversal bar and the verification of the entire connection system, respectively.

Even though the  $b_{51}$  does not satisfy the shear verification, no plastic redistribution of shear forces is taken into account. Thus, forces on the connector system could be less than the ones actually calculated.

**Table 6.20:** Check of the connector system and bars for DOMI1 and DOMI2 solutions

Element	$f$
$b_{11}$	0.07
$c_{12}$	0.07
$c_{13}$	0.45
$b_{21}$	0.29
$c_{22}$	0.29
$c_{23}$	0.53
$b_{31}$	0.57
$c_{32}$	0.57
$c_{33}$	0.72
$b_{41}$	0.85
$b_{43}$	0.96
$b_{51}$	1.07

### 6.3.5.4 Longitudinal shear and transversal reinforcement

As for the Section 6.3.4.5, it is mandatory to arrange the reinforcement such that adsorb the concrete strut stress caused by shear stud connectors. With reference to CEN (2012b), Table 6.21 gathers numerical results, while Table 6.22 summarises verifications adopted.

**Table 6.21:** Reinforcement  $A_{sf}$  and shear stress  $v_{Ed}$  calculation for DOMI1 and DOMI2 solutions

Component	Value	Unit
$\phi_x$	12	mm
$s_{f,z}$	300	mm
$n$	3	-
$A_{sf,x}$	339	mm <sup>2</sup>
$\cot \theta_f$	1.25	-
$v_{Ed,z}$	1.574	MPa
$\phi_z$	16	mm
$s_{f,x}$	125	mm
$n$	2	-
$A_{sf,z}$	402	mm <sup>2</sup>
$\cot \theta_f$	1.25	-
$v_{Ed,x}$	2.890	MPa

**Table 6.22:** Check of longitudinal shear  $v_{Ed,z}$  and  $v_{Ed,x}$  in the connector system for DOMI1 and DOMI2 solutions

z-direction	Equation 6.38	442.6	>	251.28
	Equation 6.39	1.57	<	5.87
x-direction	Equation 6.38	1258.82	>	416.46
	Equation 6.39	2.89	<	5.87

### 6.3.6 ULS seismic verification of innovative cross-beam configurations

The ULS seismic loading combination that stressing the innovative joint has already been calculated in Section 6.2. With reference to seismic verifications, the innovative solutions are evaluated in the same manner.

In accord with CEN (2006), the seismic design of the bridge has to be such that damages of the deck are avoided. Under ULS seismic loading combination, in case of lack of significant yielding of the deck, the verification is guaranteed. In practice, the deck remains in elastic field.

The joint verification could be obtained by checking the stress in the concrete slab.

#### 6.3.6.1 Check of tensile strength of longitudinal reinforcement in the concrete slab

For this verification to hold, it is necessary to avoid the development of any yield in the longitudinal reinforcement. Design seismic actions could be obtained from Table 6.4, whilst static contribution could be evaluated with the procedure reported in Section 6.3.3; the latter provides, top and bottom longitu-

dinal reinforcement stresses of 116 kN and 81.1 kN, respectively, for a bending moment of  $M_{2,Ed} = 950$  kN.

The maximum stress in the reinforcing steel is the sum of seismic and static contributions, i.e. 145.1 kN. Since it is less than the  $f_{sd}$ , the deck remains in elastic field.

### **6.3.6.2 Check of shear resistance of concrete slab**

The transversal shear  $F_{2,Ed}$  is absorbed by the reinforcing concrete slab. The longitudinal reinforcement placed near the lateral edge of the slab is composed by  $\phi 20$  and  $\phi 16$ , to whom corresponds a shear resistance of  $V_{Rd,c} = 192.7$  kN. Since  $F_{2,Ed} = 150$  kN, the verification is satisfied.

## **6.4 Selection of the representative subassembly specimen based on preliminary numerical analysis**

In order to reproduce a significant level of stresses and strains, a specimen derived from a representative part of the full bridge was obtained. Analyses performed with the SAP2000 software (Computer and Structures, 2002) allowed to extrapolate a significant substructure of the bridge to be tested in the laboratory. With the aim of identifying a suitable substructure model that takes into account both the best match with modal analysis results and laboratory space availability, three type of substructures were investigated, as shown in Figure 6.13.

As clearly shown in Figure 6.14(a) and Figure 6.14(b), the *Submodel A* was able to well represent the out-of-plane bending moment  $M_3$ , whilst inaccurate results were achieved in terms of the shear force  $F_2$ . Also the *Submodel B*

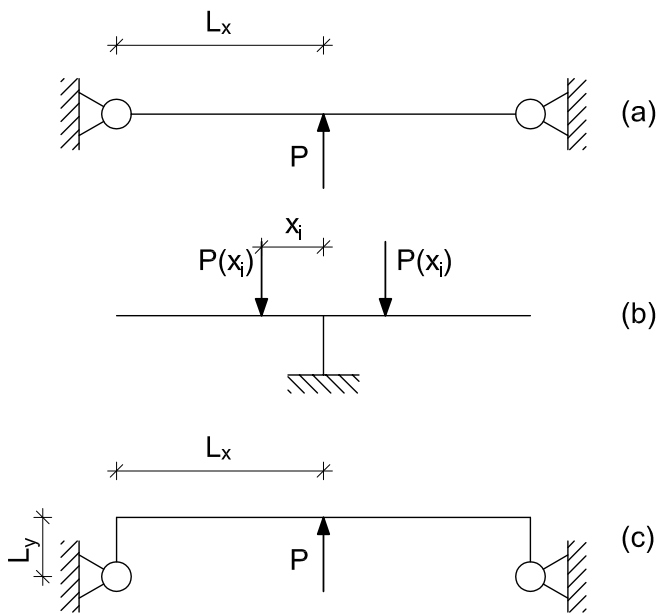


**Figure 6.13:** Submodel types: (a) submodel A, (b) submodel B, and (c) submodel C

was not able to recreate both bending moment and shear force, as depicted in Figure 6.15(a) and Figure 6.15(b). Moreover, neither model configurations was able to reproduce axial force in the specimen.

The *Submodel C* instead not only provided good results in terms of moment (see Figure 6.16(a)) but also was able to emulate part of the axial force. However, this configuration was deemed to be difficult to realize in the laboratory, due to several construction issues that could influence test results.

In light of these considerations and owing to its simply feasibility from the constructional point of view, the *Submodel A* was chosen as the representative substructure of the bridge.

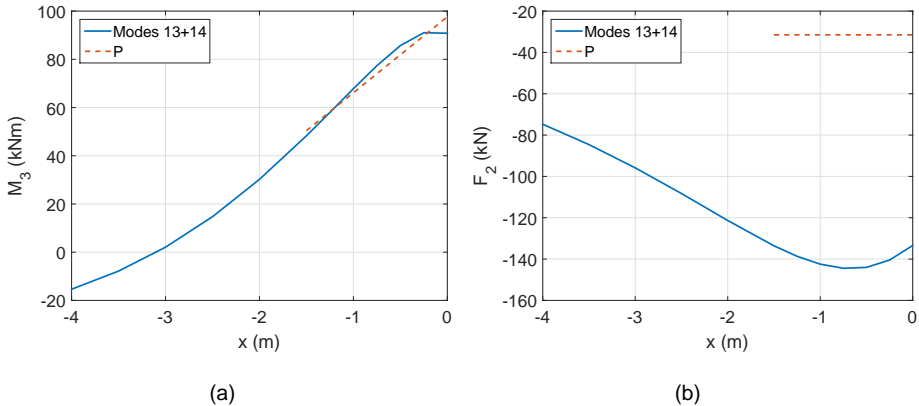


**Figure 6.14:** (a) Out-of-plane bending moment  $M_3$ , and (b) shear force  $F_2$  comparison between Submodel A and full bridge model

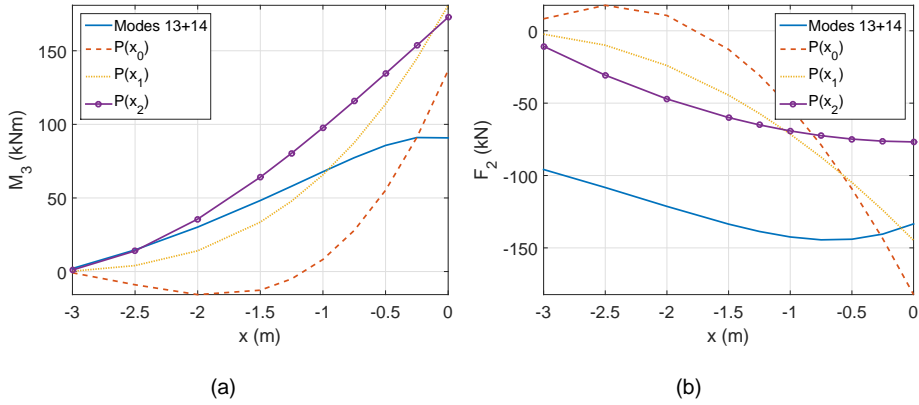


**Figure 6.15:** (a) Out-of-plane bending moment  $M_3$ , and (b) shear force  $F_2$  comparison between Submodel B and full bridge model

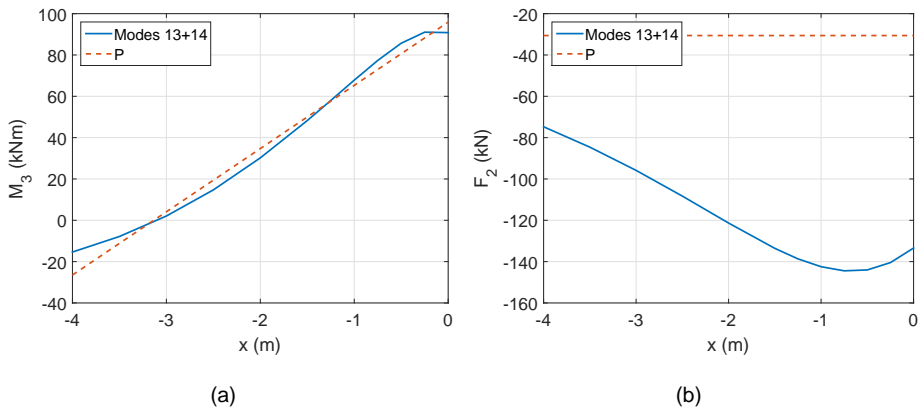


**Figure 6.16:** (a) Out-of-plane bending moment  $M_3$ , and (b) shear force  $F_2$  comparison between Submodel C and full bridge model

## **CHAPTER 7**

### **EXPERIMENTAL CAMPAIGN OF SUBASSEMBLY SPECIMENS**

#### **7.1 The experimental setup, the testing programme and the testing protocol**

##### **7.1.1 Scaling procedure**

As mentioned in Chapter 6, in order to replicate significant stress and strain levels, a specimen derived from the representative part of full bridge was obtained. The specimen was scaled of a factor  $S = 2$  in accordance with the procedure proposed by Kumar et al. (1997). Since for short/medium span composite bridge the gravity load plays an important rule, the Procedure 1 was followed. Table 7.1 shows the different scale factors to characterise specimen quantities.

Components such as the reinforcement, the steel girder profiles and the stud connectors had to match scaling requirements and at the same time follow the required commercial dimensions. A comparison in terms of the moment of inertia was adopted for scaling the I-girder section, and an IPE 330 was hence adopted. Diameters in a range of  $\phi 6$  to  $\phi 12$  were used for the reinforcing steel,

**Table 7.1:** Scale factors (Kumar et al., 1997)

Quantity	Scale factor	Value
Length	$S$	2
Mass	$S^3$	8
Stiffness	$S$	2
Force	$S^2$	4
Stress	1	1

whilst 13 mm shank diameter were chosen for the head studs.

### 7.1.2 Design of subassembly specimens

The *DIN FB 104 Var. C* detail solution was characterised by a steel girder (IPE 330) with a 420×250×35 mm head plate, as shown in Figure 7.1(a). 168 connectors were used in total. On the girders' top flanges two rows of Nelson studs were welded. The spacing in shear force direction ( $y$ -direction) was 67.5 mm, while in transverse direction a spacing of 80 mm was chosen. The connectors at the head plates were disposed following a four-by-five grid. Four studs were welded on each bottom flange extension. These extensions protruded 210 mm inside the concrete cross beam, had a width of 50 mm and a thickness of 12 mm.

The *DOMI1* detail solution was designed as depicted in Figure 7.1(b), where 112 Nelson studs were used to transfer shear forces from the slab to the steel girders. The stud layout was the same as in *DIN FB 104 Var. C* detail specimens. Differences lie in the head plates and the arrangement of connectors

inside the CCB. The girders' webs were extended 180 mm and 24 studs were evenly distributed over the protrusion's surfaces. A 230×140×35 mm plate with 8 studs was welded on the bottom flange of each girder, while a thin cover plate was used to delimit the remaining girder-cross beam interface.

With reference to *DOMI2* detail type, it was identified by the presence of the threaded  $\phi 16$  pre-stressed bars connecting the girders' bottom flanges. Thus, the Nelson studs became unnecessary and were used only for the web extensions, as shown in Figure 7.1(c). For this connection 24 studs were used, while 112 were welded on the top flanges of the steel beams.

As far as the aforementioned solutions are concerned, steelwork elements were fabricated directly in the workshop, steel end plates and Nelson studs were butt welded to the I-girders.

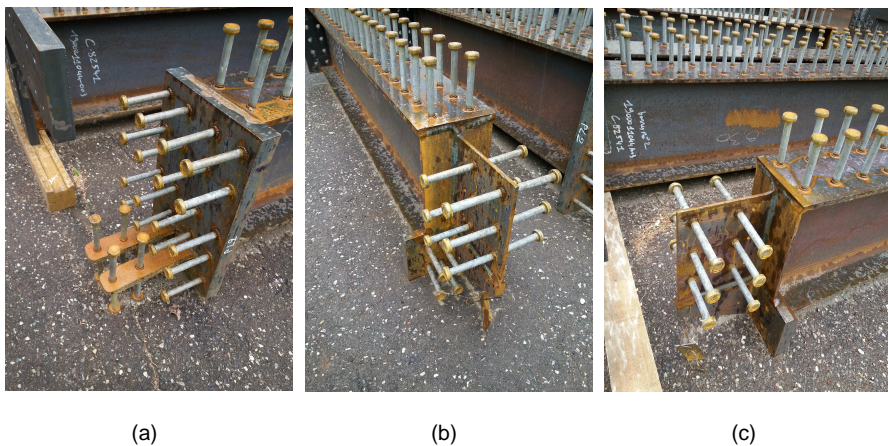


**Figure 7.1:** Steel girder-CCB connection details for (a) DIN FB 104 Var.C type, (b) DOMI1 type, and (c) DOMI2 type

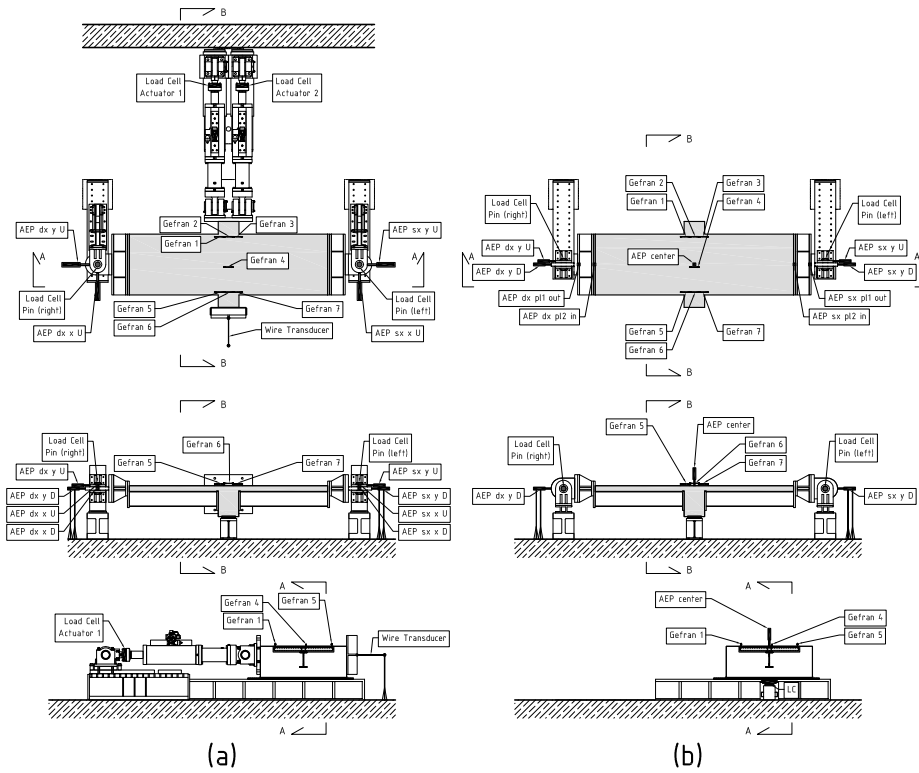


**Figure 7.2:** Testing equipment, specimen and sensor layout for (a) monotonic and cyclic tests with lateral loads, and (b) monotonic test with vertical load

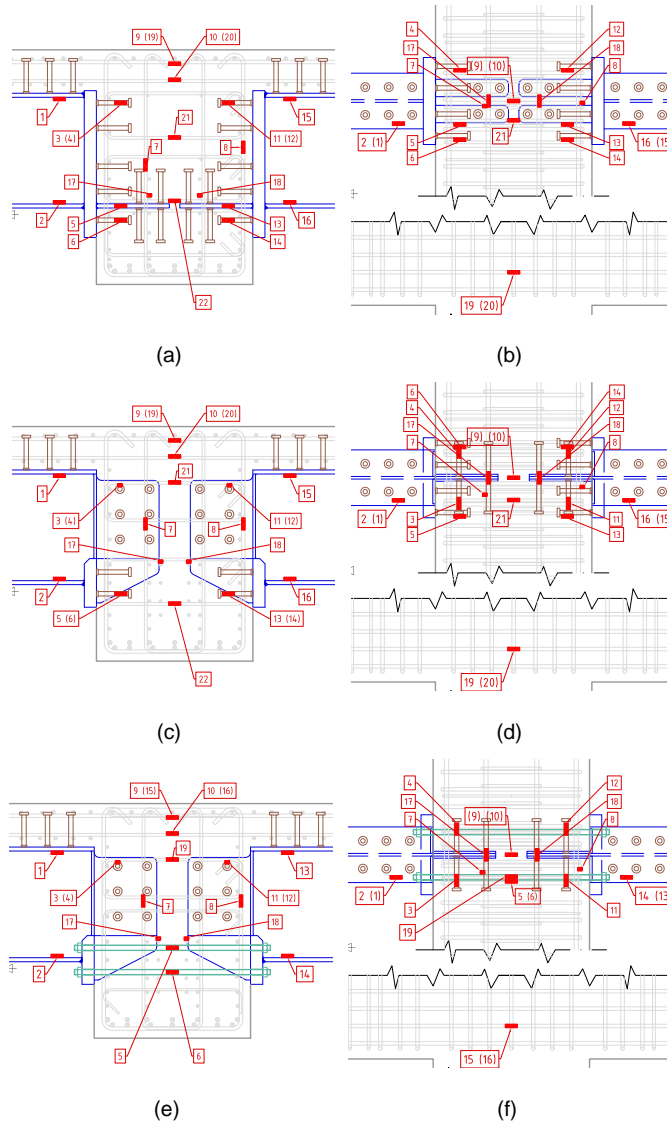


**Figure 7.3:** Strain gauges configuration for (a) front, and (b) top views for SQ1M/SQ1C tests; (c) front, and (d) top views for SQ2M/SQ2C tests; (e) front, and (f) top views for SQ3M/SQ3C/SQ3V tests, respectively

### 7.1.3 The test setup

The setup configuration conceived for the test campaign is depicted in Figure 7.2a, and was adopted for all tests with lateral -or transversal- loading. The substructured specimen was characterized by a center of gravity aligned with the two hinges at the boundaries. This layout does not reproduce substructures located at the ends of the composite slab of a bridge. For the last test, that was conceived to investigate the residual vertical loading capacity of the specimen already subjected to a certain level of damage, some modifications of the setup were needed, as schematically depicted in Figure 7.2b.

Two electro-hydraulic actuators of 1000 kN capacity each, both equipped with two load cells, indicated as *Load Cell Actuator 1 and 2* in Figure 7.2a, applied the required displacement to the CCB by means of a thick steel plate. A steel stub with two layers of Teflon on its upper surface supported the bottom face of the CCB. The edges of the concrete slab were connected to the steel pin hinges, i.e. *Load Cell Pin left and right* placed on a distance of  $L_{hinge} = 5.70$  m, by means of a steel beam. The hinges were connected to the strong floor through heavy steel beam basements. With the aim to grasp the main deformations in the critical areas of each specimen, several sensors were installed. In particular, seven *Linear Variable Displacement Transducer (LVDT) Gefran* sensors were used to measure the crack opening in the interface between the concrete slab and the CCB. With reference to both the DIN FB104 Var. C and the DOMI1 joint solutions, 22 *strain gauges (SG)* were glued on flanges of steel I-girders, rebars and Nelson studs inside the CCB; conversely, 19 *strain gauges (SG)* were placed in the DOMI2 joint solution. Strain gauges configurations for the proposed connection details are shown in Figure 7.3.

Because of the high stiffness of the specimen, the design of test setup was a challenging step which included the evaluation and the handling of the setup flexibility. Therefore, in order to monitor the setup deformation during testing, some *LVDT AEP* type were installed on the hinges. The deformability of the setup did not affect the global response of the specimens and the relevant collapse mechanism; however, the flexibility of the setup was taken into account in the calibration of the numerical models.

For the last test encompassing the vertical loading shown at the bottom of Figure 7.2b, counter columns were replaced by two stiff steel plates, which were connected to the heavy steel beams. The pin-hinges at the end of the specimen were turned by  $90^\circ$  around the y-axis. The vertical load was applied to the specimen through a hydraulic jack of 1000 kN capacity, placed at the bottom of the CCB. A *load cell (LC)* and a steel plate were inserted between the jack and the CCB.

#### **7.1.4 The testing programme**

Table 7.2 summarises the experimental campaign on the subassembly specimens. In detail, three monotonic and three cyclic tests in transversal out-of-plane directions were performed, and only a monotonic vertical test on a damaged specimen was carried out.

#### **7.1.5 The testing protocol**

Two different testing protocols were adopted for monotonic and cyclic tests. In order to reduce the inertial forces and to apply transversal or vertical loads in a quasi-static manner, a linear displacement history with an imposed velocity of

**Table 7.2:** Testing program

Test	Loading direction	Testing procedure	Test acronym	Tested detail solution
1	Transversal	Monotonic	SQ1M	DIN FB 104 Var. C
2	Transversal	Monotonic	SQ2M	DOMI1
3	Transversal	Monotonic	SQ3M	DOMI2
4	Transversal	Cyclic ECCS	SQ1C	DIN FB 104 Var. C
5	Transversal	Cyclic ECCS	SQ2C	DOMI1
6	Transversal	Cyclic ECCS	SQ3C	DOMI2
7	Vertical	Monotonic	SQ3V	DOMI2 (damaged)

0.1 mm/sec was applied for monotonic tests. With reference to the cyclic tests, the procedure according to the ECCS (1986) protocol was adopted. In detail, the monotonic tests provided the yielding point of specimens  $e_y$ , after that the displacement history were calibrated on this parameter. Moreover, the procedure adopted to obtain the yielding displacement is discussed in Section 7.2.5.

## 7.2 Monotonic tests and outcomes

The main goal of these tests was, on the one hand, to define the overall specimen response under quasi-static transversal loads, on the other hand to provide necessary information for the complete definition of the cyclic test protocol.

In order to understand the mechanism that developed inside the specimen, particular attention had to be paid to experimental results. The force-displacement relationship allowed to characterise the stiffness of the specimen tested. Moreover, it was possible to observe the displacement at which the specimen collapsed. In particular, an abrupt decrease of transversal load-bearing capacity

pinpointed the collapse of the specimen. The failure occurred after a slightly decrease in terms of force.

All three specimens showed the collapse phenomenon at the CCB displacement of 35-40 mm, as depicted in Figure 7.4. For greater displacement beyond this point, the force maintained its intensity constant around 500 kN, without other decreases of in terms of stiffness. Table 7.3 summarised the maximum values of force and displacement at failure of specimens.

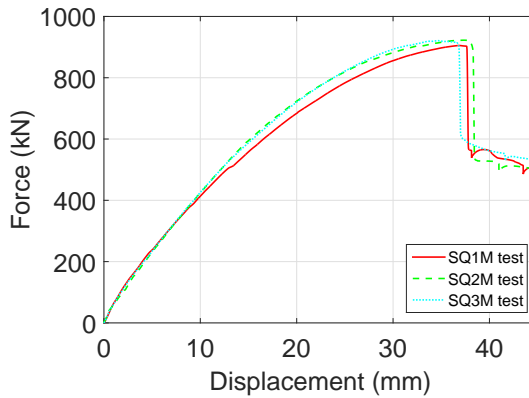


**Figure 7.4:** Force-displacement relationship of monotonic tests

**Table 7.3:** Relevant displacement and force values for monotonic tests

Testname	$d_{F_{max}}$ (mm)	$F_{max}$ (kN)	$d_f$ (mm)
SQ1M	36.9	906	37.6
SQ2M	37.4	922	38.3
SQ3M	34.8	922	36.8

At the beginning of each test, i.e. less than 1 mm in terms of displacement, slip between the steelwork elements was observed; these phenomena were due to hole-bolt clearance. For a displacement less than 2 mm, a linear elastic behaviour was observed. Values of the elastic stiffness lied between 66-69 kN/mm. The remaining part of the test showed a non-linear response. Due to the eccentricity between the force application point and the centre of gravity of specimens, rotation of the CCB in the global  $x$ - $z$ -plane occurred.

### 7.2.1 SQ1M test

The first monotonic test was performed on a specimen with the *DIN FB 104 Var. C* detail solution. Cracks became visible on the concrete slab at a displacement of 2-4 mm in the sector of Gefran 7, whilst crushing phenomenon was observed in the sector of Gefran 3. Figure 7.5(a) and Figure 7.5(b) show the deformation read by the pairs of transducers, Gefran 1+3 and 5+7, in the part of the slab under compression and tension, respectively. Both graphs pinpointed the concrete spalling through a large downfall in terms of deformation.

At top and bottom I-girders flanges, on longitudinal reinforcements of the concrete slab and on Nelson studs in the upper part of the steel head plate, significant deformations were measured, as shown in Figure 7.6(a), Figure 7.6(b) and Figure 7.7(a), respectively. In detail, strain gauges positioned on steel flanges measured deformations of nearly 2000  $\mu\epsilon$  and 1000  $\mu\epsilon$  at the top and bottom flange, respectively. On the longitudinal reinforcing steel, an approximatively linear increase of elongation was registered. With regard to the top row of studs, high deformations were reached, while low strain values on the bottom row of studs were observed, as displayed in Figure 7.7(b). The instrumented

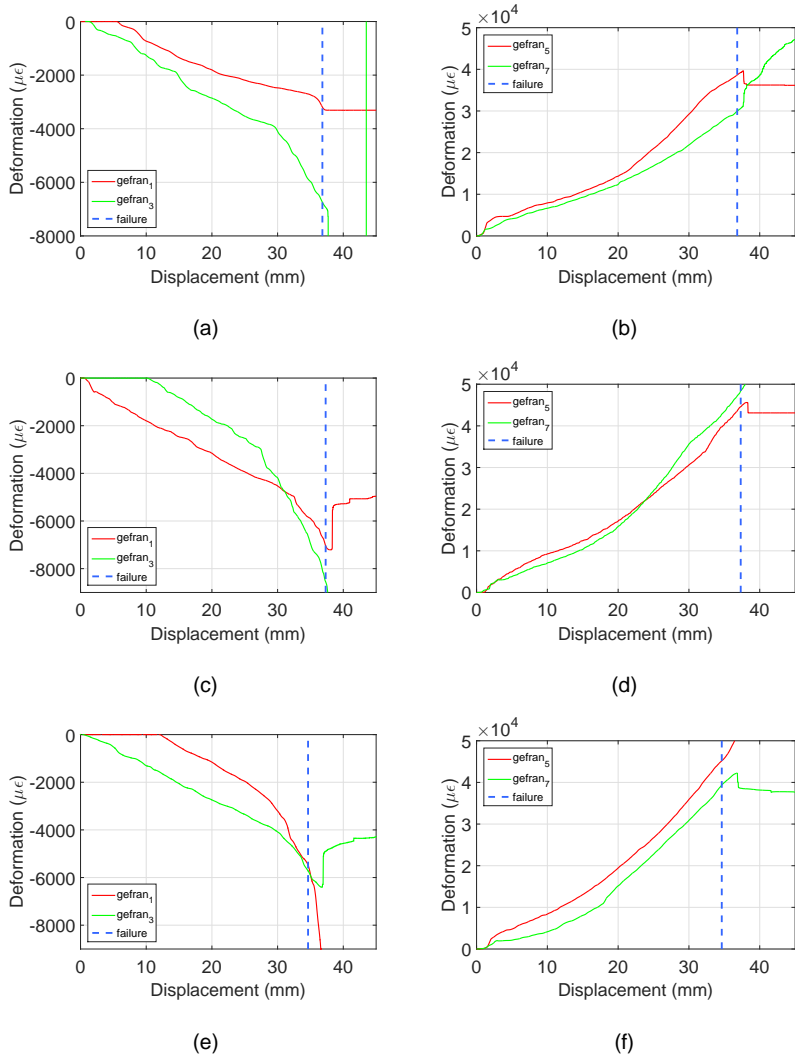
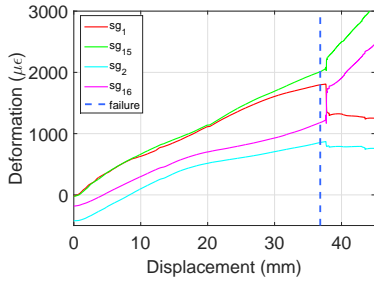
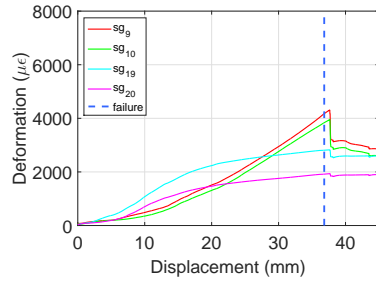


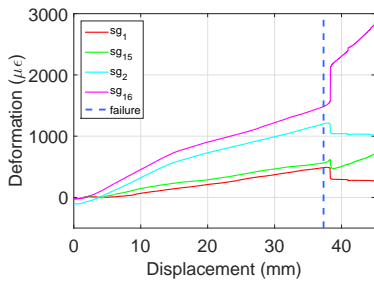
**Figure 7.5:** Deformation measured by Gefran 1, 3, 5, 7 on the top concrete slab for (a) and (b) SQ1M test, (c) and (d) for SQ2M test, and (e) and (f) for SQ3M test, respectively



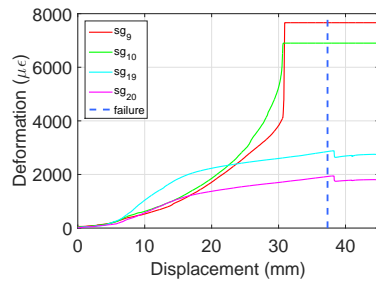
(a)



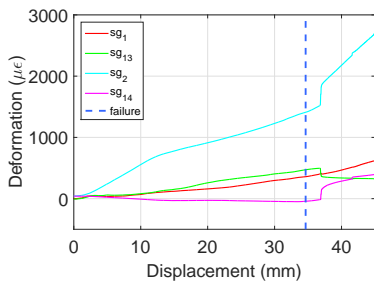
(b)



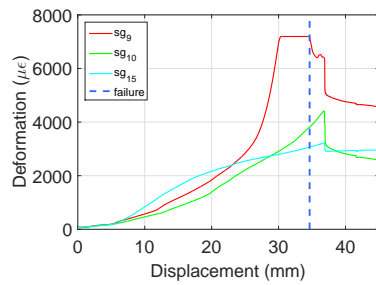
(c)



(d)



(e)



(f)

**Figure 7.6:** Deformation measured by strain gauges on top and bottom flanges of steel girders for (a) SQ1M test, (c) SQ2M test, and (e) SQ3M test, respectively; deformation measured by strain gauges on longitudinal reinforcements of the concrete slab for (b) SQ1M test, (d) SQ2M test, and (f) SQ3M test, respectively

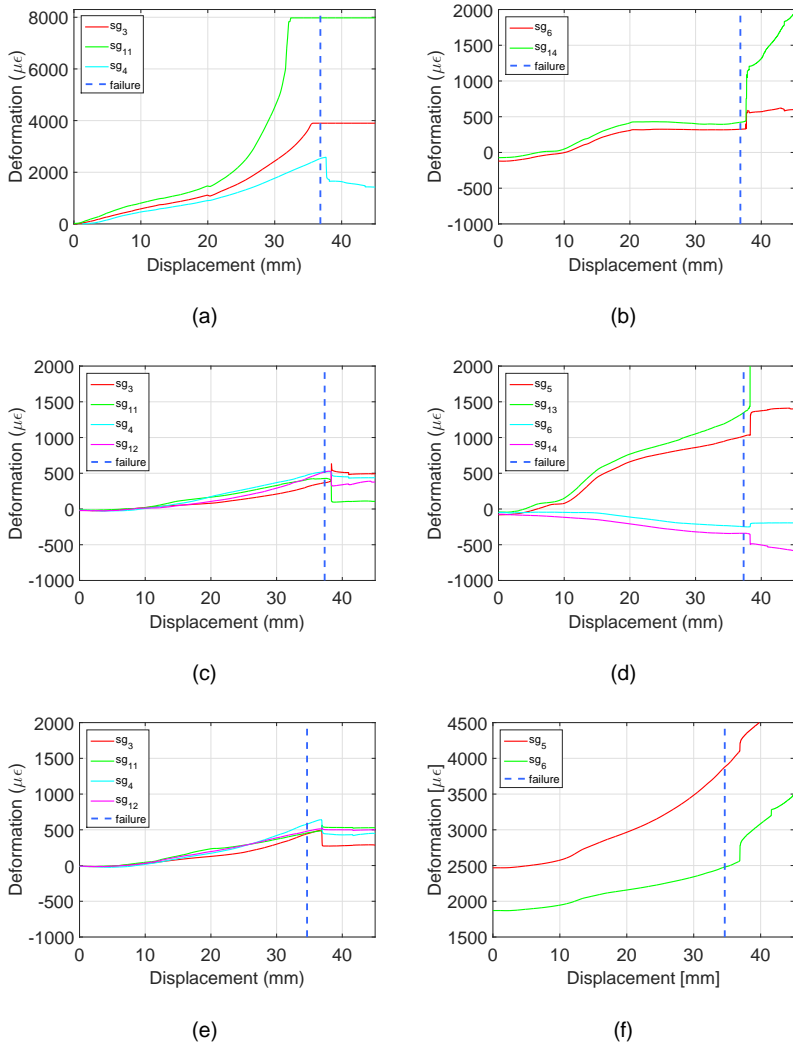
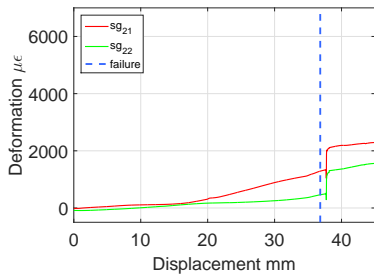
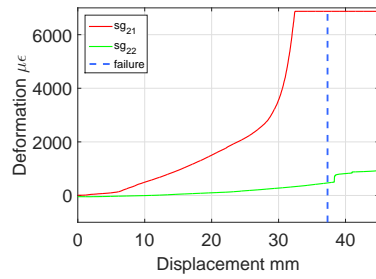


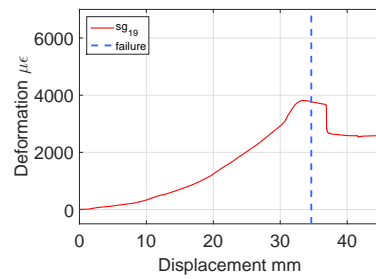
**Figure 7.7:** Deformation measured by strain gauges on: (a) top, and (b) bottom rows of studs for SQ1M test; (c) top, and (d) bottom rows of studs for SQ2M test; (e) top row of studs and (f) bottom prestresses bars for SQ3M test



(a)



(b)



(c)

**Figure 7.8:** Deformation measured by strain gauges on stirrups for (a) SQ1M test, (b) SQ2M test, and (c) SQ3M test

stirrup inside the CCB showed the value of around  $1500 \mu\epsilon$  as maximum deformation, as shown in Figure 7.8(a). The remaining instruments positioned on rebars in the CCB registered small values in terms of deformation.

### **7.2.2 SQ2M test**

The second monotonic test was performed on a specimen with the *DOMI1* detail solution. As emphasised from data transducers placed on the concrete deck, the failure of the specimen occurred on the left SCCS-CCB interface. The deformations read by Gefran instruments exhibited an almost linear trend till collapse, as shown in Figure 7.5(c) and Figure 7.5(d). The bottom steel flange reached a deformation of  $1500 \mu\epsilon$ , almost three times the top steel flange's value, as depicted in Figure 7.6(c). At the moment of collapse, the strain gauges glued on the longitudinal reinforcements reached deformation values around  $7000-8000 \mu\epsilon$ , as emphasised in Figure 7.6(d). The studs welded on the web's protrusion were subjected to a low deformation, as shown in Figure 7.7(c), while Figure 7.7(d) highlighted that the studs welded on thick steel head plates were stressed partly in tension, and partly in compression. The stirrup in the upper part of the CCB reached a high value of strain, whereas low tensile deformation was registered in the stirrup in the bottom part of the concrete-cross beam, as pinpointed in Figure 7.8(b).

### **7.2.3 SQ3M test**

The last monotonic test was performed on a specimen with the *DOMI2* detail solution. In this test the collapse occurred on the right SCCS-CCB interface. Cracks developed in the concrete slab at about 2 mm of the transversal displa-

cement, but they were hardly noticeable. Crushing phenomena instead can be observed after 15 mm of the CCB displacement. As for the other monotonic test, comparable deformations were registered by Gefran instrumentations placed on the concrete slab. In particular, Figure 7.5(e) and Figure 7.5(f) show compression and tension deformations, respectively. Strain gauges on steel flanges registered small values in terms of deformation, with the exception of the left bottom flange, where a value of  $1500 \mu\epsilon$  was reached (see Figure 7.6(e)). The most severe deformations were measured by strain gauges placed on an internal re-bar, as shown in Figure 7.6(f). The top row of Nelson studs exhibited small deformations with a linear behaviour, as depicted in Figure 7.7(e). At the beginning of the test, a force of 63 kN was stressed into the bars; they had experienced an elongation of  $2500 \mu\epsilon$  and  $1900 \mu\epsilon$  at the strain gauges 5 and 6, respectively, as emphasised in Figure 7.7(f). Finally, Figure 7.8(c) showed a nonlinear behaviour in the stirrup placed in the upper part of the CCB.

#### **7.2.4 Outcomes of monotonic tests**

As mentioned before, the transversal displacement at which collapse of the specimen occurred varied slightly among tests. Hence, the detail type appeared not to be the main responsible for the transversal bearing capacity of specimens. The collapse mechanism developed at the SCCS-CCB interface. Although some studs exhibited heavy deformations, no detachment of the head plate from the lateral surface of the CCB was observed. Due to high stiffness of the CCB and the high geometrical ratio of reinforcement, an outstanding resistance of the detail could be observed. Cracks opened in the slab

**Table 7.4:** Monotonic tests results

At failure	Instrument	Unit	SQ1M	SQ2M	SQ3M
Force	Load cells	kN	906	922	922
Displacement ( $x$ -dir.)	Temposonic	mm	37.6	38.3	36.8
Strain (concrete spalling)	Gefran	$\mu\varepsilon$	-6800	-8500	-5800
Strain (concrete cracking)	Gefran	$\mu\varepsilon$	38800	48400	45400
Strain (steel girder flanges)	Strain gauge	$\mu\varepsilon$	2000	1500	1400
Strain (studs on head plates)	Strain gauge	$\mu\varepsilon$	>8000	1300	-
Strain (studs on web ext.)	Strain gauge	$\mu\varepsilon$	-	500	600
Strain (concrete slab re-bars)	Strain gauge	$\mu\varepsilon$	4200	>7600	>7200

near the CCB. With reference to the specimen construction, some geometrical imperfections occurred/emerged and that explained the asymmetric behaviour pinpointed during tests. The most important results obtained from monotonic test are gathered in Table 7.4.

### 7.2.5 Evaluation of the yielding point for cyclic tests

In order to define the parameter  $e_y$ , a yield limit state characterised by the displacement  $e_y^+$  as well as by the corresponding reaction force have to be defined. With the purpose of fitting the monotonic force-displacement response of the specimen with a linear polynomial approximation, indications provided in Bursi et al. (2002) were followed. In detail, on the basis of the best-fitting and on the equivalence of the dissipated energy between the actual nonlinear response and the idealiser linear approximation up to  $(e_{max}^+, P_{max}^+)$ , a trilinear polynomial curve of each response was determined, as shown in Figure 7.9. In accordance with ECCS (1986), the amplitude of cycles was calibrated on the

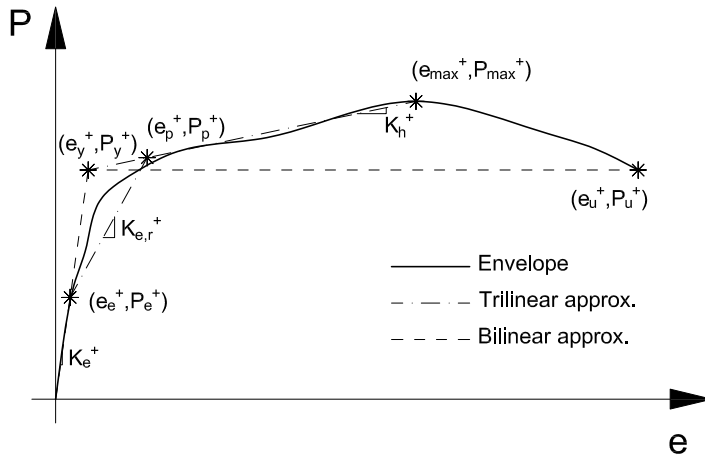


**Figure 7.9:** Bi- and trilinear fits of a force-displacement relationship envelope

basis of the yielding displacement  $e_y^+$ . Table 7.5 gathered results on the three monotonic tests, where yielding points were defined. A value of  $e_y^+ = 8$  mm was chosen as representative value for all specimens, due to the fact that it allowed to perform more cycles, while at the same time to better monitor the process of damaging. Since the failure displacement was about 40 mm,  $6e_y^+ = 48$  mm appeared to be sufficient to capture the collapse of specimens subjected to cyclic loading.

### 7.3 Cyclic tests and outcomes

The cyclic tests were the most important part of the experimental campaign. In fact, they provided the structural behaviour of subassembly specimens under particular loading conditions. The main results of SQ1C and SQ2C tests are reported and commented. A modified test protocol for the last cyclic test,

**Table 7.5:** Yielding points coordinates calculated in accordance with Bursi et al. (2002)

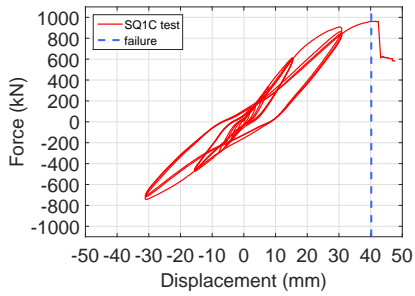
Testname	$e_y$ (mm)	$P_y$ (kN)
SQ1M	7.43	467.3
SQ2M	12.87	836.5
SQ3M	9.60	625.1

i.e. SQ3, based on a damage index approach was used.

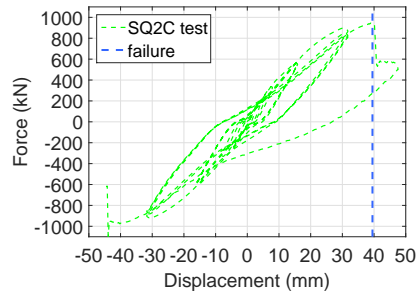
Cyclic tests allowed to investigate the specimens' response to low-cycle fatigue loading. The behaviours in terms of rotation and translation of specimens during the cyclic tests and the monotonic tests was similar. Both SQ1C and SQ2C tests reached the failure before the peak transversal displacement of the  $6e_y$  cycle, as shown in Figure 7.10. Hence, 10 load cycles with increasing amplitude was applied to the specimens. The concrete slab achieved a transversal displacement slightly higher than in SQ1M and SQ2M tests at the collapse. Moreover, no accentuate deterioration of the structures' stiffness due to the cyclic loading was observed. The observed collapse mechanism was similar to that reached during the monotonic tests. Figure 7.11 shows the region where the damaging occurred for SQ1C and SQ2C tests, respectively. Table 7.6 summarises the maximum values in terms of force and displacement registered during tests.

### 7.3.1 SQ1C test

The first cyclic test was carried out on a specimen with the *DIN FB 104 Var. C* detail solution. Collapse in form of concrete spalling was allocated to

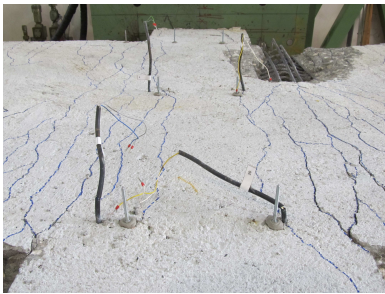


(a)



(b)

**Figure 7.10:** Force-displacement relationship for (a) SQ1C, and (b) SQ2C cyclic tests



(a)



(b)

**Figure 7.11:** Damaged specimen after (a) SQ1C, and (b) SQ2C cyclic tests

**Table 7.6:** Relevant displacement and force values for cyclic tests

Testname	$d_{F_{max}}$ (mm)	$F_{max}$ (kN)	$d_f$ (mm)
SQ1C	40.2	964	42.4
SQ2C	39.5	948	40.1

the SCCS-CCB interface. The failure occurred before the peak displacement of the 11th cycle was reached. The envelope of the SQ1C force-displacement curve fitted, with good approximation, the SQ1M test. The response during the unloading phase of every cycle exhibited an high nonlinear behaviour, even those with small amplitudes. Cracks became visible at a displacement of about 6 mm, whilst concrete crushing was observed at a displacement of 14 mm. The strain ranged between  $-5000 \mu\epsilon$  and  $80000 \mu\epsilon$  at collapse on the left SCCS-CCB interface (Gefran 3 and 7) and were almost half those values on the right side interface, as shown in Figure 7.12(a) and Figure 7.12(b). Concrete spalling was confined on the left side of the CCB. For no severe crushing occurred on the right side of the specimen, the damage pattern was asymmetric. At failure, the bottom steel flange yielded, as illustrated in Figure 7.13(a). With reference to longitudinal reinforcements in the concrete slab, Figure 7.13(b) shows how these steel elements suffered elongation with subsequent shortening during every cycle. The Nelson studs welded on head plates were subjected to tension stress, as depicted in Figure 7.14(a). Although the corresponding stud in the upper row reached a value of  $8000 \mu\epsilon$ , no detachment of the steel plate was visible with the naked eye. At collapse, also the studs in the bottom part of the head plate exceeded yielding value, as shown in Figure 7.14(b). The stirrup placed inside the CCB shows a double value in terms of deformation in comparison with these registered the SQ1M test for the same displacement (see Figure 7.15(a)).

### 7.3.2 SQ2C test

The second cyclic test was performed on a specimen with the *DOM1* detail solution. The cyclic test behaviour followed the monotonic load path. The influence of accumulated damage became evident in the second cycle of both 2  $e_y$  and 4  $e_y$ . Two regions of the concrete slab suffered from huge damage, as clearly shown in Figure 7.11(b). In detail, concrete failed due to spalling before the peak displacement of the 6  $e_y$  cycle was achieved (Gefran 1), while cracks width reached values of about 1.5 mm in the Gefran 7 zone. In the second part of the first cycle with 6  $e_y$  amplitude, concrete crushing was achieved in the sector of Gefran 7. Cracks width less than 1 mm were observed in the remaining areas of the slab and the CCB interface. Measurements from Gefran devices allowed to understand the progressive damage process of the specimen, as depicted in Figure 7.12(c) and Figure 7.12(d). The response of the SCCS-CCB connection was investigated thanks to strain gauges data. In detail, SG glued on top and bottom flanges pinpointed the yielding of ste I-girder at failure of the specimen, as illustrated in Figure 7.13(c). The longitudinal reinforcement suffered of relevant deformations, as shown in Figure 7.13(d); apparently it seems that the re-bar close to the specimen's centreline ( $y$ -axis) suffered a more severe elongation than re-bars with strain gauges 19 and 20. The deformation values provided by devices for a restrained region of the bar could be deceptive. In fact, along the longitudinal re-bars at the edge of the slab deformation was not uniform and was more evident in regions of Gefran 5 and 7. The Nelson studs in the upper and bottom part of the CCB were slightly deformed, as shown in Figure 7.14(c) and Figure 7.14(d). The instrumented stirrup showed an increasing deformation during the test. In particular, high

stress value was recorded, as reported in Figure 7.15(b).

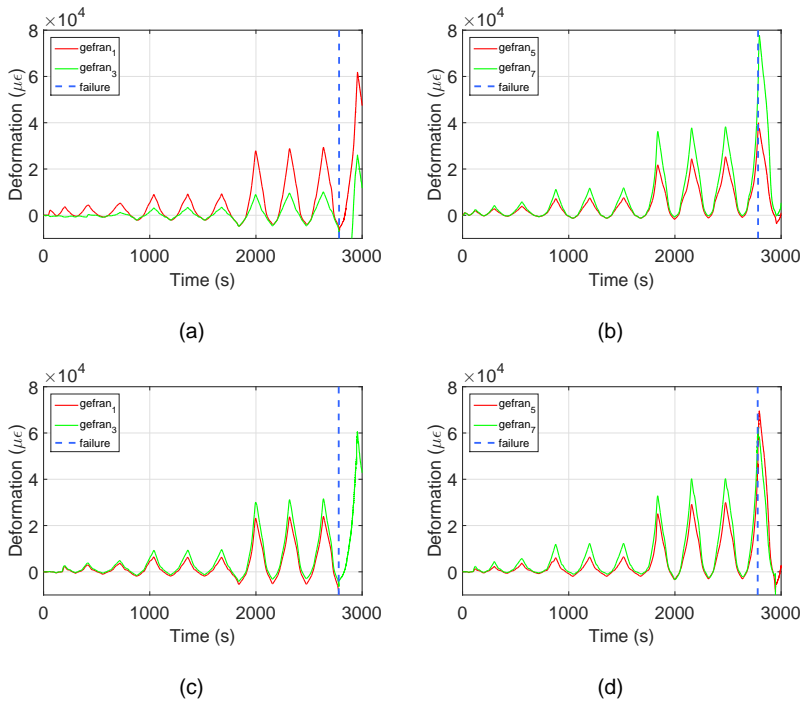
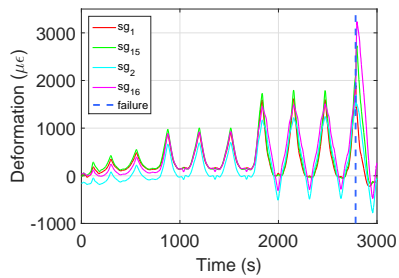


**Figure 7.12:** Deformation measured by Gefran 1, 3, 5, 7 on the top concrete slab: (a) and (b) for SQ1C test; (c) and (d) for SQ2C test, respectively

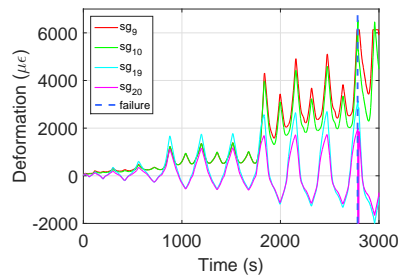
### 7.3.3 SQ3C test

#### 7.3.3.1 The damage index $D_i$ and the damage domain

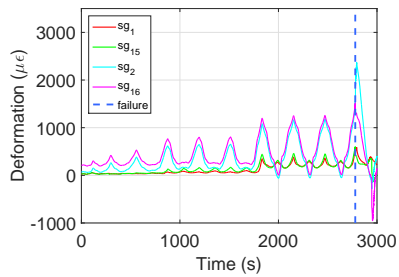
As already mentioned in Chapter 5, the damage index  $D_i$  is an empirical parameter that allowed to characterise the health's condition of structures and



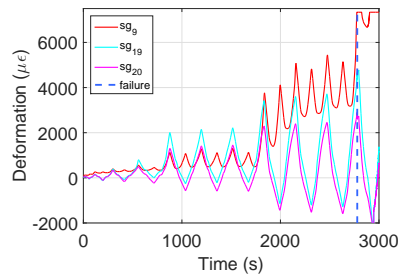
(a)



(b)



(c)



(d)

**Figure 7.13:** Deformation measured by strain gauges on top and bottom flanges of steel girders for (a) SQ1M test, and (c) SQ2M test, respectively; deformation measured by strain gauges on longitudinal reinforcements of the concrete slab for (b) SQ1M test, and (d) SQ2M test, respectively

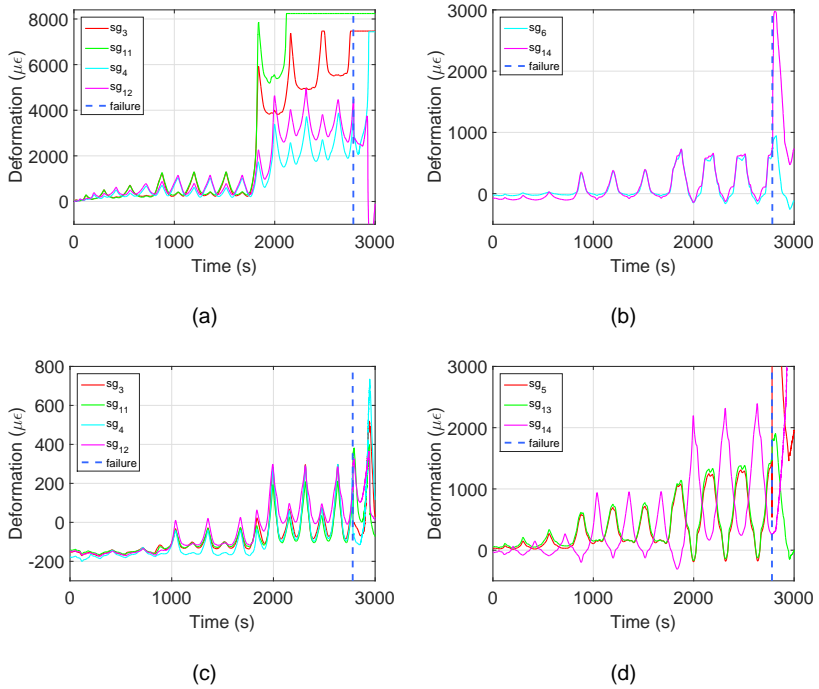


**Figure 7.14:** Deformation measured by strain gauges on: (a) top, and (b) bottom rows of studs for SQ1C test; (c) top, and (d) bottom rows of studs for SQ2C test

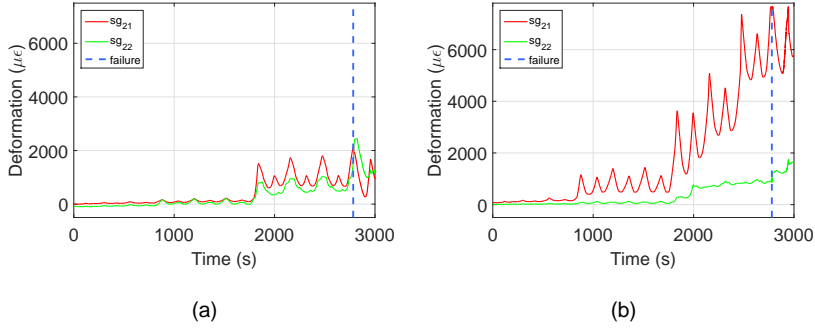


**Figure 7.15:** Deformation measured by strain gauges on stirrups for (a) SQ1C, and (b) SQ2C tests

infrastructures. It varies between 0, i.e. no damage, and 1, complete damaging of the construction. Many Authors have proposed empirical or semi-empirical relationship between common engineering parameters, such as intersory drift, curvature, strain, ect., and structural damage states. The damage index  $D_i$  according to Chai et al. (1995) is defined as follows:

$$D_i = \frac{d_m}{d_{um}} + \beta^* \cdot \frac{E_h - E_{hm}}{F_y \cdot d_{um}} \quad (7.1)$$

where  $d_m$  is the maximum response displacement,  $d_{um}$  is the maximum displacement under monotonic loading,  $E_h$  is the plastic strain energy dissipated by the member,  $E_{hm}$  is the plastic strain energy dissipated by the structure under monotonic loading,  $F_y$  is the yield strength of the member and  $\beta^*$  is the strength deterioration parameter that characterizes the damage contribution due to plastic strain energy. The model converges to  $D_i = 1$  for monotonic loading.

The damage domain can be represented in the normalized energy versus displacement space, where the ultimate limit state is defined by a straight line

with y-intercept equal to  $\frac{1}{\beta}$  and slope given by  $-\frac{1}{\beta^*}$ . In correspondence of the limit state, the damage index assumes the value of 1. Above this value, the structure is supposed to have reached failure.

The parameters of the model,  $\beta$  and  $\beta^*$ , can be calculated from experimental data. For the determination of the ULS line,  $d_{um}$  and  $F_y$  values from monotonic tests were recalled. After that, hysteretic energy of monotonic and cyclic tests, i.e.  $E_{hm}$  and  $E_h$  respectively, were calculated. Hence, five tests (three monotonic and two cyclic) conducted were able to provide five points in the normalized energy versus displacement space. The required strength deterioration parameter  $-\frac{1}{\beta^*} = -15.55$  can be extracted from the linear interpolation slope, as shown in Figure 7.16(a).

### 7.3.3.2 Damage limit states

In order to evaluate the residual bearing load capacity of a damaged specimen, specific damage threshold values were determined. With reference to the tested substructure, deck damage limit states were adopted (Mackie et al., 2008). For comparison, also the limit state proposed in CEN (2006) was considered. Table 7.7 gathers the limit states and their descriptions. The threshold chosen for the third cyclic test was the achievement of ADS2 limit state. The average spalling strain equal to  $-7850 \mu\epsilon$  was calculated as the mean of values read by Gefran 1 and 3 in SQ1C and SQ2C tests. Consequently, values at 50%, 25% and 2% of spalling strain were obtained. The SQ3C test was stopped when the value of  $-3925 \mu\epsilon$  in terms of spalling strain was achieved in the concrete slab.

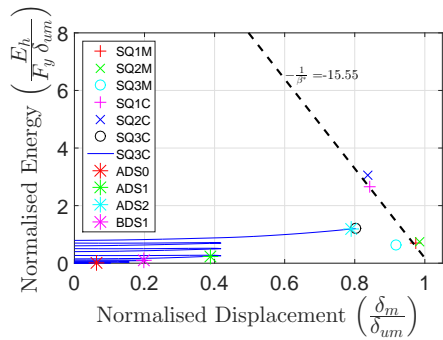
**Table 7.7:** Damage limit states in accordance with Mackie et al. (2008)<sup>1</sup> and CEN (2006)<sup>2</sup>

Limit State	Associated Strain ( $\mu\varepsilon$ )	Associated $D_i$ (-)	Damage state description
ADS0 <sup>1</sup>	-157	0.0545	No irreversible damage/yielding on structural elements, no visible effects/cracks on section
ADS1 <sup>1</sup>	-1963	0.4674	Reinforcement yielding in more than 25% of section, concrete cracking (crack width $\simeq$ 0.2 mm) and crushing
ADS2 <sup>1</sup>	-3925	0.7452	Reinforcement yielding in more than 50% of section, concrete cracking (crack width $\simeq$ 0.7 mm)
BDS1 <sup>2</sup>	-785	0.1982	Reinforcement yielding in more than 10% of section, concrete cracking (crack width $\simeq$ 0.2 mm)

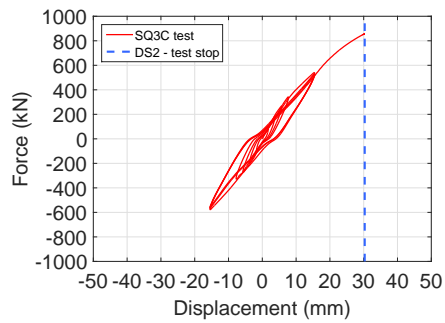
### 7.3.3.3 SQ3C test results

The last cyclic test was performed on a specimen with the *DOMI2* detail solution. The displacement history procedure was stopped before the specimen collapsed. In detail, when the 50% of the concrete spalling was read by Gefran devices, the ADS2 limit state was reached. Under this condition, the specimen achieved the displacement of 30.3 mm, and force equal to 859.3 kN was registered by the load cells of the actuators, as pinpointed in Figure 7.16(b). Figure 7.17 shows the damaged specimen at the end of the test.

The behaviour of the concrete slab was identical in compression, whilst differences were noticed in the area subjected to tension stress, as shown in Figure 7.18(a) and Figure 7.18(b). The steel girders and Nelson studs on the web extension inside the CCB were slightly stressed, as illustrated in Figure 7.18(c)



(a)



(b)

**Figure 7.16:** (a) Damage domain and limit states for tested specimens, and (b) force-displacement relationship for the SQ3C test



(a)

(b)



(c)



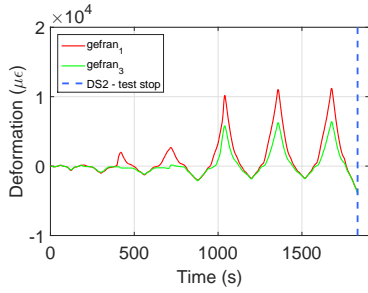
(d)

**Figure 7.17:** Damaged specimen for the SQ3C test: (a) concrete crushing at the top of the slab, (b) top view of the slab and the CCB, (c) concrete cracking read by Gefran 7, and (d) concrete cracking at the edge of the slab

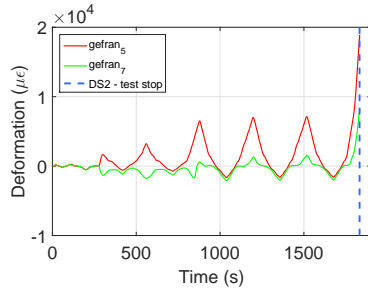
and Figure 7.18(e). With reference to longitudinal rebars, Figure 7.18(d) emphasised that the yielding phenomenon occurred at the beginning of the 4  $e_y$  cycle. The strain registered in the prestressed bars showed that the strain gauges glued on bars' surface were damaged before starting the test (see Figure 7.18(f)).

#### **7.3.4 Outcomes of cyclic tests**

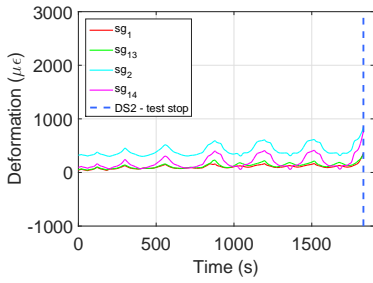
As already observed during monotonic tests, the specimen subjected to cyclic displacement history exhibited the same failure mechanism. With reference to SQ1C and SQ2C tests, the collapse were carried out for a transversal displacement of the CCB of about 40 mm. In order to perform the vertical monotonic test to the damaged specimen, the collapse was not achieved on the SQ3C test. The CCB rotated in the  $x$ - $z$  plane more than during monotonic tests. Cracks on the slab extended to the centreline of the CCB and were distributed over the entire deck surface. Over a distance of 1 m to the CCB, cracks distribution were hardly visible by the naked eye, while near the SCCS-CCB interface were easily pinpointed. No damage was observed in other part of the specimen. Hence, the collapse mechanism was independent of joint connections. The steelwork elements and concrete reinforcements were moderately stressed. In detail, yielding phenomena in longitudinal reinforcement and head plate studs were achieved. Cyclic tests confirmed both high resistance and stiffness of subassembly specimens. Moreover, tested specimens were able to dissipate plastic energy without noticeable decrease of the transversal load capacity.



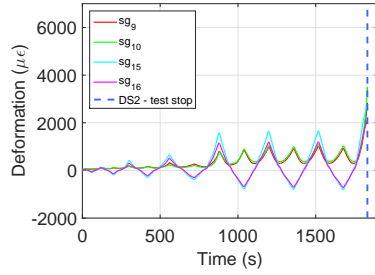
(a)



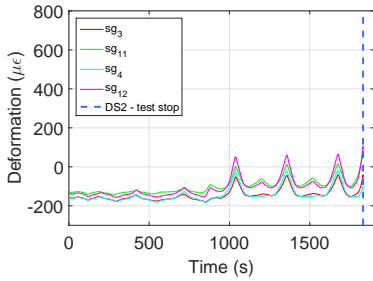
(b)



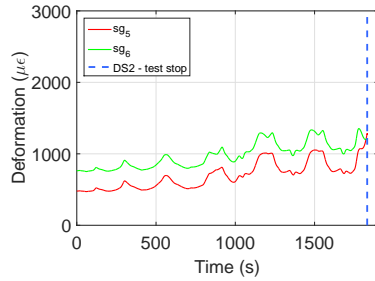
(c)



(d)



(e)



(f)

**Figure 7.18:** Deformation measured in the SQ3C test by (a) Gefran 1 and 3, (b) Gefran 5 and 7 on the top concrete slab; deformation measured by strain gauges on (c) top and bottom steel flanges, (d) longitudinal rebars in the concrete slab, (e) upper row of Nelson studs, and (f) prestressed bars

**Table 7.8:** Cyclic tests results

At failure/Max.disp*	Instrument	Unit	SQ1C	SQ2C	SQ3C*
Force	Load cells	kN	964	948	859
Displacement (x-dir.)	Temposonic	mm	42.4	40.1	30.3
Strain (concrete spalling)	Gefran	$\mu\varepsilon$	-7400	-8700	-
Strain (concrete cracking)	Gefran	$\mu\varepsilon$	55500	46500	18800
Strain (steel girder flanges)	Strain gauge	$\mu\varepsilon$	2100	1500	850
Strain (studs on head plates)	Strain gauge	$\mu\varepsilon$	>8000	1500	-
Strain (studs on web ext.)	Strain gauge	$\mu\varepsilon$	-	280	100
Strain (concrete slab re-bars)	Strain gauge	$\mu\varepsilon$	6300	>7300	>3500

#### 7.4 Vertical test and outcomes

The aim of this last test is to verify the actual stiffness and strength of the specimen after a seismic event occurred.

In order to reproduce hogging bending moments derived from a full-scale analysis of the entire bridge, a linear static F.E. model of the substructure specimen was developed in Computer and Structures (2002). Beam and shell elements were used, and also P-Delta effect were taken into account. Such numerical model provided the vertical force needed to replicate the scaled bending moment. In accordance with CEN (2002), four limit states were considered, i.e. the Ultimate limit state (ULS), and the Serviceability limit states: characteristics (SLS/ch), frequent (SLS/fr), and quasi-permanent (SLS/qp).

The SQ3V test was able to demonstrate the high stiffness and resistance of the specimen, even though it was previously damaged during the SQ3C test. A stiffness value of 10700 N/mm can be obtained for the damaged specimen tested against vertical loads. The values of vertical loads needed to reach all

limit states foreseen in CEN (2002) were considered. In detail, all serviceability limit states corresponding to quasi-permanent, frequent and characteristic loading combinations did not provide significant additional damage to the deck (see Figure 7.19(a)). Moreover, the specimen maintained a linear behaviour also for the ultimate loading combination (ULS), as shown in Figure 7.19(b). Test results are gathered in Table 7.9 .

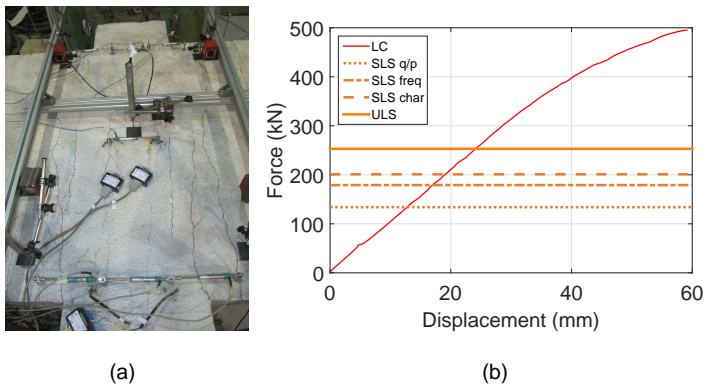


**Figure 7.19:** Force-displacement relationship of vertical monotonic test

**Table 7.9:** Vertical test results

	Instrument	Unit	SLS/qp	SLS/fr	SLS/ch	ULS
Force	Load cells	kN	134	185	201	253
Displacement (z-dir.)	AEP	mm	13.6	17.9	19.9	25.2
Strain (concrete spalling)	Gefran	$\mu\epsilon$	-	-	-	-
Strain (concrete cracking)	Gefran	$\mu\epsilon$	1200	1700	2000	2700
Strain (steel girder flanges)	Strain gauge	$\mu\epsilon$	-600	-900	-1000	-1300
Strain (studs on web ext.)	Strain gauge	$\mu\epsilon$	50	80	100	130
Strain (concrete slab re-bars)	Strain gauge	$\mu\epsilon$	700	900	1100	1400

## **CHAPTER 8**

### **NUMERICAL MODELLING AND ANALYSIS OF THE SUBASSEMBLY SPECIMEN**

#### **8.1 3D F.E. modelling of the I-girder-CCB subassembly specimen**

A fully 3D nonlinear model of the DOMI2 substructure specimen was developed with the F.E. program ABAQUS (Dassault Systèmes Simulia Corp., 2014b). The DOMI2 connection detail was chosen as the most interesting and innovative joint solution. Hence, a refined numerical model was conceived. The aim of this model was essentially to reproduce the global and local behaviour of the experimental specimen subjected to a monotonic loading. First of all, materials' low and mechanical properties of actual elements used for the test are provided. Then, a detailed description of the model is presented. After that, calibration and verification of the model are compared with the experimental results. Finally, the possibility to obtain information about the damage of the specimen are discussed.

### 8.1.1 Material models

In order to obtain realistic numerical simulations, the calibration of the material's properties is a fundamental step. The description of standard and tests needed to calibrate materials' low are provided below.

#### 8.1.1.1 Steel materials

The linear kinematic hardening model was used to simulate the inelastic behaviour of steel materials (Dassault Systèmes Simulia Corp., 2014b). This model assumes an associated plastic flow as follows:

$$\dot{\varepsilon}^{pl} = \dot{\varepsilon}^{pl} \frac{\partial F}{\partial \sigma} \quad (8.1)$$

where  $\dot{\varepsilon}^{pl}$  is the rate of plastic flow and  $\dot{\varepsilon}^{pl}$  is the equivalent plastic strain rate. The pressure-independent yield surface can be defined as:

$$F = f(\sigma - \alpha) - \sigma^0 = 0 \quad (8.2)$$

where  $\sigma^0$  is the yield stress and  $f(\sigma - \alpha)$  is the equivalent Mises stress with respect to the backstress  $\alpha$ .

#### Steel parameters

In this model a monotonic test was carried out. Hence, only stress and plastic strain values were required. Steel parameters of each steel element were obtained from material characterization tests. In detail, uniaxial tensile tests provided information about elastic modulus, yield and ultimate values in terms of strength and strain. Table 8.1, Table 8.2 and Table 8.3 summarise the mechanical characteristics of S460M I-girder steel, B450C reinforcing steel, S235J2G3+C450 Nelson stud, and M10.9 pre-stressing bar, respectively.

**Table 8.1:** Tensile test results of S460M I-girder

Mechanical property	Flange	Web	Unit
Young modulus $E$	191.7	203.7	GPa
Yield strength $f_y$	522.1	538.8	MPa
Yield strain $\varepsilon_y$	2740	2650	$\mu\varepsilon$
Ultimate strength $f_u$	662.6	649.9	MPa
Ultimate strain $\varepsilon_u$	131480	125500	$\mu\varepsilon$

**Table 8.2:** Tensile test results of B450C reinforcements

Mechanical property	$\phi_6$	$\phi_8$	$\phi_{10}$	$\phi_{12}$	Unit
Young modulus $E$	209.2	196.9	198.3	204.5	GPa
Yield strength $f_y$	515.5	527.2	537.7	538.7	MPa
Yield strain $\varepsilon_y$	2460	2690	2710	2630	$\mu\varepsilon$
Ultimate strength $f_u$	595.2	636.4	621.4	644.8	MPa
Ultimate strain $\varepsilon_u$	119370	71550	56950	70490	$\mu\varepsilon$

**Table 8.3:** Tensile test results of S235J2G3+C450 Nelson stud and M10.9 prestressing bar

Mechanical property	Nelson stud	Pre. bar	Unit
Young modulus $E$	204.8	206.8	GPa
Yield strength $f_y$	405.8	775.8	MPa
Yield strain $\varepsilon_y$	1984	3735	$\mu\varepsilon$
Ultimate strength $f_U$	487.2	1049.2	MPa
Ultimate strain $\varepsilon_U$	41100	47639	$\mu\varepsilon$

### 8.1.1.2 Concrete material

The concrete damage plasticity (CDP) model in ABAQUS Dassault Systèmes Simulia Corp. (2014b) provided the capability for modelling concrete which was subjected to monotonic and cyclic loading under low confining pressures. In order to represent the inelastic behaviour of concrete, isotropic damaged elasticity in combination with isotropic tensile and compressive plasticity was introduced. This type of material assumed two main failure mechanisms, i.e. tensile cracking and compressive crushing of concrete. Two hardening variables, i.e. tensile  $\bar{\varepsilon}_t^{Pl}$  and compressive  $\bar{\varepsilon}_c^{Pl}$  equivalent plastic strains, controlled the evolution of yield and failure surfaces. Thus, this material could represent the inelastic behaviour of concrete both in tension and compression. Moreover, uniaxial tensile and compressive behaviours are defined by damaged plasticity.

The constitutive equation of the material with scalar isotropic damage is re-

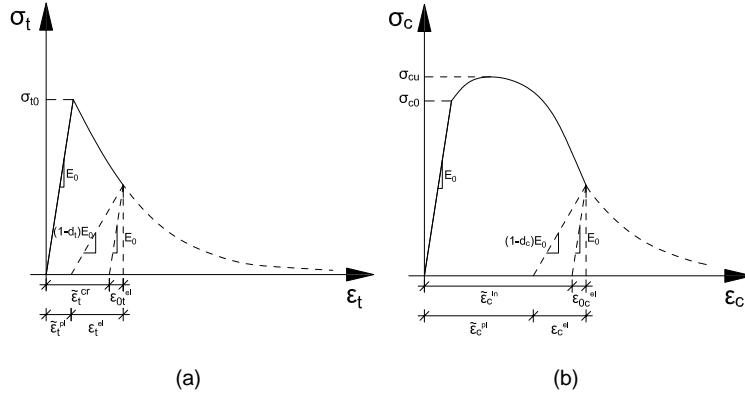


**Figure 8.1:** Response of concrete to uniaxial loading in (a) tension, and (b) compression

ported hereinafter:

$$\sigma = D^{el} : (\varepsilon - \varepsilon^{pl}) \quad (8.3)$$

where  $\sigma$  is the stress tensor,  $D^{el} = (1 - d)D_0^{el}$  is the degraded elastic stiffness tensor,  $d$  is the scalar degradation variable,  $D_0^{el}$  is the initial elastic stiffness of the material,  $\varepsilon$  and  $\varepsilon^{pl}$  are the total and the plastic tensor strain, respectively.

### Tension stiffening postfailure behaviour

The post-failure behaviour of the concrete in tension is characterised by the post-failure stress, which is defined as a function of cracking strain  $\tilde{\varepsilon}_t^{cr}$ . Figure 8.1(a) shows the definition of the cracking strain, that corresponds to the total strain minus the elastic strain, i.e.  $\tilde{\varepsilon}_t^{cr} = \varepsilon_t - \varepsilon_{0t}^{el}$ , where  $\varepsilon_{0t}^{el} = \sigma_t/E_0$ . ABAQUS calculates the plastic strain values by means of the tensile-damage

curve, as follows:

$$\varepsilon_t^{pl} = \varepsilon_t^{cr} - \frac{d_t}{(1 - d_t)} \frac{\sigma_t}{E_0} \quad (8.4)$$

where  $d_t$  is the damage variable in tension, which in turn is function of plastic strains, and  $E_0$  is the initial elastic stiffness of the concrete.

It is also possible to characterise the tension behaviour of the concrete in terms of stress-displacement values instead of stress-strain relationship. In this case the fracture energy approach is used (Hillerborg et al., 1976). This theory needs as material parameter the energy required to open a unit area of crack, i.e.  $G_F$ . The cracking displacement values are automatically converted into plastic displacement values by ABAQUS as follows:

$$u_t^{pl} = u_t^{cr} - \frac{d_t}{(1 - d_t)} \frac{\sigma_t l_0}{E_0} \quad (8.5)$$

where the specimen length  $l_0$  is assumed to be one unit length.

### Compressive behaviour

The compressive behaviour of the concrete is shown in Figure 8.1(b). The hardening data are provided in terms of inelastic strain  $\varepsilon_c^{in}$ . This strain corresponds to the total strain minus the elastic strain, i.e.  $\varepsilon_c^{in} = \varepsilon_c - \varepsilon_{0c}^{el}$ , where  $\varepsilon_{0c}^{el} = \sigma_c / E_0$ . ABAQUS calculates the plastic strain values by means of the compressive-damage curve, as follows:

$$\varepsilon_c^{pl} = \varepsilon_c^{in} - \frac{d_c}{(1 - d_c)} \frac{\sigma_c}{E_0} \quad (8.6)$$

where  $d_c$  is the damage variable in compression, which is function of inelastic strains, and  $E_0$  is the initial elastic stiffness of the concrete.

### Concrete plasticity

The CDP model uses nonassociated potential plastic flow:

$$\dot{\varepsilon}^{pl} = \dot{\lambda} \frac{\partial G(\bar{\sigma})}{\partial \bar{\sigma}} \quad (8.7)$$

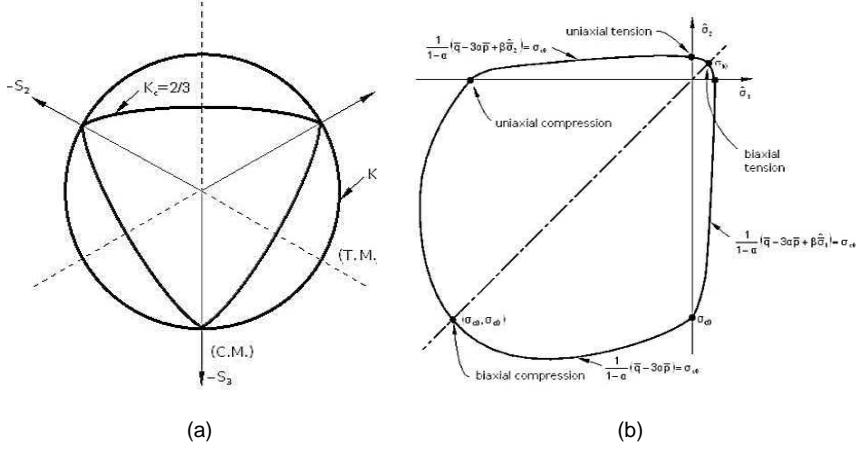


**Figure 8.2:** Yield surfaces in (a) deviatoric plane, and (b) in plane stress

The flow potential function  $G$  is defined by means of the Drucker-Prager hyperbolic function:

$$G = \sqrt{(\epsilon \sigma_{t0} \tan \psi)^2 + \bar{q}^2} - \bar{p} \tan \psi \quad (8.8)$$

where  $\psi$  is the dilation angle;  $\sigma_{t0}$  is the uniaxial tensile stress at failure;  $\epsilon$  is the eccentricity;  $\bar{p}$  is the effective hydrostatic stress; and  $\bar{q}$  is the equivalent effective stress of Mises.

The yield function is proposed by Lubliner et al. (1989), with the modification suggested by Lee and Fenves (1998) that taken into account the different evolution of strength under tension and compression, as depicted in Figure 8.2(a). The evolution of the yielding surface is provided by hardening variables,  $\bar{\epsilon}_t^{pl}$  and  $\bar{\epsilon}_c^{pl}$ . Yield function is defined as follows:

$$F = \frac{1}{1-\alpha} \left( \bar{q} - 3\alpha\bar{p} + \beta(\bar{\epsilon}^{pl}) \langle \bar{\sigma}_{max} \rangle - \gamma \langle -\bar{\sigma}_{max} \rangle \right) - \bar{\sigma}_c(\bar{\epsilon}_c^{pl}) = 0 \quad (8.9)$$

where  $\alpha$  is determined in accordance with the Kupfer's curve (Kupfer et al., 1979), as shown in Figure 8.2(b),  $\beta$  is a function of the effective tensile  $\bar{\sigma}_t$  and compressive cohesion  $\bar{\sigma}_c$  stresses, respectively,  $\bar{\sigma}_{max}$  is the algebraically maximum eigenvalue of  $\bar{\sigma}$ , and  $\gamma$  defines the shape of the loading surface in the deviatoric plane. In detail:

$$\begin{aligned}\alpha &= \frac{(\sigma_{b0}/\sigma_{c0}) - 1}{2(\sigma_{b0}/\sigma_{c0}) - 1} \\ \beta &= \frac{\bar{\sigma}_c(\bar{\varepsilon}_c^{pl})}{\bar{\sigma}_t(\bar{\varepsilon}_t^{pl})} (1 - \alpha) - (1 + \alpha) \\ \gamma &= \frac{3(1 - K_C)}{2K_C - 1}\end{aligned}\tag{8.10}$$

where  $\sigma_{b0}/\sigma_{c0}$  is the ratio of compressive strength under biaxial loading of concrete to initial uniaxial compressive yield stress (the default value is 1.16), and  $K_C$  is the ratio of the second stress invariant on the tensile meridian  $q(TM)$  to that on the compressive meridian  $q(CM)$  (the default value is 2/3).

### Concrete parameters

With reference to CEB-FIP (2010), concrete mechanical properties were evaluated. Mean compression cube strength, i.e.  $f_{cm,cube} = 60$  MPa, was identified from standard cube compression tests. The strain at the peak compression stress  $\varepsilon_{c1} = 0.0025$  and at failure stress  $\varepsilon_{c,lim} = 0.0034$  were assumed. The following basic properties of the model for the concrete were determined: Young elastic modulus  $E_c = 36715$  MPa and Poisson's ratio  $\nu = 0.2$ .

In accordance with Mander et al. (1988), the effect of confinement on concrete members due to the high reinforcement ratio was taken into account. Thus, the increasing of the peak compression strength and strain were recalculated and resulted equal to  $f_{cc} = 64.74$  MPa and  $\varepsilon_{cc} = 0.0037$ , respectively. Moreover,

the effect of reinforcement also influences the ultimate behaviour of concrete. The specific fracture energy  $G_F$ , i.e. the required energy to propagate a tensile crack of unit area (Hillerborg et al., 1976), was adopted to calibrate parameters for tensile behaviour of the concrete. The value of  $G_F = 3.6715e+04$  N/m was calculated in accordance with CEB-FIP (2010).

The damage relationship for both compression and tension behaviour of the concrete was evaluated as follows:

$$\begin{aligned} d_c &= 1 - \sigma_c/f_{cm} & \text{when } \varepsilon_c \geq \varepsilon_{c1} \\ d_t &= 1 - \sigma_{ct}/f_{ctm} & \text{when } \varepsilon_c \geq \varepsilon_{ct1} \end{aligned} \quad (8.11)$$

Finally, with reference to plasticity parameters, biaxial/uniaxial compressive strength ratio  $\sigma_{b0}/\sigma_{c0} = 1.16$ , ratio of the second stress invariant  $K_c = 2/3$ , and flow potential eccentricity  $\varepsilon = 0.1$  were assumed as suggested by ABAQUS manual Dassault Systèmes Simulia Corp. (2014a), whilst the dilation angle  $\phi = 38^\circ$  was iteratively calibrated. Moreover, in order to increase the convergence of the analysis, the viscosity parameter was set equal to 0.001.

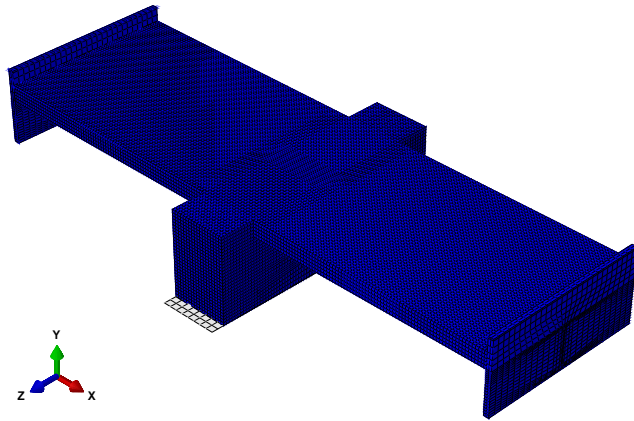
### 8.1.2 Description of the model

A detailed description of the subassembly specimen is provided hereinafter. In detail, with reference to the modelling of the concrete slab, the CCB and steel I-girders, ABAQUS (Dassault Systèmes Simulia Corp., 2014b) owned a huge family of tridimensional elements. Among these, C3D8R elements were adopted for their capability to reproduce plastic behaviour. The C3D8R element is a linear brick element with only one integration point. This element avoids the locking phenomena, but on the other hand its bending behaviour tends to be less stiff. However, the C3D8R element reduced the computational time and

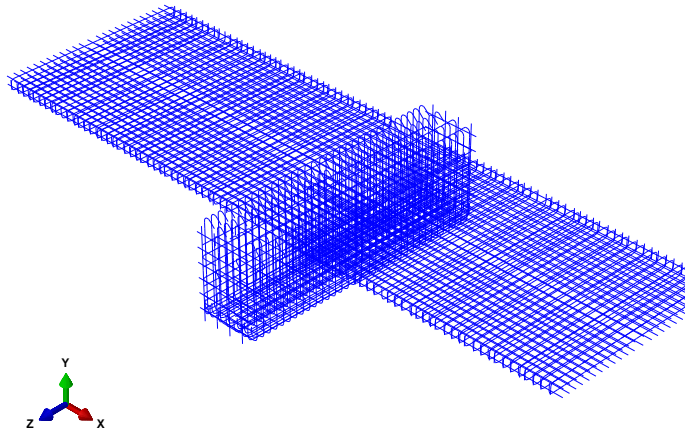
it appeared suitable for a complex nonlinear analysis.

The plane support where the specimen slides was modelled with R3D4 elements. Since Teflon sheet was placed between the bottom surface of the CCB and the plane support during experimental tests, no tangential friction was considered. Thus, only *"Hard" Contact* with *Penalty* method was used to reproduce contact behaviour.

Longitudinal and transversal reinforcements in the slab and in the CCB were modelled with monodimensional *wire* elements, whose sections were assigned as *truss* elements, as shown in Figure 8.3(b). The interaction between the concrete and the reinforcement was established by *embedded* region constraint technique. In detail, concrete elements were considered as "host" region, whilst reinforcements were assumed as "embedded" regions. Because no slip effects between the steel and the concrete were required, this approach appeared to be appropriate. In accordance with phases of experimental campaign, five steps were defined for the analysis. In the first step, also called "Initial step", all boundary conditions and interactions were imposed to the model. In particular, in order to reproduce the actual setup configuration (see Figure 7.2), restraints connected the left and the right side of the model to the ground. The influence of the deformability of steel counter cantilevers was considered by adding nonlinear springs at the ends to the model. A trilinear approximation of the force-displacement relationship derived by experimental data was obtained for each nonlinear spring, as shown in Figure 8.5. At *Translator* connector section elements were assigned these nonlinear springs, as depicted in Figure 8.4(a). *MPC Constraints* Beam type connected the steel I-girder ends plates to the restraints, as emphasised in Figure 8.4(b). Since the number of shear studs welded on the top surface of the steel I-girdered beam was calcu-



(a)



(b)

**Figure 8.3:** (a) Mesh characterisation of the specimen, and (b) reinforcing steel elements embedded to the concrete specimen

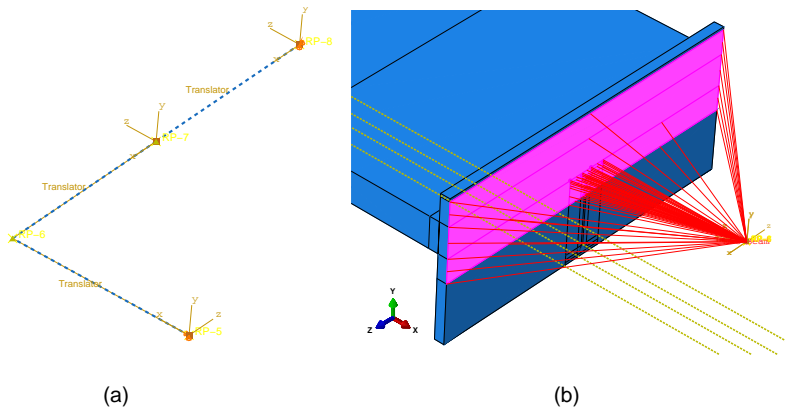


**Figure 8.4:** (a) S

lated to assure the full-interaction between I-girder and concrete slab, to connect together these elements *Tie Constraints* were adopted. On the basis of experimental evidences, small stress levels in Nelson studs welded on the web protrusions were reached. Thus, in order to reduce computational efforts, also these elements were modelled with *Tie Constraints*.

The second step consists in the application of the prestress force to prestressing bars through *Bolt load* command. In detail, with reference to the contact property, for the normal behaviour between bars and concrete "*Hard*" *Contact* with *Penalty* method was set. This method improved convergence rates, enhanced equation solver performance and allowed a good treatment of overlapping constrains (Dassault Systèmes Simulia Corp., 2014a). Moreover, the separation after contact was allowed. Lateral surfaces of prestressed bars were chosen as *Master Surface*, whilst concrete elements became *Slave Surface*. A *Surface to surface* discretization method with a small sliding formulation was adopted. Although the latter assumed that although two bodies may undergo

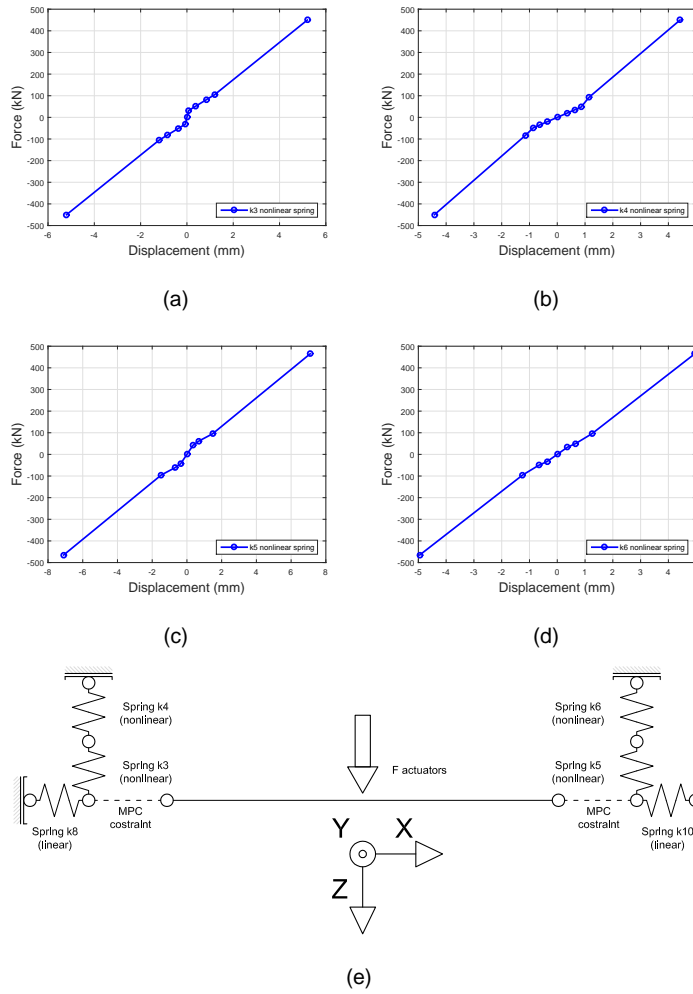


**Figure 8.5:** Trilinear force-displacement relationships of test setup (from(a) to (d)), and (e) springs setup configuration

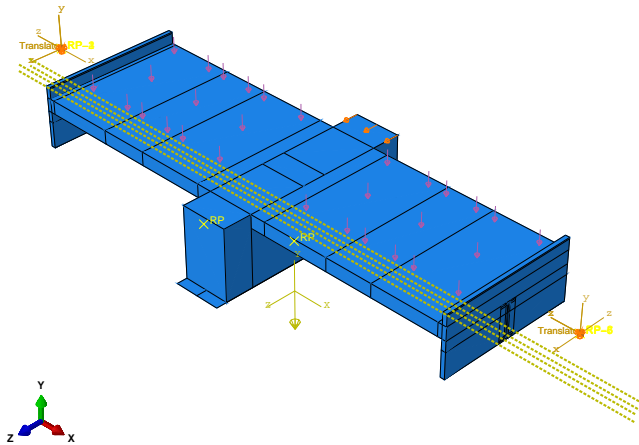


**Figure 8.6:** Model assembly of the specimen with boundary conditions, applied loads and the imposed displacement

large motions, only a small sliding was allowed.

The *Gravity* was applied to the whole model in the third step. ABAQUS automatically calculated self-weight of specimen starting from material's density and geometrical dimensions of each element.

In order to represent non-structural elements and part of the traffic load that encumbered on the specimen, additional loads were imposed on the top side of the concrete slab during the fourth step.

Finally, the fifth step corresponded to the application of the imposed displacement history to the specimen.

For solving nonlinear equilibrium equations, a *Full Newton's* method was chosen as numerical solution technique. In detail, a direct method with an asymmetric scheme for the matrix storage was adopted. These choices improved significantly the computational efficiency.

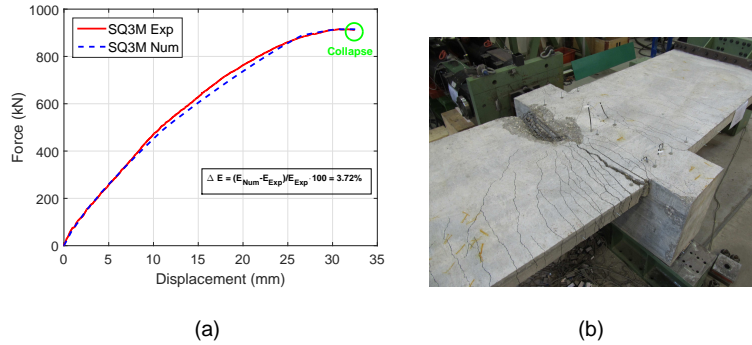


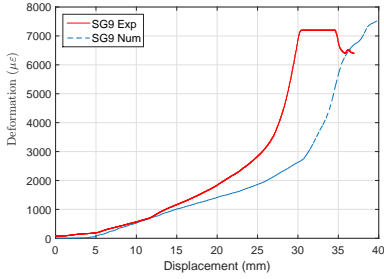
**Figure 8.7:** (a) Force-displacement comparison for the SQ3M specimen, and (b) actual damaged condition after the monotonic test

## 8.2 Validation and calibration of the numerical modelling

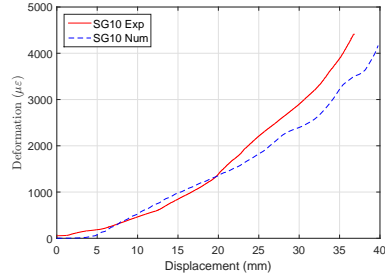
In order to determine the accuracy of a numerical model to represent the real world, the Model Validation and the Model Calibration assessment were carried out (Thacker et al., 2004). Thus, these pieces of information allow to decide whether or not the outcomes from the model matched the ones of the experimental test.

The numerical model has two main aims. On the one hand to reproduce stress, strain or displacement in certain specific points, usually where measurement devices were placed. On the other hand, after the model's ability to replicate these points had been verified, it could provide information about all the remaining part of the specimen.

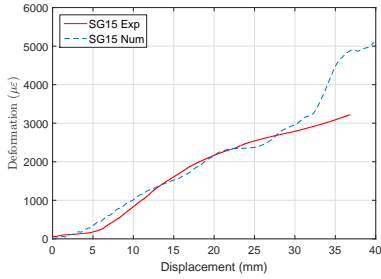
In order to verify the goodness of the FE model, numerical force-displacement curve was compared with experimental relationship. An energy error approach



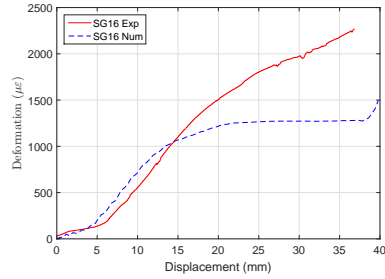
(a)



(b)



(c)



(d)

**Figure 8.8:** Comparison between experimental data read from strain gauges and numerical simulation for the (a) SG9, (b) SG10, (c) SG15, and (d) SG16, respectively

was used to quantify the effective correspondence between both global behaviours as follows:

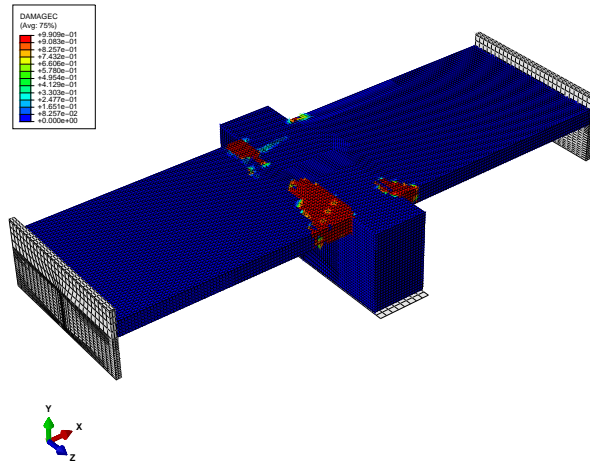
$$\Delta E = \frac{E_{model} - E_{experimental}}{E_{experimental}} = 3.72\% \quad (8.12)$$

where  $E_{model}$  is the area under the numerical curve, whilst  $E_{experimental}$  is the area under the experimental one. The slight difference between energies emphasises the goodness of the modelling. Figure 8.7(a) shows the comparison in terms of force-displacement between the model and the experimental test

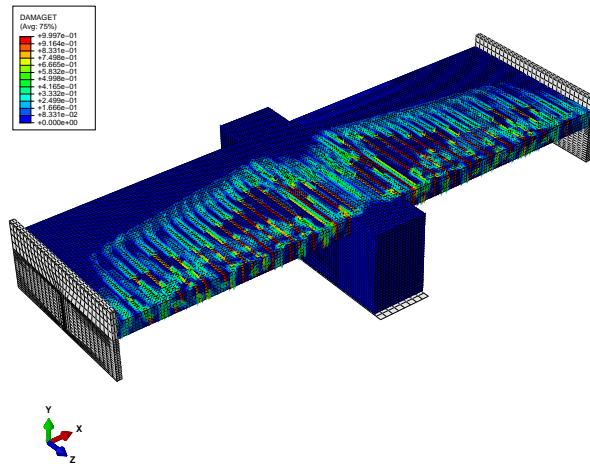
SQ3M. It can be noticed that both the initial elastic behaviour and the nonlinear force-displacement of the specimen were well reproduced by the model. Moreover, the collapse of the specimen was also well represented. In order to continue the validation of the model, also local comparison between experimental data provided by strain gauges in the specimen and strain data obtained from numerical model was carried out, as shown in Figure 8.8. The concrete cracking and crushing phenomena were captured from the model. In fact, in accordance with the experimental behaviour shows in Figure 8.7(b)), the model was able to reproduce the damage in compression and in tension of the concrete slab, as illustrated in Figure 8.9(a) and Figure 8.9(b), respectively.

After the validation, the model was subjected to a calibration process. Actually, only the stiffness of springs that represents steel counter cantilevers was adjusted to the experimental behaviour. This process was needed in order to improve the accuracy of the non-linear response of the specimen. As a result, also significant enhancements in terms of local deformations were pinpointed in reinforcing steel.

As illustrated in the Figure 8.10, the FE model permits to verify the condition on steel I-girders and on reinforcements, especially in points where strain gauges sensors were not forecasted. In particular, the maximum stress in the steel web protrusion inside the CCB was about 540 MPa, as well as for the most stressed reinforcing steel in the concrete slab. Thus, at collapse, these elements exhibited slight yielding phenomena. Steel stirrups for local phenomena, namely those inside the CCB and near the steel web protrusion, remains in elastic field. This highlights that the collapse of the specimen occurred for the failure of the concrete slab-CCB interface. Moreover, the effect of the prestressed bars not influence the response of the model.

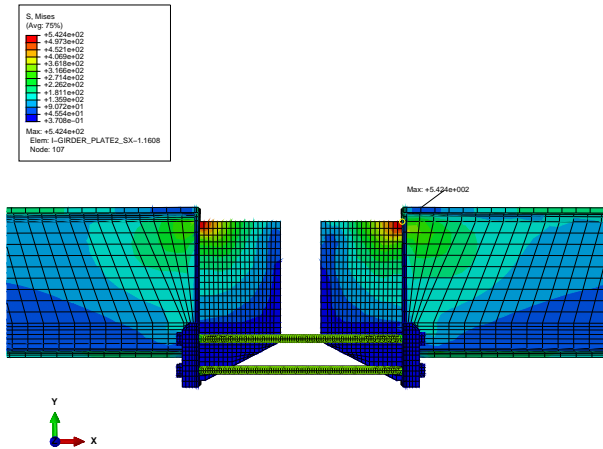


(a)

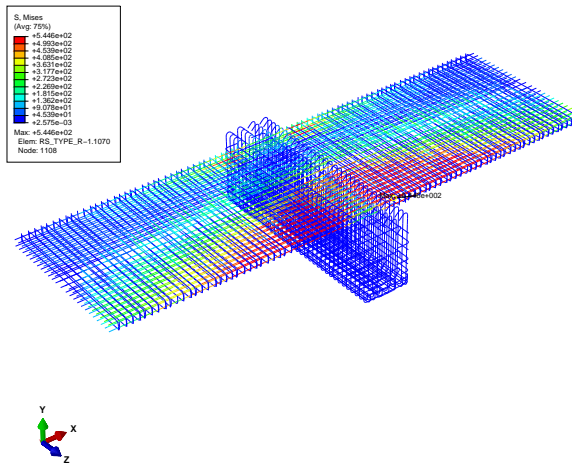


(b)

**Figure 8.9:** Damage of the concrete specimen in (a) compression, and (b) tension configurations, respectively



(a)



(b)

**Figure 8.10:** Maximum stresses on (a) steel web protrusion, and (b) on steel reinforcement cage

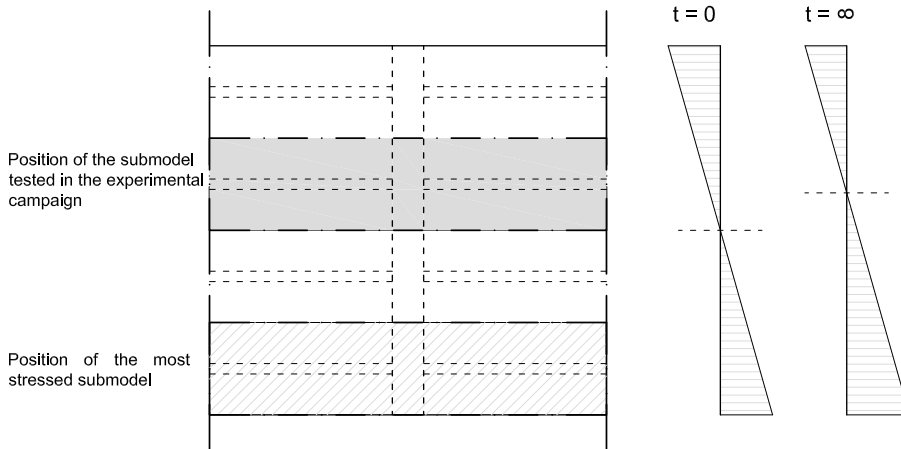


**Figure 8.11:** Location of the submodel analysed in the experimental campaign and with the FE model, and the position of the most stressed subassembly

### 8.3 Comments

Several considerations on the FE model can be pinpointed. First of all, the model is able to replicate both the most important global and local behaviours observed during the experimental test. In fact, cracking and crushing phenomena in the concrete slab are well reproduced. Moreover, stress and strain values in the longitudinal reinforcing steel at the SSC-CCB interface can be used for the definition of the yielding damage state. In fact, strain gauges glued on longitudinal reinforcements are placed inside the CCB, and they are able to measure less deformation than that indeed occurs.

The model is representative of a central part of the steel-concrete bridge, as shown in Figure 8.11. This configuration was chosen to overcome technical issues of the setup, as discussed in Chapter 6. However, the most stressed part

of the bridge subjected to a transversal loading is located at the edge of the deck. Thus, in order to take into account for the additional axial force caused by the eccentricity between the neutral axis and the position of the specimen, boundary conditions in the FE model should be modified. Moreover, the neutral axis changes position due to a progressive degradation of the resistant section. In addition, in order to represent the full-scale composite joint, geometrical dimensions of the FE model have to be scaled for a scale factor  $S = 2$  (Kumar et al., 1997).

All these modifications could quantify the damage evolution in the SCC-CCB connection detail. In fact, the FE model is the keystone to define damage measure when, as in the case of this study, few experimental tests data are available.



## **CHAPTER 9**

### **DAMAGE ASSESSMENT EVALUATION WITH A PERFORMANCE-BASED FRAMEWORK**

#### **9.1 The Performance-based Earthquake Engineering methodology**

Performance-based Earthquake Engineering (PBEE) is a probabilistic approach that allows to improve seismic risk decision-making by means of assessment and design methods that are more transparent, scientific, and informative for stakeholders than current prescriptive approaches (Deierlein et al., 2003). This methodology represents a consistent framework in which all the uncertainties in earthquake performance assessment are taken into account. The main task of the PBEE framework is to relate decision variables (repair costs, downtime, human costs, lane closures, ect.) directly to parameters that characterised the seismic of the site (Moehle and Deierlein, 2004), as summarised in Figure 9.1.

The PBEE concept was introduced for the first time in the Vision 2000 document (SEOAC, 1995). Several developments were achieved in different fields, such as for the rehabilitation of new and existing buildings (FEMA-302, 1996; FEMA-273, 1996). These documents define the so-called First-Generation

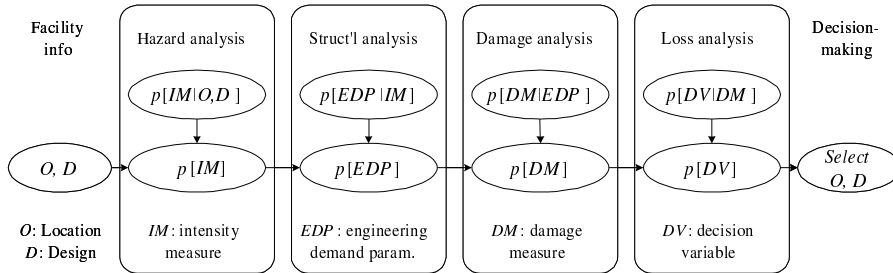


**Figure 9.1:** PBEE framework (after Moehle and Deierlein (2004); Porter (2003))

Performance-Based Seismic Engineering. This approach is essentially deterministic and it is implemented in most of codes and standards.

With the intention of treating all uncertainties and randomness in both demand and capacity, the Pacific Earthquake Engineering Center (PEER) developed a fully probabilistic framework for the performance-based design. However, in order to analyse the complete process, each problem needs to be partitioned. Thus, the PEER PBEE methodology de-aggregates the problem into several probabilistic models by means of the total probability theorem, as indicated in Equation 9.1. The mean annual frequency (MAF) of a DV exceeding a limit value  $dv$  is expressed by means of:

$$\lambda_{DV}(dv) = \int_{dm} \int_{edp} \int_{im} G(dv|dm) dG(dm|edp) dG(edp|im) d\lambda(im) \quad (9.1)$$

where  $G(DV|DM)$  is a loss or performance model, predicting the complementary cumulative distribution of a DV conditioned on a DM;  $G(DM|EDP)$  is a capacity or damage model, predicting the complementary cumulative distribution of a DM conditioned on an EDP;  $G(EDP|IM)$  is a demand model, predicting the complementary cumulative distribution of a EDP conditioned on an IM;  $G(IM)$  is a seismic hazard model, predicting the complementary cumulative distribution

of a seismic hazard  $IM$  in a single earthquake event; and  $\lambda(IM)$  is a seismic hazard model, predicting the MAF of an  $IM$  in a particular seismic hazard environment (Mackie and Stojadinovic, 2005). The methodology essentially develops into four steps:

- "*Hazard Analysis*" that characterised the seismicity of the site where the structure is placed;
- "*Structural Analysis*" provides the best estimate of the structural response by means of a non-linear model subjected to a time-history analysis;
- "*Damage Analysis*" that allows to transform response quantities derive from model to an actual measure of the state of the damage;
- "*Loss Analysis*" that relates the damage to a measure of performance.

In this section only the damage assessment will be treated. In particular, the quantification of damage for the SCCS-CCB detail will be proposed. In order to estimate damage as a function of structural response parameters, fragility functions for various damage states will be developed. Thus, the fragility function is the probability of exceeding a certain level of damage (DM) of a component as a function of a certain engineering demand parameter (EDP).

## **9.2 Assessment of components for damage fragility functions**

The data provided by the experimental campaign was used as a basis for developing the specimen fragility function. The specimen can be considered as a component due to the fact that the damage was concentrated in the SCCS-CCB detail connection. In order to use these data, the identification of significant EDPs that predict observed damage and some damage states (DSs)

that mark the progression of damage with the increasing of loading, were of fundamental importance. Moreover, the appropriate method of repair of the component under a specific damage condition was reported.

### **9.2.1 Engineering Demand Parameters**

An engineering demand parameter is a quantity that defines the earthquake demand on a specific component. The EDP allows to efficiently predict damage. The EDP is usually a geometrical or physical quantity that can be measured or calculated from experimental tests or numerical analysis. In particular, experimental tests identify the range of EDPs and emphasise the most representative EDPs for the component considered.

### **9.2.2 Damage Measures**

The damage analysis has as objective the develop of a mathematical relationship between engineering demand parameters (EDPs) and damage measures (DMs). DMs are usually reported as discrete rather than continuous quantities, defined as observations of the onset of certain damage states (Mackie et al., 2008). Specific values or ranges of DMs that quantify damage are called damage states (DSs). The DS has a strong correlation with demand and, in particular, with repair methods to restore the initial undamaged condition before any earthquake phenomena. In order to define the damage model, several sources can be taken into account. In particular, damage measures can be calculated by means of:

- experimental tests on structural components, subassembly specimens, and full-scale tests associate to the applied level demand. In this case,

the damage model is called "*Capacity Model*" or Experimental Damage Model;

- resistances of components provided by standard documents;
- finite element reliability analysis. In this case, the procedure is called "*Analytical Damage Model*".

Several examples can be found in literature. With reference to the first source, Berry and Eberhard (2007) developed empirical equations to evaluate different deformation in concrete columns. On the basis of the experimental UW-PEER reinforced concrete column performance database, concrete cover spalling, bar buckling, and bar fracture damage estimation equations were defined. With regards to the finite element reliability analysis, Mackie and Stojadinovic (2005) developed DM-EDP fragility curves for circular reinforced concrete columns. Peak strength, drift ratio, and hysteretic energy at bar buckling, drift ratio, and hysteretic energy at spalling were defined as damage limit states. Although analytical method introduces model and statistical errors, this approach allows to estimate damage without predictive equations, usually based on experimental database.

#### **9.2.2.1 Definition of damage states**

With reference to the experimental campaign, observations and data provided by installed devices on the specimen allowed to correlate specific damage to a certain measurable quantity. Owing to the geometrical configuration of the component, cracks can be concentrated around the SCCS-CCB interface, and they mainly propagate on the concrete slab rather than on the CCB. Thus,

the CCB remained in elastic field during the entire test. This situation occurred for both monotonic and cyclic tests, and for all the CCB detail connections proposed. Moreover, also the steel I-girders are in the elastic behaviour.

The discrete damage states observed during tests are reported herein:

- **Light Cracking (DS1).** This damage state is reached when the first crack of width of 0.2 mm appears on the concrete slab (CEN, 2005a), as illustrated in Figure 9.2(a). In this situation, the corresponding repair action consists in cleaning the area where damage occurred, and a subsequent application of methacrylate resin in the cracked area. This resin hardens with a curing time between 0.5 to 1 hour in 0 to 35°C conditions, and it possesses good adhesive properties because of its excellent wettability and impregnating ability in cement concrete. The aim of the repair action is to improve the barrier against water infiltration into the slab.



(a)

(b)

**Figure 9.2:** Visual damage observations corresponding to (a) DS1, and (b) DS2, respectively

- **Significant Cracking (DS2).** This damage state is reached when when the first crack with a width of 0.4 mm appears on the concrete slab (CEN,

2005a), as shown in Figure 9.2(b). The repair action for this situation consists in cleaning the area where damage occurred, and subsequent epoxy resin injections into the cracks. The epoxy resins have low viscosity and excellent workability. Moreover, it is suitable for civil engineering repair application due to its good mechanical strength. The aim of the repair action is to partially restore the undamaged condition of the component in terms of strength and stiffness.

- **Yielding of rebars (DS3).** This damage state is reached when yielding phenomenon occurs on the top and/or bottom longitudinal reinforcing steel in the concrete slab. Spalling phenomena are observed near the SCCS-CCB interface in the compression zone, as depicted in Figure 9.3(a). The repair action for this damage state consists in the removal of the spalling concrete, and new concrete material must be placed with epoxy-embedded downel bars, in order to assure the bond between the new and the existing concrete. Moreover, the area where reinforcing steel yields could be removed, and a mechanical connection between new bars and existing reinforcements have to be provided.
- **Failure of the component (DS4).** This damage state is reached when concrete crushing occurs on the top of the concrete slab, as shown in Figure 9.3(b). This phenomenon is associated with a sudden loss of strength and stiffness of the component, and thus the loss of the lateral and gravity load capacity. Buckling of longitudinal reinforcements is clearly visible after removing of the crushed concrete. Cracks width in tension zone became large (more than mm 4 mm). In this situation, the repair action consists in removing concrete using jack-hammering and reinforcing steel



**Figure 9.3:** Visual damage observations corresponding to (a) DS3, and (b) DS4, respectively

damaged, providing a mechanical connection between new bars and existing reinforcements. Moreover, damaged concrete has to be replaced where crushed and epoxy resin is injected in the cracked area. However, this damage state is rarely achieved.

Table 9.1 summarises the unit cost related to the proposed repair actions. Repair costs are assumed as mean values.

### 9.3 Damage Estimation and Evaluation of Fragility Curves

In order to take into account for the uncertainty of the evaluation of the damage, the fragility function allows to estimate the level of damage of the specimen due to some EPDs. In detail, fragility functions provide the probability of exceeding a particular damage state, DS, conditioned on a certain EDP. The lognormal distribution is appropriate in order to describe the damage. The parameters of the lognormal distribution could be estimated given a sample of the data set, namely the EDP data set. However, the median and the standard

**Table 9.1:** Component repair methods and items

Damage State	Description	Repair Item	Unit Computation	Unit Cost
DS1	Cracking in the slab (0.2 mm)	Clean deck for methacrylate (m2)	mean damage length x deck width	4 €
		Furnish methacrylate (lt)	mean damage length	20 €
		Apply methacrylate (m2)	mean damage length x deck width	205 €
DS2	Cracking in the slab (0.4 mm)	Clean deck for Epoxy (m2)	mean damage length x deck width	4 €
		Epoxy inject cracks (m)	mean damage length	620 €
DS3	Yielding of the rebar in the slab	Bridge removal, portion (m3)	mean damage deck volume	169 €
		Structural concrete, bridge (m3)	mean damage deck volume	191 €
		Bar reinforcing steel, bridge (kg)	mean damage deck volume x rebar ratio	1.49 €
		Clean deck for Epoxy (m2)	mean damage length x deck width	4 €
		Epoxy inject cracks (m)	mean damage length	620 €
DS4	Failure of the component	Bridge removal, portion (m3)	mean damage deck volume	169 €
		Structural concrete, bridge (m3)	mean damage deck volume	191 €
		Bar reinforcing steel, bridge (kg)	mean damage deck volume x rebar ratio	1.49 €
		Clean deck for Epoxy (m2)	mean damage length x deck width	4 €
		Epoxy inject cracks (m)	mean damage length	620 €

deviation of the population are estimated by means of the sample data. Thus, this assumption entails additional source of errors that become larger when a small sample data is available. In this respect, by means of the Method of the Maximum Likelihood Estimation (MLE) it is possible to provide the estimation of the probability density function (PDF) parameters. Suppose  $Y_1, \dots, Y_n$  are statistically independent random variables with a distribution governed by  $f(Y_i|\theta)$ , where  $n$  represents the sample size. The likelihood function, as indicated in Equation 9.2, is the joint probability of observing the data values  $Y_1 = y_1, \dots, Y_n = y_n$  when viewed as a function of the parameter  $\theta$ , i.e. an unknown parameter indexing a parametric family of distributions.

$$L_n(\theta) = \prod_{i=1}^n f(y_i|\theta) \quad (9.2)$$

The best model is the one that maximizes the likelihood function  $L(\theta)$ . In order to work with sum and not with product, the natural logarithm of the  $L(\theta)$  is used. The solution of the Equation 9.3 provides the required model parameters.

$$\frac{d}{d\theta} \ln L_n(\theta) = 0 \quad (9.3)$$

In order to verify that the cumulative distribution function could be assumed as longnormally distributed, the Lilliefors goodness-of-fit test was used. In this case, the Lilliefors test is more appropriate than the Kolmogorov-Smirnov Test (KS) given that the parameters of the hypothesised distribution are not known and must be estimated. The null and alternative hypotheses are therefore:

- $H_0$ : the statistical population is described by the hypothesised theoretical cumulative distribution  $P(x)$ ;
- $H_1$ : the statistical population is not described by the hypothesised theoretical cumulative distribution  $P(x)$ .

For a sample of  $n$  data, the Lilliefors test statistic is the random variable (RV):

$$D_n^* = \sup_{x \in R} |P(x) - P_{e,n}(x)| \quad (9.4)$$

where  $P_{e,n}(x)$  is the empirical cumulative frequency distribution. The null hypothesis  $H_0$  is rejected if the value of the  $D_n^*$  is sufficiently large.

### 9.3.1 Damage estimation from experimental tests and numerical simulations

Figure 9.4 shows the force-displacement relationship for tests conducted in the experimental campaign. In each plot four DS corresponding to aforementioned specific limit states are represented. The first and the second DS were obtained from data provided by linear potentiometer LVDT placed on the SCCS-CCB interface. Yield deformation on the most stressed longitudinal reinforcement in the subassembly was provided by numerical simulations obtained from the FE model. This configuration denoted the third DS. Finally, with the exception of the SQ3C test, the DS4 was reached an instant before achieving the failure of the specimen, thus when significant damage could be already observed.

### 9.3.2 Fragility functions

For this study, three representative EDPs were monitored: two global parameters, i.e. the relative traversal displacement  $d$  and the hysteretic energy  $HE$  dissipated by the specimen, and an intermediate parameter, i.e. the deck out-of-plane curvature  $\phi$ . For each damage state were reached the corresponding values. These data, in addition to the numerical simulations results, repre-

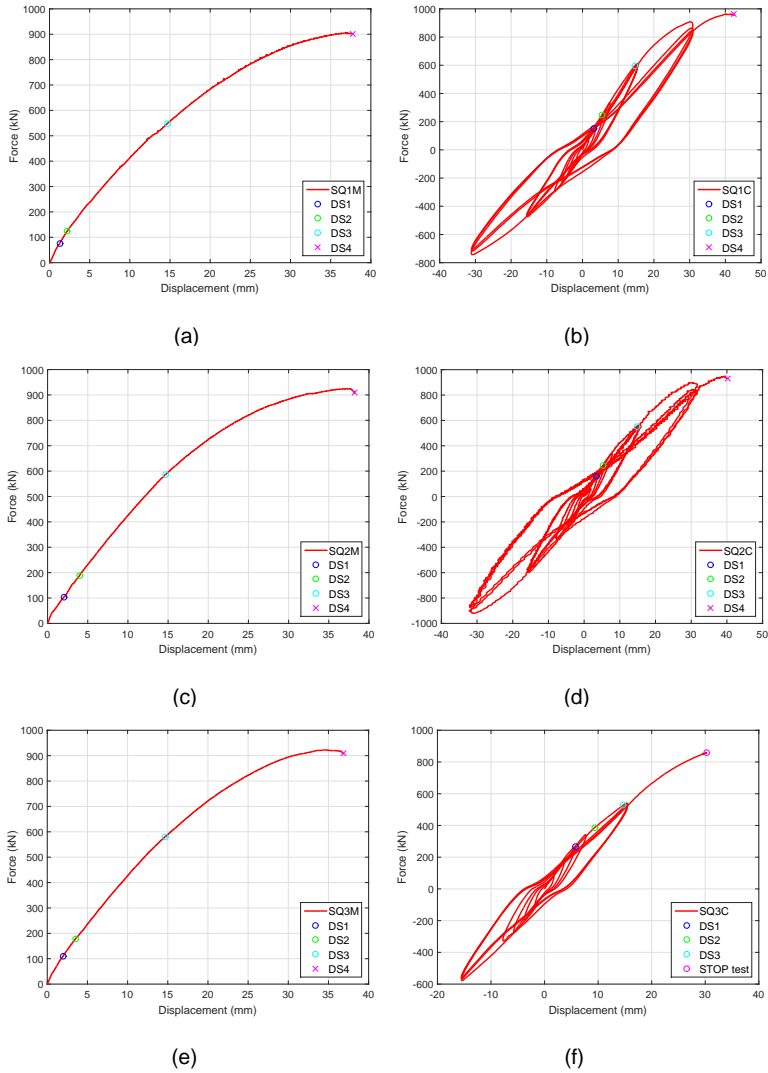


**Figure 9.4:** Identification of damage states for (a) SQ1M, (b) SQ1C, (c) SQ2M, (d) SQ2C, (e) SQ1M, and (f) SQ1C experimental tests, respectively

sent the sample data. In order to estimate median and standard deviation of the lognormal PDF, the Maximum Likelihood Estimation method was adopted. The statistical parameters estimated for representative EDPs, such as relative transversal drift (EDP1), deck curvature (EDP2) and hysteretic energy (EDP3) are summarised in Table 9.2, Table 9.3, and Table 9.4, respectively.

**Table 9.2:** Statistical parameters estimated for  $EDP1$  for the damage states

Damage State	Description	$\overline{EDP1}$ (mm)	$\sigma_{\ln EDP1}$
DS1	Cracking in the slab (0.2 mm)	2.62	0.47
DS2	Cracking in the slab (0.4 mm)	4.49	0.45
DS3	Yielding of the rebar in the slab	14.66	0.07
DS4	Failure of the component	39.03	0.05

**Table 9.3:** Statistical parameters estimated for  $EDP2$  for the damage states

Damage State	Description	$\overline{EDP2}$ (1/mm)	$\sigma_{\ln EDP2}$
DS1	Cracking in the slab (0.2 mm)	9.14e-07	0.12
DS2	Cracking in the slab (0.4 mm)	1.82e-06	0.10
DS3	Yielding of the rebar in the slab	4.87e-06	0.18
DS4	Failure of the component	1.02e-05	0.75

The lognormal cumulative distribution function was obtained on the basis of the following expression:

$$P(DS \geq ds_i | EDP = edp) = \Phi \left[ \frac{\ln(edp) - \ln(\overline{EDP})}{\sigma_{\ln EDP}} \right] \quad (9.5)$$

where  $P(DS \geq ds_i | EDP = edp)$  is the probability of exceeding damage state  $i$ ,  $\overline{EDP}$  is the median value of the  $EDP$  data set,  $\sigma_{\ln EDP}$  is the natural logarithm of the  $EDP$  data set, and  $\Phi$  is the cumulative standard normal distribution.

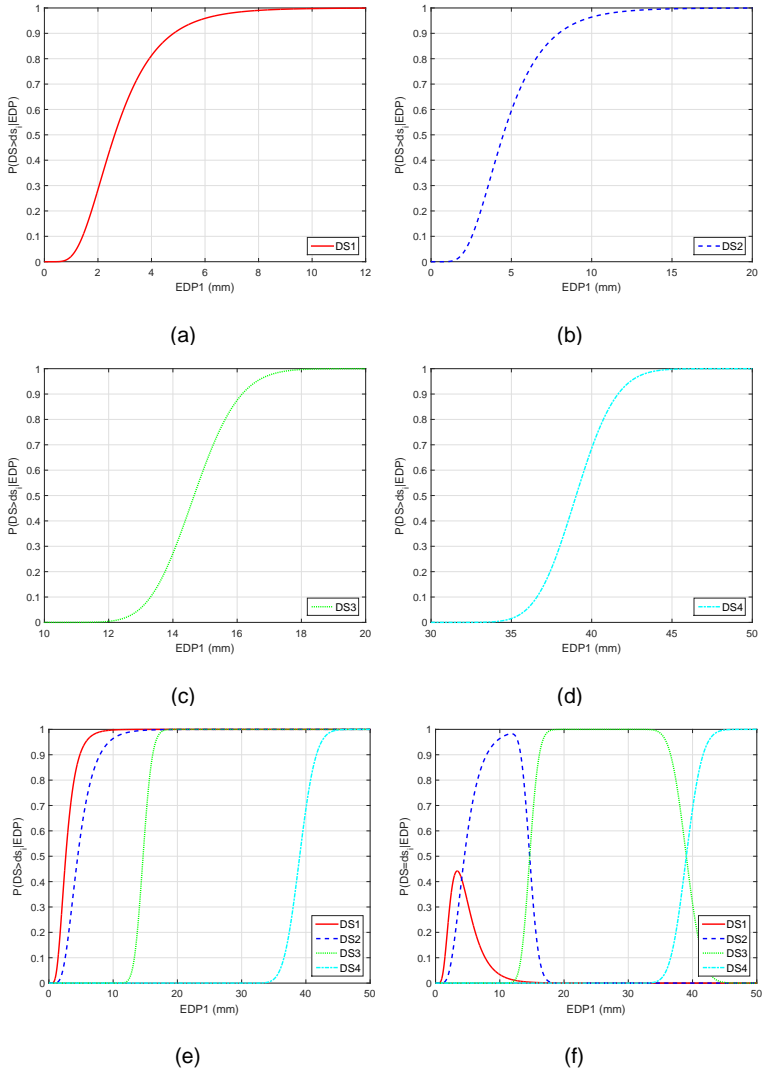


**Figure 9.5:** Fragility functions and probability of being at each damage state for the SCCS-CCB connection detail for the  $EDP1 = d$

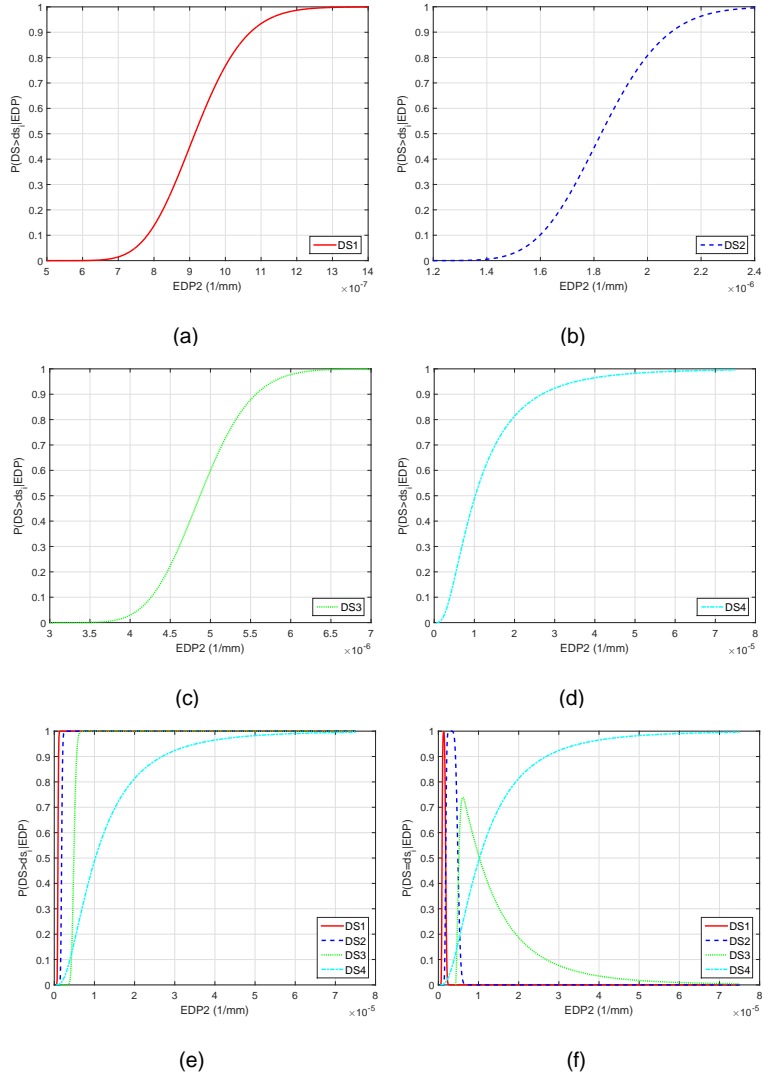
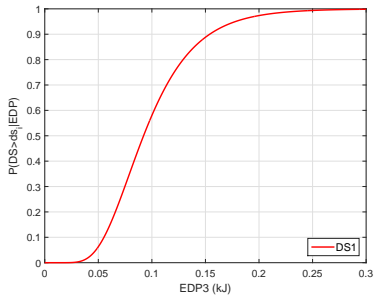
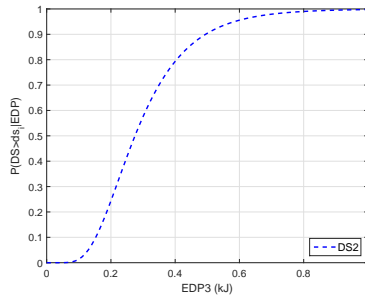


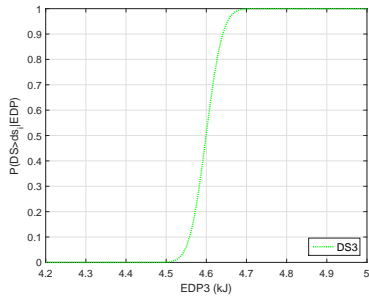
**Figure 9.6:** Fragility functions and probability of being at each damage state for the SCCS-CCB connection detail for the  $EDP2 = \phi$



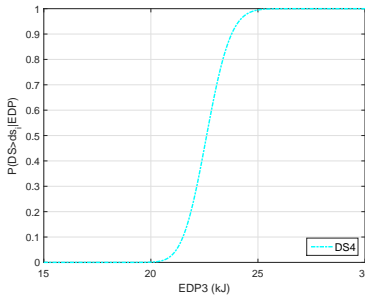
(a)



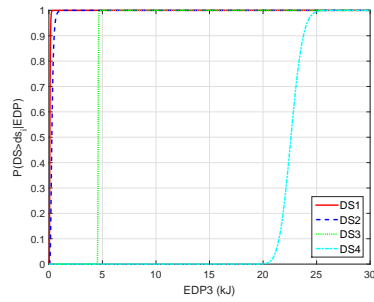
(b)



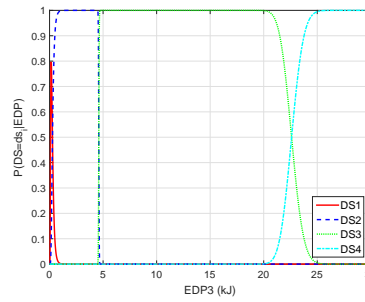
(c)



(d)



(e)



(f)

**Figure 9.7:** Fragility functions and probability of being at each damage state for the SCCS-CCB connection detail for the  $EDP3 = HE$

**Table 9.4:** Statistical parameters estimated for  $EDP_3$  for the damage states

Damage State	Description	$\overline{EDP_3}$ (kJ)	$\sigma_{\ln EDP_3}$
DS1	Cracking in the slab (0.2 mm)	0.09	0.40
DS2	Cracking in the slab (0.4 mm)	0.27	0.46
DS3	Yielding of the rebar in the slab	4.59	0.01
DS4	Failure of the component	22.60	0.04

Fragility functions developed for the SCCS-CCB connection detail can be used to estimate the probability that the joint is at a certain damage state when it is subjected to a specific level of the EDP (Aslani and Miranda, 2005). This probability can be computed as follows:

$$P(DS = ds_j | EDP = edp) = \begin{cases} 1 - P(DS \geq ds_{i+1} | EDP = edp) & i = 0 \\ P(DS \geq ds_i | EDP = edp) - P(DS \geq ds_{i+1} | EDP = edp) & 1 \leq i \leq m \\ P(DS < ds_i | EDP = edp) & i = m \end{cases} \quad (9.6)$$

where  $i = 0$  corresponds to the state of no damage in the component,  $P(DS \geq ds_j | EDP = edp)$  is the fragility function for the  $i^{th}$  damage state in the component, and  $m = 4$  is the number of damage states defines previously. In order to estimate the probability by means of Equation 9.6, fragility curves for all damage states and for each EDP were calculated. From Figure 9.5(a) to Figure 9.5(d) show the fragility curves for each damage state, Figure 9.5(e) illustrates all fragility curves together, and Figure 9.5(f) depicts the probability of being at each damage state for the relative transversal displacement  $EDP_1$ . For instance, for transversal displacement of 5 mm, the probability that the DS1 is reached is equal to 32%, whilst a probability of 60% to be in the DS2. Thus, the probability that the component does not show any damage is equal to one

minus the two calculated probabilities, i.e. 8%. The same line of reasoning can be maintained for the other EDPs, i.e.  $EDP2 = \phi$  and  $EDP3 = HE$ , as shown in Figure 9.6 and Figure 9.7, respectively.

This study is essentially related to the identification of damage states of the proposed joint. Instead, with reference to the full-scale bridge, the deformation at the deck level reached at maximum the tensile resistance of the concrete under strong earthquakes (1.9g) (Fassin et al., 2015). For this configuration, the damage level of the component was under the DS1 threshold, and thus no damage occurred. The probability of damage of this component was negligible in comparison with other components of bridge, such as piles.

## **CHAPTER 10**

### **SUMMARY, CONCLUSIONS AND FUTURE PERSPECTIVES**

#### **10.1 Summary**

Nowadays, infrastructures are of strategical importance for allowing communication between countries. Owing to its usefulness, the design and the maintenance of bridges, streets and tunnels, which represent the network, become a fundamental issue.

In order to investigate the behaviour of infrastructures under different loads, such as gravity, seismic phenomena, thermal differences, and so on, appears essential a comprehensive experimental campaign on scaled and full-scale specimens. In particular, in order to guarantee the safety of citizens, the seismic response of infrastructures under an earthquake requires a careful evaluation of the level of damage of structural elements.

In this thesis, typical case studies are considered, such as a concrete tunnel lining and a composite steel-concrete bridge.

In the first part of the thesis, a typical concrete tunnel lining is analysed. In order to investigate the inelastic behaviour of a concrete circular tunnel, several tests were performed. In greater detail, the best Fiber Bragg Grating (FBG)

package configuration was obtained by means of monotonic and cyclic tests on substructures. Based on these results, the resulting suitable configuration in a full-scale tunnel test was used to measure deformations with high accuracy. Cyclic test on the full-scale tunnel provided data on the damage of reinforcing concrete and the developing of plastic hinges. With the aim of providing information on the structural safety of a tunnel after an earthquake, a damage index was calculated. In this respect, a nonlinear fiber F.E. model in the OpenSEES environment was developed. This model calculated the stress in terms of bending moment in concrete sections with the use of experimental curvatures measured by FBGs system. Finally, the damage evolution in the concrete tunnel was reported and commented.

In the second part of this thesis, a composite steel-concrete short-medium span bridge is treated. The innovation was the application of the PEER Performance-Based Earthquake Engineering (PBEE) to this type of bridge. Moreover, the use of the Hot-rolled (HRS) steel to manufacture I-girder beams has become an innovation in civil infrastructures in Europe, as much as the use of transversal concrete cross-beams (CCBs) to connect spans. With reference to the hazard selected, a suitable case study was chosen. With the aim of understanding the most critical and stressed parts of the case study, preliminary elastic shell and stick models were developed. After the identification of interesting parts, half-scale subassembly specimens were designed and built. Several quasi-static tests, both monotonic and cyclic, were carried out with the objective of exploring global and local mechanisms in the section owing to low-cycle fatigue phenomena. To detect damage in the connection detail, a refined F.E. model in ABAQUS was developed. Fragility curve parameters of the damage's interest quantities were obtained by fitting experimental and numerical data by means

of the Maximum Likelihood Estimation method. The results and the numerical model could be ready for the application of the Performance-Based Earthquake Engineering tool, in which decision variables, such as repair costs, downtime, human life loss and lane closures, were taken into consideration in order to increase the confidence in the design for both engineer and owner's viewpoint.

## **10.2 Conclusions**

The main conclusions of this thesis are summarised herein.

With reference to the first part of the thesis, the maximum stress on the concrete section of a benchmark tunnel lining due to gravity and seismic loads is computed. In order to investigate the capability of FBG sensors for monitoring the inelastic response of a new circular tunnel lining subjected to seismic loading, an experimental campaign based on substructure and full-scale tests was carried out. Several fiber package solutions were tested, such as bonded and unbonded in concrete; internal (embedded) and external sensors. First of all, both embedded and external unbonded solutions for fiber sensors, classified as long-gauge sensors, were able to perform with reliably deformations in the inelastic range at strains higher than 1%. This value was believed to be adequate to estimate deformation demands of ductile concrete sections in moderate/high seismic areas. Such strains occurred both in substructure tests and in the full-scale test. Second, with reference to the demand moment-curvature diagram, it can be observed that nonlinearities were well detected by fiber measurements. The plastic hinge length estimated by means of Standards expressions was in a range between 165 and 480 mm. In those places, where high nonlinear behaviours owing to seismic loading were expected, i.e. over the maximum expected spacing of cracks and within the expected plastic hinge length, a cir-

cumferential unbonded fiber package with 3 sensors in a row was suited to structure monitoring. In fact, the FBGs system mounted in the full-scale test showed a maximum strain value of about 1.2% at sections of the tunnel where plastic hinges formed. Moreover, embedded fibers acquired data that were less perturbed than those provided by external fibers located at section without plastic hinges. Due to simple application during both the construction process and also for replacement during the service life of the infrastructure, an external solution for the fiber package could be preferable. The data obtained from the experimental campaign have been used to calibrate a nonlinear fiber FE model in OpenSEES. That model allows to calculate the corresponding bending moment on sections, and thus to predict damage evolution in the concrete tunnel lining. Finally, two threshold values of damage index corresponding to the normalised curvature where plastic hinges develop and where plastic hinges fail were provided and equal to 0.14 and 0.81, respectively.

With reference to the second part of the thesis, the seismic behaviour of new joints type for a steel-concrete composite bridge is analysed. An innovative solution for steel-concrete composite section (SCCS) bridges with hot-rolled sections (HRSs) has been the conception of the concrete cross-beam (CCB). In particular, a design procedure was proposed and developed step-by-step for each SCCS-CCB detail solution considered. In order to investigate the out-of-plane transversal behaviour, an experimental campaign on half-scale subassembly specimens was carried out. In particular, damage observations were reported during both monotonic and cyclic tests. All tests clearly showed that specimen failure was mainly governed by the concrete slab more than the connections between the I-girder steel beams and the CCB. Because the design was governed by static loading, the CCB suffered limited damage un-

der seismic loading. Therefore, the connection details under study did not influence the seismic response of the bridge subassembly under transversal loadings. However, Nelson studs welded on the web protrusion in the innovative solution called DOMI1 and DOMI2 suffered considerably less stress than those placed in the classical solution based on DIN FB 104 (2009). Moreover, with the aim to verify the residual gravity load capacity, a monotonic vertical test on a damaged specimen was carried out. Favourable behaviour was observed for both serviceability and ultimate limit states. A 3D refined nonlinear model developed in ABAQUS, calibrated on experimental data, provided additional information on the actual state of damage of the detail, and essentially confirms that local damages were concentrated on the SCCS-CCB interface. In order to estimate the damage evolution for the proposed DOMI2 joint solution, fragility functions were calculated from data provided by experimental tests and numerical simulations. The fragility function represents the probability of exceeding a damage limit state for a given engineering demand parameter. In particular, under the assumption that the probability distribution function was lognormal, probability distribution parameters estimation was carried out with the Maximum Likelihood Estimation method, and the lognormally hypothesis was verified by means of the Lilliefors test with a significance level of 5%. The probability that the connection detail was at a certain damage state when it was subjected to a specific level of the EDP was provided for each EDP considered. This study is essentially related to the identification of damage states of the proposed joint. The maximum deformation read in the full-scale bridge under a strong seismic loading (1.9g) at the deck level was closed to the tensile resistance of the concrete. Hence, the CCB connection detail did not even reach the first damage limit state DS1; as a result no damage occurred at the

component.

### **10.3 Future perspectives**

For the part relative to the concrete tunnel lining, a refined 3D model of the tunnel will be developed in an ABAQUS environment. In this way, it should be possible to calculate the damage of concrete sections, and thus developed fragility functions for the tunnel component.

For the part relative to the steel-concrete bridge, future perspectives should be addressed to apply the entire PBEE method at the benchmark bridge. However, first of all it appears to be more important to increase the capability of the FE model to predict damage. The cyclic behaviour of the 3D joint model will be validated and calibrated. These analysis could provide additional information about the evolution of the damage in the CCB detail. Moreover, the longitudinal behaviour of the CCB joint detail will be investigated. In this view, the effect of Nelson studs inside the CCB become important to the actual behaviour of the joint, and thus they will be explicitly modelled. The data derived from the experimental campaign conducted at the University of Roma Tre will be used to validate and to calibrate the 3D FE model also in the longitudinal direction. Fragility curves of the CCB joint will be generated in order to take into account also the damage evolution due to longitudinal seismic loading. The FE model will be used in other case studies to evaluate the damage, where different support conditions of the deck as well as different spans length could influence the response of the CCB joint, and, thus, reached significant level of damage.

## BIBLIOGRAPHY

- Aslani, H. and Miranda, E. (2005). Probabilistic earthquake loss estimation and loss disaggregation in buildings. *Report No. 157, University of Stanford, The John A. Blume Earthquake Engineering Center, Stanford CA.*
- BAEL91 (2000). Règles bael 91 modifiées 99 - règles techniques de concept et de calcul des ouvrages et constructions en béton armé suivant la méthode des étants-limites. *édition Eyrolles, Paris.*
- Bairaktaris, D., Frondistou-Yannas, S., Kalles, D., Stathaki, A., Kallidromitis, V., Kotrotsios, G., Negro, P., and Colombo, A. (1998). Intelligent monitoring of seismic damage in reinforced concrete tunnel linings. *Workshop on Reducing Earthquake Risks to Structures and Monuments in the EU, Cambridge, UK, 26-27.*
- Berry, M. P. and Eberhard, M. O. (2007). Performance modeling strategies for modern reinforced concrete bridge columns. *Report No. 2007/07, University of California, Pacific Earthquake Engineering Research Center, Berkeley CA.*
- BPEL91 (1993). Règles techniques de concept et de calcul des ouvrages et construction en béton précontraint, suivant la méthode des étants-limites. *édition Eyrolles, Paris.*

- Bursi, O. S., Aribert, J. M., and Lachal, A. (2002). Energy-based damage models in seismic analysis of steel-concrete composite members. *The Twelfth European Conference on Earthquake Engineering*, London.
- Bursi, O. S. and Ferrario, F. (2003). *Computational Models for the Low-Cycle Fatigue Behaviour of Composite Members and Joints*, chapter 5, pages 119–148. Progress in Civil and Structural Engineering Computing, Saxe-Coburg Publications, B.H.V. Topping, Stirlingshire, UK.
- Cazzador, E., Fassin, M., Bursi, O. S., Paolacci, F., and Hechler, O. (2015). Performance based earthquake engineering applied to composite bridges with short and medium spans and concrete cross beams. *Proceedings of the 8th International Symposium on Steel Bridges: Innovation & New Challenges 2015 (SBIC-2015)*, Istanbul, Turkey.
- CEB-FIP (2010). CEB-FIP Model Code 2010. *Fib-International*.
- CEN (2002). Eurocode 0: Basis of structural design. *European Committee for Standardization*, Brussels, Belgium.
- CEN (2005a). Eurocode 2: Design of concrete structures. Part 1-1: General rules and rules for buildings. *European Committee for Standardization*, Brussels, Belgium.
- CEN (2005b). Eurocode 3: Design of steel structures. Part 1-1: General rules and rules for buildings. *European Committee for Standardization*, Brussels, Belgium.
- CEN (2005c). Eurocode 3: Design of steel structures. Part 1-8: Design of joints. *European Committee for Standardization*, Brussels, Belgium.

- CEN (2006). Eurocode 8: Design of structures for earthquake resistance. Part 2: Bridges. *European Committee for Standardization*, Brussels, Belgium.
- CEN (2012a). Eurocode 4: Design of composite steel and concrete structures. Part 1-1: General rules and rules for buildings. *European Committee for Standardization*, Brussels, Belgium.
- CEN (2012b). Eurocode 4: Design of composite steel and concrete structures. Part 2: General rules and rules for bridges. *European Committee for Standardization*, Brussels, Belgium.
- Chabrolin, B., Kretz, T., and Laravoire, J. (2010). Ponts mixtes acier-béton - Un guide pour des ouvrages innovants - Projet national MIKTI. *Institut pour la recherche appliquée et l'expérimentation en génie civil (IREX)*, Presses des ponts, (in French).
- Chai, Y. H., Romstad, K. M., and Bird, S. (1995). Energy based linear damage model for high-intensity seismic loading. *Journal of Structural Engineering*, ASCE,, 121(5):857–864.
- Computer and Structures (2002). Sap2000 nonlinear user' s manual, v.8. *Berkeley, CA*.
- Dassault Systèmes Simulia Corp. (2014a). Abaqus/CAE 6.14-2: Analysys User's guide. *Dassault Systèmes Providence*.
- Dassault Systèmes Simulia Corp. (2014b). Abaqus/CAE 6.14-2: Integrated Software for finite element analysis and coputer-aided engineering for Structural Analysis and Design. *Dassault Systèmes Providence, RI, USA*.

- Deierlein, G. G., Krawinkler, H., and Cornell, C. A. (2003). A framework for performance-based earthquake engineering. *2003 Pacific Conference on Earthquake Engineering*.
- DIN FB 104 (2009). Composite steel and concrete bridges. *Deutsches Institut für Normung e.V., Fachbericht*, Germany.
- Ditlevsen, O. and Madsen, H. O. (1996). *Structural Reliability Methods*. Wiley, Chichester, UK.
- ECCS (1986). Recommended Testing Procedures for Assessing the Behaviour of Structural Steel Elements under Cyclic Loads. *Technical Committee 1, TWG 1.3, No. 45*, Brussels, Belgium.
- Fassin, M., Cazzador, E., Bursi, O. S., and Paolacci, F. (2015). A component-based model of steel-concrete connections for the probabilistic seismic response of short-medium span bridges. *Journal of Earthquake Engineering and Structural Dynamics*.
- FEMA-273 (1996). Nehr guidelines for the seismic rehabilitation of buildings. *Technical Report FEMA-273, Federal Emergency Management Agency, Whashington D.C.*
- FEMA-302 (1996). Nehr recommended provisions for seismic regualtions for new buildings and other structures. *Technical Report FEMA-302, Federal Emergency Management Agency, Whashington D.C.*
- Günay, S. and Mosalam, K. (2013). PEER performance-based earthquake engineering methodology, revisited. *Journal of Earthquake Engineering*, 17(6):829–858.

- Habel, W. R. and Krebber, K. (2011). Fiber-optic sensor applications in civil and geotechnical engineering. *Photonic Sensors*, 1(3):268–280.
- Hammersley, J. M. and Handscomb, D. C. (1975). Monte Carlo Methods. Fletcher, Norwich, England.
- Hashash, Y. M. A., Hook, J. J., Schmidt, B., and Yao, J. I.-C. (2001). Seismic design and analysis of underground structures. *Tunnelling and Underground Space Technology*, 16(4):247–293.
- Hashash, Y. M. A., Park, D., and Chiang Yao, J. I. (2005). Ovaling deformations of circular tunnels under seismic loading, an update on seismic design and analysis of underground structures. *Tunnelling and Underground Space Technology*, 20(5):435–441.
- Her, S.-C. and Huang, C.-Y. (2011). Effect of coating on the strain transfer of optical fiber sensors. *Sensors*, 11(7):6926–6941.
- Hillerborg, A., Modeer, M., and Petersson, P. E. (1976). Analysis of crack formation and crack growth in concrete by means of fracture mechanics and finite elements. *Cement and Concrete Research*, 6:773–782.
- Iman, R. L. and Conover, W. J. (1980). Small sample sensitivity analysis technique for computer models, with an application to risk assessment. *Communications in Statistics*, A9(17):1749–1874.
- Kerrouche, A., Boyle, W. J. O., Sun, T., Grattan, K. T. V., Schmidt, J. W., and Taljsten, B. (2009). Strain measurement using embedded fibre Bragg grating sensors inside an anchored carbon fiber polymer reinforcement pre-stressing rod for structural monitoring. *IEEE Sensors Journal*, 9(11):1456–1461.

- Kumar, S., Itoh, Y., Saizuka, K., and Usami, T. (1997). Pseudodynamic testing of scaled models. *Journal of Structural Engineering, ASCE*, 123(4).
- Kupfer, H., Hilsdorf, H. K., and Rush, H. (1979). Behavior of concrete under biaxial stresses. *ACI Journal*, 65(8):656–666.
- Lee, J. and Fenves, G. L. (1998). Plastic-damage model for cyclic loading of concrete structures. *Journal of Engineering Mechanics*, 124(8):892–900.
- Loupos, K., Kanellos, G., Bursi, O. S., Frondistou, S., Meissner, J., Bairaktaris, D., Griffoni, B., and Orfanoudakis, A. (2011). Application of fibre-optic technologies for real-time structural monitoring - the MONICO EC project. *Proceeding of the 9th International Conference on Damage Assessment of Structures (DAMAS 2011)*, Oxford, UK.
- Lubliner, J., Oliver, J., Oller, S., and Oñate, E. (1989). A plastic-damage model for concrete. *International Journal of Solids and Structures*, 25:299–329.
- Mackie, K. E., Wong, J.-M., and Stojadinovic, B. (2008). Integrated probabilistic performance-based evaluation of benchmark reinforced concrete bridges. *PEER 2007/09-report*.
- Mackie, K. R. and Stojadinovic, B. (2005). Fragility basis for california highway overpass bridge seismic decision making. *PEER 2005/12-report*.
- Majumder, M., Gangopadhyay, T. K., Chakraborty, A. K., Dasgupta, K., and Bhattacharya, D. K. (2008). Fibre Bragg gratings in structural health monitoring - present status and applications. *Sensors and Actuators*, 147:150–164.
- Mander, J. B., Priestley, M. J. N., and Park, R. (1988). Theoretical stress-strain

- model for confined concrete. *Journal of Structural Engineering*, 114(8):1804–1826.
- McKenna, F., Fenves, G. L., Scott, M. H., and Jeremic, B. (2000). Open System for Earthquake Engineering Simulation (OpenSees). *Pacific Earthquake Engineering Research Center, University of California, Berkeley, CA*.
- Migliacci, A. and Mola, F. (1984). Progetto agli stati limite delle strutture in C.A.: Parte ii. CEA, (in Italian).
- Ministero delle Infrastrutture (2008). Norme Tecniche per le Costruzioni. *Gazzetta Ufficiale*, Rome (in Italian).
- Moehle, J. and Deierlein, G. G. (2004). A framework methodology for performance-based earthquake engineering. *13 th World Conference on Earthquake Engineering Vancouver, B.C., Canada*, (679).
- Nilson, A. H. and Winter, G. (1986). Design of Concrete Structures. 10th edn, McGraw Hill, New York.
- OPCM 3274 (2003). Ordinanza del Presidente del Consiglio dei Ministri n. 3274 e s.m. (3431 - 3 maggio 2005). primi elementi in materia di criteri generali per la classificazione sismica del territorio nazionale e di normative tecniche per le costruzioni in zona sismica. *Gazzetta Ufficiale*, Rome (in Italian).
- Park, Y. J. and Ang, A. H.-S. (1985). Mechanistic seismic damage model for reinforced concrete. *Journal of Structural Engineering, ASCE*, 111(ST4):722–739.
- PCI (1991). PCI Design Handbook: Precast and Prestressed Concrete,. *Precast/Prestressed Concrete Institute*, Chicago.

- Penzien, J. and Wu, C. L. (1998). Stresses in linings of bored tunnels. *Earthquake Engineering and Structural Dynamics*, 27(3):283–300.
- Porter, K. A. (2003). An overview of PEER's performance-based earthquake engineering methodology. *Proc. Ninth International Conference on Applications of Statistics and Probability in Civil Engineering (ICASP9)*, pages 973–980. San Francisco, CA. Civil Engineering Risk and Reliability Association (CERRA).
- Pozzi, M., Zonta, D., Wu, H., and Inaudi, D. (2008). Development and laboratory validation of in-line multiplexed low-coherence interferometric sensors. *Optical Fiber Technology*, 14(4):281 – 293.
- Rao, Y. J. (1997). In-fibre Bragg grating sensors. *Measurement Science and Technology*, 8(4):355–375.
- Rodrigues, C., Felix, C., Lage, A., and Figueiras, J. (2010). Development of a long-term monitoring based on FBG sensors applied to concrete bridges. *Engineering Structures*, 32(8):1993–2002.
- SAC (1997). Protocol for fabrication, inspection, testing, and documentation of beam-column connection tests and other experimental specimen. *Sacramento, USA*.
- SEOAC (1995). A framework for performance based design. *Vision 2000, Structural Engineering Association of California*.
- Szechy, K. (1970). *The Art of Tunnelling*. Akademiai Kiadó, Budapest,.
- Thacker, B. H., Doebling, S. W., Hemez, F. M., Anderson, M. C., Pepin, J. E.,

- and Rodriguez, E. A. (2004). Concepts of model verification and validation. *Los Alamos National Laboratory*.
- Thonier, H. (1996). *Conception et calcul des structures de bâtiment - Tome 4*. Geodif.
- Werneck, M., Allil, R., Ribeiro, B., and De Nazaré, F. (2013). *A Guide to Fiber Bragg Grating Sensors, Current Trends in Short- and Long-period Fiber Gratings*. Dr. Christian Cuadrado-Laborde.
- Williams, M. S. and Sexsmith, R. G. (1995). Seismic damage indices for concrete structures: a state-of-the-art review. *Earthquake Spectra*, 11(2):319–349.
- Wu, Z. and Adewuyi, A. D. (2011). Identification of damage in reinforced concrete columns under progressive seismic excitation stages. *Journal of Earthquake and Tsunami*, 5(2):151–165.
- Yang, T. Y., Mohele, J., Stojadinovic, B., and Der Kiuregan, A. (2009). Seismic performance evaluation of facilities: Methodology and implementation. *Journal of Structural Engineering*, 135:1146–1154.
- Zonta, D., Pozzi, M., and Bursi, O. S. (2007). Performance evaluation of smart prefabricated concrete elements. *Smart Structures and Systems*, 3(4).